SYNTHESIS, CHARACTERIZATION AND ELECTRO-CATALYTIC APPLICATIONS OF METAL NANOPARTICLES-DECORATED CARBON NANOTUBES FOR HYDROGEN STORAGE

by

PHELADI MACK MASIPA

RESEARCH DISSERTATION

Submitted in fulfillment of the requirements for the degree of

MASTER OF SCIENCE

in

CHEMISTRY

in the

FACULTY OF SCIENCE AND AGRICULTURE

(School of Physical and Mineral Sciences)

at the

UNIVERSITY OF LIMPOPO

SUPERVISOR: Dr. T Magadzu

2013

DECLARATION

I declare that the dissertation hereby submitted to the University of Limpopo, for the degree of Master of Science in Chemistry has not previously been submitted by me for a degree at this or any other university; that is my work in design and in execution, and that all materials contained herein has been duly acknowledged.

Surname, Initials (Title) **Date**

DEDICATIONS

To my mother, the late Sefularo Dorcus Masipa for her encouragement, inspiration and support in every decision that I have made in life. May her soul rest in peace.

ACKNOWLEDGEMENTS

First and foremost, I would like to thank my creator God through his son Jesus Christ, for the great things He has done for me and making everything possible.

Many thanks to my supervisor: Dr. Takalani Magadzu for his encouraging words, guidance and great support. I would like to also express my sincere gratitude to Dr. Kenneth I. Ozoemena for his inspirational words and effective assistance.

I also wish to thank the Department of Chemistry staff and post-graduate students for the discussions and constructive critics we had. To all my friends, thank you for making Turfloop entertaining and enjoyable in many ways.

I wish to extend my appreciation to Mr. Mokae Bambo of Mintek (Nanoscience and Nanotechnology Laboratory) for carrying out the TEM and SEM experiment free of charge.

My appreciation also goes to University of Pretoria MSc students, Alfred Chidembo and Joel Lekitima for useful electrochemical demonstrations and methods that resulted in my research being easy and enjoyable to conduct.

Thank you National Research Foundation (NRF) for the financial assistance both on personal level and for the project.

I wish to also extend my appreciation to Mrs. Margaret Ward of the CSIR nanostructured materials for making it possible for me to analyse my samples by TEM, XRD and FTIR.

Finally, I wish to acknowledge my family at home, my brothers: Seima, Ntlatsa, Pokga, Pheeha, sisters: Raladitsa, Letjeka, Mosibudi, nephews and nieces (too numerous to mention by names), thank you all for your patience, unconditional love and support.

ABSTRACT

Since their discovery in 1991, CNTs have shown extraordinary properties and as result, these materials are being investigated for several different applications. Synthesis and electrochemical application of CNTs for hydrogen storage provide new possibilities for replacement of gasoline use in vehicles due to its cost and negative environmental impact.

The study investigated the metal nanoparticles modified multi-walled carbon nanotubes as possible storage material for hydrogen. Herein, carbon nanotubes were successfully synthesized by pyrolysis of iron (II) phthalocyanine under Ar/H_2 reducing atmosphere at 900 ^oC for 30 min. The micro-structural information of the as-prepared carbon nanotubes was examined by Transmission electron microscopy (TEM). It was found that the prepared CNTs were multi-walled with iron particles impurities present on the surface. Synthesized MWCNTs were found to have open tips as shown by TEM images. These materials were purified and functionalized with acid groups as confirmed by Fourier transform infra-red spectroscopy (FTIR). A successful decoration of MWCNTs by Cu, CuO, Fe, Fe_2O_3, Ni and NiO nanoparticles was confirmed by Scanning electron miscroscopy (SEM) and Transmission electron microscopy (TEM). TEM images showed that metal nanoparticles and metal oxides were well dispersed on the surface of the MWCNTs. The chemical composition of the as-prepared MWCNTs was confirmed by XRD (showing the presence of metal impurities and amorphous carbon).

Synthesized materials were applied in electrochemical techniques such as cyclic voltammetry, chronopotentiometry and controlled potential electrolysis. These techniques have shown that modification of glassy carbon bare electrode (GCE) with carbon nanotubes decorated with metal nanoparticles (Cu, Ni and Fe), improves the current density, charge-discharge voltages and discharge capacity for hydrogen storage (in a 6 M KOH aqueous electrolyte). It was shown that MWCNTs exhibit high conductivity, porosity and high surface area for hydrogen

storage. The increase in discharge capacity was as follows: GCE < GCE-MWCNT < GCE-MWCNT-M (M = Cu, Ni, Fe and/or metal oxides). This confirmed a successful modification of GCE with MWCNTs and MWCNT-M (M = Cu, Ni, Fe and/or metal oxides). The maximum discharge capacity of 8 nAh/g was obtained by GCE-MWCNTs-Ni electrode, corresponding to an H/C value of 28.32 x 10^{-9} wt%. Minimum discharge capacity of 0.5 nAh/g was obtained by the GCE-Fe electrode, which was even lower, to that of 0.9 nAh/g of the glassy carbon bare electrode.

It was confirmed that both Ni loading and MWCNTs loading have an impact on the current response, charge-discharge voltages and discharge capacity. A maximum current density and discharge current was reached when a 4wt% nickel was loaded. A decrease in current density and discharge current was observed for nickel loading of higher than 4wt%. Thus suggests a possible decrease in surface area of the adsorbed material on the surface of the electrode for hydrogen storage. As more MWCNTs were added, a decrease in current density was observed. A 2wt% MWCNTs gave higher discharge current and this was possibly due to less hindrance on the surface of the electrode for hydrogen to diffuse.

It was shown that calcining the metal nanoparticles result in particles agglomeration, as confirmed by Transmision electron microscopy (TEM). This resulted in a decrease in surface area of the working electrode. A low current response was observed compared to the uncalcined Ni nanoparticles. The highest exchange current density was obtained while using a GCE-MWCNT-Ni_{cal} as compared to the GCE-MWCNT-Ni_{uncal} electrode. The applied discharge current in CPE was also shown to have influence on the discharge capacity. An increase in discharge capacity for the GCE-MWCNT-Ni (2wt% MWCNTs and 4wt% Ni) electrode was observed as more discharge current was applied. A decrease in discharge capacity for hydrogen was observed as more content of the MWCNT-Ni_{uncal} nanocomposite are added on the active surface area of the glassy carbon electrode.

PRESENTATIONS AND PUBLICATIONS

Poster presentation

Catalysis Society of South Africa (CATSA), at Goudini Spa, Cape Town, South Africa; November 2009: Electro-catalytic storage of hydrogen in nickel oxide decorated carbon nanotubes. *P.M Masipa* and *T. Magadzu.*

Publication

P.M Masipa and T. Magadzu, Electrochemical storage of hydrogen in nickel oxide decorated multi-walled carbon nanotubes at the glassy carbon bare electrode, to be submitted.

P.M Masipa and T. Magadzu, The effect of MWCNTs, Ni nanoparticles and calcined Ni nanoparticles in the MWCNTs-Ni nanocomposite electrode on the current response, charge-discharge voltage and discharge capacity for hydrogen storage, to be submitted.

P.M Masipa and T. Magadzu, Electrochemical activity of metal oxides and metal nanoparticles decorated multi-walled carbon nanotubes for hydrogen storage at the glassy carbon bare electrode, to be submitted.

TABLE OF CONTENTS

LIST OF FIGURES

LIST OF ABBREVIATIONS

ACNTs	=	As-prepared Carbon Nanotubes
Ag/AgCl	=	Silver/Silver Chloride Reference Electrode
Ar	=	Argon
ASA	=	Active Surface Area
BET	=	Brunauer-Emmett-Teller
BPPGE	=	Basal Plane Pyrolytic Graphite Electrode
Cal	=	Calcined
CCVD	=	Catalytic Chemical Vapor Deposition
CD	=	Charge-Discharge
CE	=	Counter Electrode
CNTs	=	Carbon Nanotubes
Co	=	Cobalt
CO	=	Carbonyl
CO_2	=	Carbon dioxide
COOH	=	Carboxylic acid
CP	=	Chronopotentiometry
CPE	=	Controlled-Potential Electrolysis
Cu	=	Copper nanoparticles
$Cu(NO_3)_2 * 2.5H_2O$	=	Copper (II) nitrate pentahemihydrate

CuO	=	Copper (II) Oxide
CV	=	Cyclic Voltammetry
DI	=	Distilled/ De-ionized
DMF	=	N, N-Dimethylformamide
EIS	=	Electrochemical Impedance Spectroscopy
ESR	=	Equivalent Series Resistant
Fe	=	Iron nanoparticles
Fe_2O_3	=	Iron (III) Oxide
FTIR	=	Fourier-Transform Infrared
$Fe(NO_3)_3 * 9H_2O$	=	Iron (III) nitrate nonahydrate
FePc	=	Iron Phthalocyanine
GCE	=	Glassy Carbon Electrode
H^+	=	Hydrogen atom
H_2	=	Hydrogen gas
H_2O	=	Water
H_2SO_4	=	Sulphuric acid
HNO_3	=	Nitric acid
KBr	=	Potassium Bromide
KCl	=	Potassium Chloride
KOH	=	Potassium Hydroxide
LiOH	=	Lithium Hydroxide

LSV	=	Linear Square Voltammetry
Mn	=	Manganese
MWCNTs	=	Multi-Walled Carbon Nanotubes
$NaBH_4$	=	Sodium Borohydride
NaCl	=	Sodium Chloride
NaOH	=	Sodium Hydroxide
Ni	=	Nickel nanoparticles
$Ni(NO_3)_2 * 6H_2O$	=	Nickel (II) nitrate hexahydrate
NiO	=	Nickel (II) Oxide
OH^-	=	Hydroxyl ion
O_2	=	Oxygen
pH	=	Hydrogen potential
Pt	=	Platinum
PTFE	=	Polytetrafluoroethylene
RE	=	Reference Electrode
SEM	=	Scanning Electron Microscopy
SWCNTs	=	Single-Walled Carbon Nanotubes
TEM	=	Transmission Electron Microscopy
Uncal	=	Uncalcined
VLS	=	Vapor-Liquid-Solid
VS	=	Vapor-Solid

WE	=	Working Electrode
Wt%	=	Percentage by Weight
XRD	=	X-Ray Diffraction

CHAPTER 1

General Introduction

1.1 Historical background

Hydrogen has been considered as the potential alternative energy source for the present expensive and non-environmentally friendly fossil fuels [1]. At present, the main drawback in using hydrogen as a fuel is the lack of proper hydrogen storage material, thus an on-going research activities are focused on the development of advanced hydrogen storage material [2]. Hence, hydrogen can be used as a fuel to power transport vehicles and portable electronic devices. The advantage of hydrogen as energy source is that its combustion product is water. In addition hydrogen can be easily regenerated [3, 4]. For this reason, a suitable hydrogen storage system is necessary, satisfying both the volume and weight limitations [5].

Many alloys are able to store hydrogen reversibly, but the gravimetric storage density is too low for any practical applications [6]. Theoretical studies have predicted that interaction of hydrogen with carbon nanotubes can occur by both physisorption and chemisorption of hydrogen on the exterior and perhaps in the interior surface. Hence, the carbon nanotubes appear to be the ultimate solution due to their chemical stability, large surface area, low density and hollowness [7, 8].

Carbon nanotubes have attracted much attention in electrochemistry as both the catalyst and the energy storage materials [9]. Their application as energy storage is based on their high surface area, pore size and electrical conductivity. They are commonly used in fuel cells, batteries and other electrochemical applications [10]. Because of their cylindrical, hollow geometry and nanometer-scale

diameter, it has been predicted that carbon nanotubes can store a liquid or a gas in the inner cores through a capillary effect.

It has been reported that the storage capacity of the carbon nanotubes can be improved by the defects sites on the surface [11]. In the defective sites, hydrogen atom is stored. The atomic storage of hydrogen is due to the dangling bonds present at the defects sites. The presents of small amount of catalytic impurities such as nickel and copper in carbon could dissociate the hydrogen molecule to hydrogen atoms, thereby enhancing the chemisorption of hydrogen at moderate conditions and reasonable conditions [12].

1.1.1Synthesis of carbon nanotubes

In 1999, Liming Dai *et al.* [13] prepared well-aligned carbon nanotubes films by the pyrolysis of iron (II) phthalocyanine, $FeC_{32}N_8H_{16}$ (designated FePc), which contains both the metal catalyst and the carbon source required for carbon nanotubes growth. The pyrolysis was performed under Ar/H_2 at 800-1100 ^oC using an appropriate substrate in a flow reactor consisting of a quartz glass tube and a dual furnace fitted with independent temperature controllers. The resulting carbon nanotubes appeared on the substrate as a black layer, which could be scrapped off from the substrate as powder [13]. The synthesized CNTs were found to have a high surface area and porous structure, desirable for hydrogen storage. Liu *et al*. [14] used the same method to prepare bamboo-like carbon nanotubes in 2001.

1.1.2 Metal nanoparticles decorated carbon nanotubes

In 2007, Hsieh *et al*. [15] investigated the electrochemical activity of Ni-attached carbon nanotubes electrodes for hydrogen storage in the alkali electrode.

MWCNTs were prepared by CCVD method, using ethylene and Ni particle as a carbon precursor and catalyst respectively. Chemical oxidation method was employed to purify the as-prepared MWCNTs. Oxidized MWCNTs were functionalized with Ni nanoparticles using an ionic adsorption method followed by direct hearting. They measured the capacity of the electrodes by charging the capacitors to a voltage of -0.2 V vs. reference electrode at a constant discharge current density. From the CV results, the adsorption/desorption peaks of hydrogen were observed between -0.9 V and -10 V vs. SCE. With increasing the sweep rate, the peaks current were nearly proportional to the rates. The specific current density was found to increase with the Ni loading onto the MWCNTs. From the charge-discharge studies, it was found that the capacitance is directly proportional to the Ni nanoparticles loading on the MWCNTs surface. It was also found that MWCNTs coated with Ni nanoparticles significantly increased the hydrogen storage capacity in MWCNTs [16].

Very few investigations have been reported on the storage of hydrogen in metal oxides decorated CNTs, though metal oxides like NiO and CuO also have high surface area and porous structures for high amount of hydrogen storage [17]. There is therefore a need to study the effect of metal oxides and metal nanoparticles on the surface of the CNTs so as to improve the storage capacity for hydrogen. In this dissertation, carbon nanotubes were synthesized and their applications in hydrogen storage were investigated. Different metal nanoparticles (Cu, Fe and Ni) and metal oxides (CuO, Fe_2O_3 and NiO) were synthesized and dispersed on the carbon nanotubes surfaces, and the investigation of their hydrogen adsorption and desorption processes was undertaken, using an electrochemical technique.

1.2 Aim of the study

The aims and objectives of the study as proposed in the proposal are as follows:

(a) To prepare or synthesize carbon nanotubes using iron (II) phthalocyanine.

(b) To synthesize metal nanoparticles (Cu, Fe and Ni) and metal oxides (CuO, Fe_2O_3 and NiO).

(c) To purify the as-prepared carbon nanotubes and decorate them with metal nanoparticles (Cu, Fe and Ni) and metal oxides (CuO, Fe_2O_3 and NiO).

(d) To characterize carbon nanotubes and metal nanoparticles decorated CNTs using spectroscopic (XRD and FT-IR), microscopic (TEM and SEM) and electrochemical techniques (CV, LSV, CP and CPE).

(e) To modify the glassy carbon bare electrode with metal oxides and metal nanoparticles decorated CNTs and test these materials for hydrogen storage using electrochemical techniques.

1.3 Dissertation structure

In this dissertation the electrochemical activity of metal oxides (CuO, Fe_2O_3 and NiO) and metal nanoparticles (Cu, Fe and Ni) decorated multi-walled carbon nanotubes (MWCNTs) for hydrogen storage at the glassy carbon electrode (GCE) have been investigated. A short review of the literature reports on the synthesis, structure and properties of carbon nanotubes and metal nanoparticles is given in Chapter 2.

The literature review was reported with respect to the following topics: (a) synthesis, structure and properties of CNTs, metal nanoparticles and metal oxides, (b) general applications of CNTs in energy storage, (c) Hydrogen

economy and (d) electrochemical application of carbon nanotubes in hydrogen storage. The above undertaken topics were reviewed with respect to the work done in this dissertation.

Synthesis of carbon nanotubes, metal nanoparticles and metal oxides were undertaken. The results of these studies are presented in Chapter 3.

Characterization results for the carbon nanotubes, metal oxides, metal nanoparticles and multi-walled carbon nanotubes decorated with metal oxides (CuO, Fe_2O_3 and NiO) and metal nanoparticles (Cu, Fe and Ni), are presented in Chapter 4. These nanocomposites material were coated on the glassy carbon electrode. Electrochemical activity such as current response, charge-discharge voltage and discharge capacities of multi-walled carbon nanotubes decorated with metal oxides (CuO, Fe_2O_3 and NiO) and metal nanoparticles (Cu, Fe and Ni) were undertaken. The GCE-MWCNT-Ni electrode gave the highest discharge capacity. These results are fully reported in Chapter 4.

The impact of MWCNTs loading and the effect of Ni loading on the current response, charge-discharge voltage and discharge capacity using the MWCNTs-Ni nanocomposite for hydrogen storage were investigated. These results are presented in Chapter 4.

The effect of calcining Ni on the current response, charge-discharge voltage and discharge capacity was studied. The effect of applied discharge current on the discharge capacity of the GCE-MWCNT-Ni for hydrogen storage was also investigated. Finally, the effect of the amount of MWCNTs-Ni modifiers on the current response, charge-discharge voltages and discharge capacity for hydrogen storage was undertaken and the results for this study are also presented in Chapter 4.

In this dissertation, figures and schemes are integrated within the text. References are fully written at the end of the respective chapters. Overall conclusions for the study are presented in Chapter 5.

1.4 References

[1] L.X. Zheng, Nature Materials, 3 (2004) 673-676.

[2] J.W. Mintmire, B.I. Dunlap and C.T. White, Physical Review Letters, 68 (1992) 631-634.

[3] C. Dekker, Physics Today, 52 (1999) 22-28.

[4] R. Martel, V. Derycke, C. Lavoie, J. Appenzeller, K.K. Chan, J. Tersoff and P. Avouris, Physical Review Letters, 87 (2001) 256-805.

[5] T. Collins, G. Philip and P. Avouris, Scientific American, 45 (2000) 67-69.

[6] E. Flahaut, R. Bacsa, A. Peigne and C. Laurent, Chemical Communications, 12 (2003) 1442-1443.

[7] L. Liu, G.Y. Guo, C.S. Jayanthi and S.Y. Wudate, Physical Review Letters, 88 (2002) 206-217.

[8] S. Belluci, Solid-State Physics, 2 (2005) 34-35.

[9] H.G. Chae and S. Kumar, Journal of Applied Polymer, 100 (2006) 791-792.

[10] B.G. Demczyk, Y.M. Wang, J. Cumings, M. Hetman, W. Han, A. Zettl and R.O. Ritchie, Materials Science and Engineering, 334 (2003) 173-174.

[11] M. Meo and M. Rossi, Composites Science and Technology, 66 (2006) 1597-1598.

[12] S.B. Meo and R. Andrews, Critical Review of Solid-State Material Science, 26 (2001) 145-146.

[13] D. Liming, H. Showing and M. Albert, Journal of physical chemistry B, 103 (1999) 4223-4227.

[14] L. Yungi and W. Xianbao, Carbon, 39 (2001) 1533-1536.

[15] Y. Hsieh, H. Chien-Te and C. Yun-Wen, International Journal of Hydrogen energy, 32 (2007) 3457-3464.

[16] J.E.B. Randles, Transcript Faraday Society, 44 (1948) 327-328.

[17] K.B. Kim and I.H. Kim, Electrochemical Solid-State, 4 (2001) 62-64.

CHAPTER 2

Literature Review

2.1 Structural features of carbon nanotubes (MWCNTs and SWCNTs)

Many different structures of fullerenes exist, with the best known being SWCNTs and MWCNTs. Single walled carbon nanotubes (SWCNTs) are considered as a long wrapped grapheme sheets. They nearly have a one-dimensional structure [1]. Multi-walled carbon nanotubes can be considered as a collection of concentric SWCNTs with different diameters. Their length and diameter differ from that of SWCNTs and as results, their properties tend to differ [2].

2.2 Synthesis of carbon nanotubes

2.2.1 Laser evaporation technique

This method was discovered in 1995 by a Smalley‘s group at Rice University [3]. The method involves the use of pulsed or continuous laser to vaporize a graphite target in an oven at high temperatures [4, 5]. The main difference between pulsed laser and continuous laser is that the pulsed laser demands a much high light intensity. The oven is filled with helium or argon gas in order to keep the pressure at 500 Torr. A very hot vapor plume forms, then expands and cools rapidly. As the vaporized species cools, small carbon molecules and atoms quickly condense to form large clusters, possibly including fullerenes. The

catalysts begins to condense, but more slowly at first, and attach to carbon clusters and prevent their closing into the cage structures [6].

2.2.2 Arc discharge technique

The arc discharge method is one of the most common methods and easiest way to produce carbon nanotubes. However, it is a technique which produces a mixture of components and requires separating nanotubes from the soot and the catalytic metals present in the crude product. This method creates nanotubes through arc-vaporization of two carbon rods placed end to end, separated by 1mm, in an enclosure that is usually filled with inert gas at low pressure. A direct current of 50 to 100 A driven by approximately 20 V creates a high temperature discharge between the two electrodes. The discharge vaporizes one of the carbon rods and forms a small rod shaped deposit on the rod producing nanotubes in high yield depending on the uniformity of the plasma arc and the temperature of the deposit form on the carbon electrode [7]. Depending on the exact technique, SWCNTs and MWCNTs can be selectively grown.

2.2.3 Catalytic chemical vapor deposition (CCVD) technique

Chemical vapor deposition (CVD) synthesis is achieved by putting a carbon source in the gas phase and using an energy source, such as plasma or resistively heated coil to transfer energy to a gaseous carbon molecule [8]. Commonly used gaseous carbon sources include methane, carbon monoxide and acetylene. The energy used is to crack the molecule into reactive atomic carbon. Then, the carbon diffuses towards the substrate, which is heated and coated with a catalyst where it will bind [9].

In 2003, single and double-walled carbon nanotubes were synthesized by Lee *et al*. [10] using the catalytic chemical vapor deposition method. The method decomposes the methane gas to solid-state carbon nanotubes. The synthesis of carbon nanotubes was carried out by catalytic reaction of CH_4 and Fe-Mo catalyst in a fixed bed reactor. A mixture of $Fe(NO_3)_3.9H_2O$ and Mo solution was dissolved in distilled water for 1 h. The mixed Fe-Mo solution was introduced to the suspension of Al_2O_3 powder and distilled water followed by sonication for 1 h. The molar ratio of the catalyst was $Fe:Mo:Al_2O_3$ = 1:0.1:13. After drying, the material was baked at 150 ^oC for 15 h in a vacuum ambient and then ground in mortar to break the chunks into powder. About 100 mg $Fe\text{-}Mo/Al_2O_3$ catalyst was placed in the quartz boat that was inserted into the center of a quartz tube. The quartz tube was then mounted in an electrical tube furnace, and it was heated to 950 ^oC in Ar atmosphere. Subsequently, the mixture of Ar and CH_4 gas was introduced into the quartz tube for the production of nanotubes materials. The synthesis of carbon nanotubes was conducted at 950 ^oC for 30 min in atmospheric pressure. The flow rate of CH_4 and Ar was 100 and 500 ml/min, respectively. The flow of Ar/CH_4 was maintained for 30 min before the furnace was cooled to room temperature in Ar atmosphere [10].

2.3 Materials used for carbon nanotubes growth

2.3.1 Catalysts used for carbon nanotubes growth

The catalyst used has a strong effect on carbon nanotubes diameter, growth rate, wall thickness, morphology and microstructure. The catalysts used for CNTs growth are usually first row transition metal such as Ni, Fe or Co [11].

2.3.2 Carbon source used for carbon nanotubes growth

Gaseous carbon sources such as methane, carbon dioxide, ethylene, and alcohol containing compounds are usually preferred. Solid state materials such as iron (II) phthalocyanine and ferrocene are used.

2.4 Mechanisms of carbon nanotubes growth

The way carbon nanotubes form is not clearly known. One of the mechanisms proposed consists of three steps. First, the precursors bind to the surface of the metal catalyst particles. From this metastable carbide particle, a rod-like carbon is formed rapidly. Secondly there is a slow graphitization of its wall. This mechanism is based on in-situ TEM studies [12].

2.5 Purification of carbon nanotubes

The as-prepared CNTs soot contains a lot of impurities that tend to hinder their applications. The main impurities are amorphous carbon, graphite sheets and metal catalyst. These impurities interfere with most of the desired properties of the CNTs. Several purification techniques are briefly discussed.

2.5.1 Acid treatment

The acid treatment is effective in removing the metal catalyst [13]. Firstly, the surface of the metal catalyst is exposed by oxidation or sonication. The metal catalyst is then exposed to acid and solvated. The CNTs remains in suspended

form. The acids used are HNO_3 and H_2SO_4. Nitric acid has an effect on the metal catalyst and has no effect on the CNT structure [14, 15]. The acid treated carbon nanotubes will results in the formation of COOH, OH or CO groups on the sidewalls.

In 2003, Zhao *et al*. [16] purified single-walled carbon nanotubes by the acid treatment method. They refluxed 1 g of as-prepared SWCNTs in a 150 mL of 3 M nitric acid for 6 h. After refluxing, the mixture was cooled to room temperature and then diluted with distilled water. A 1.2 µm pore-sized membrane was then used to filter the carbon nanotubes. The product on the membrane was washed thoroughly with distilled water and then dried at room temperature. Nitric acid act to oxidize carbon atom at the end of SWCNTs and remove the metal nanoparticles impurities [16].

2.5.2 Ultrasonication

This technique separates particles according to their ultrasonic vibrations. Agglomerates of different nanoparticles will be forced to vibrate and will become more dispersed tubes in the system. The separation of the particles is highly dependable on the surfactant, solvent and reagent used [17, 18].

2.5.3 Micro filtration

Micro filtration is based on size or particle separation. CNTs and small amount of carbon nanoparticles are trapped in a filter. The other nanoparticles such as catalyst metal, fullerenes and carbon nanoparticles pass through the filter [19].

2.5.4 Chromatography

This technique is mainly used to separate small quantities of CNTs into fractions with small length and diameters distribution. The CNTs are run over a column with porous materials, through which CNTs will flow [20]. The number of pores the CNTs will flow depends on their size. This means that, the smaller the molecule, the longer the pathway to the end of the column will be and that the larger molecules will come out first [21, 22].

2.5.5 Annealing

High temperature (600 ^{o}C-1600 ^{o}C) treatment of CNTs will result in rearrangement and defects sites of CNTs being consumed [23, 24]. The high temperature causes the graphitic carbon and the short fullerenes to pyrolyse. At high temperature treatment (1600 ^{o}C), the metal will be melted and can be removed [25].

2.6 Properties of carbon nanotubes

2.6.1 Electrical Conductivity

Carbon nanotubes with a small diameter are either semi-conducting or metallic depending on their chirality. The differences in the conducting properties are caused by the molecular structures that result in a different band structure and thus a different band gap [26].

2.6.2 Mechanical strength

Carbon nanotubes have a very large young modulus in their axial directions. They are very flexible because of their great length.

2.6.3 Optical activity

Optical activity of the CNTs depends on their length. If the CNTs become great in length, the optical activity of chiral nanotubes disappears. The use of optical activity might results in optical devices in which CNTs play an important role [27].

2.6.4 Chemical reactivity

The reactivity of the CNTs is enhanced by their curvature surface as compared to the graphene sheet. CNTs reactivity is related to the pi-orbital mismatch caused by an increase curvature. As a result, a smaller nanotubes diameter results in increased reactivity [28].

2.7 Metal nanoparticles

Metal nanoparticles display novel physical and chemical properties due to surface effect, where most of the particle atoms are just surface atoms [29]. These novel properties have put metal nanoparticles to play an interesting role in materials technology, biomedicines, catalysis, sensing, environmental science, energy storage etc. The properties of the metal nanoparticles are highly influenced by the preparation methods and conditions, which results in particles

of various size, shape and surface stabilization [30, 31]. Moreover, the surface/interface interactions have their signatures in the properties investigated [32, 33]. It is known that nanosize powders of metals show an increased reactivity, compared to compact metals. For example, reactions that do not occur in the presence of some metals readily proceed in the presence of metal nanopowders [34].

2.7.1 Synthesis of metal nanoparticles by reduction method

Almost all properties of nanoparticles are due to their small sizes [35]. Of late, in addition to size effect, the shape of the particles has also drawn special attention, mainly to explore the application of these particles in the field of nanotechnology. Therefore, attempts are being directed to gain precise control of the size and shape of various types of nanoparticles systems during their syntheses [36]. The fact is that these syntheses result in a mixture of particles, in terms of both size and shape. The most common method employed for their preparation is the reduction of metal ions in solution, usually in the presence of a particle-stabilizer [37].

The synthesis of metal nanoparticles by reduction method involves the use of a strong reducing agent such as sodium borohydride to reduce metal nitrate salt to form metal nanoparticles. The reducing agent is added drop-wise into the solution while subsequently stirring at a known controlled rate [38, 39].

In 2006, Zhang *et al*. [40] used the reduction method to synthesize zero-valent iron nanoparticles. Iron nanoparticles were conducted in a flask reactor with three open necks. The central neck was housed with a turnable mechanical stirrer at 400 rpm. Through titration at a rate of 0.625 mL/s, the borohydride was introduced to reduce ferric ion ($Fe^{3+)}$ to zero-valent iron (Fe^{o}), according to the following reaction:

$$4Fe^{3+} + 3BH_4^- + 9H_2O \longrightarrow 4Fe^{o} + 3H_2BO_3^- + 12H^+ + 6H_2$$ **(Eq. 2.1)**

Typically, 1:1 volume ratio of $NaBH_4$ (0.2 M) and $FeCl_3.6H_20$ (0.05 M) were vigorously mixed in the flask reactor for additional 30 min after titration. Excessive borohydride (0.2 M) was applied to accelerate the synthesis reaction. Experimental parameters such as pH, reactant concentrations, stirring speed, titration rate, reaction time and external temperature can, to some extent, influence the composition and surface properties of the produced iron particles and hence need to be maintained constant in the experimental to produce consistent sample results. The generated iron particles were harvested with vacuum filtration and stabilized with a large volume of deionized water to wash, and at the end, with diluted ethanol. Thin layer of ethanol on top of the iron nanoparticles helps to preserve the nanoparticles [40].

In 2007, silver nanoparticles were synthesized by Bahadory and co-workers [41]. They added 10 mL volume of 1.0 mM silver nitrate drop-wise (about 1 drop/second) to 30 mL of 2.0 mM sodium borohydride solution that has chilled in an ice bath. The reaction mixture was stirred vigorously on a magnetic stir plate. The entire addition took about three minutes, after which the stirring was stopped and the stir bar removed. Reaction conditions including stirring time and relative quantities of reagents (both the absolute number of moles of each reactant as well as their relative molarities) was carefully controlled to obtain stable yellow colloidal silver [41].

2.7.2 Application of metal nanoparticles in hydrogen storage

Metal nanoparticles technology has received considerable attention for their potential applications and properties such as high surface area, high conductivity and sensitivity to applied potential in electrochemical experiment.

Electrochemical properties of metal nanoparticles in alkaline electrolyte have attracted close attention to researchers, for metal nanoparticles-based catalysts in such electrolytes are widely used for accelerating catalytic and electrocatalytic processes [42]. Metal nanoparticles such as nickel, has been applied in hydrogen storage to improve the storage capacity of CNTs.

In 2007, Hsieh *et al*. [43] investigated the electrochemical activity of Ni-attached carbon nanotubes electrodes for hydrogen storage in the alkali electrode. MWCNTs were prepared by CCVD method, using ethylene and Ni particle as a carbon precursor and catalyst respectively. Chemical oxidation method was employed to purify the as-prepared MWCNTs. Oxidized MWCNTs were functionalized with Ni nanoparticles using an ionic adsorption method followed by direct hearting. They measured the capacity of the electrodes by charging the capacitors to a voltage of -0.2 V vs. reference electrode at a constant discharge current density. From the CV results, the adsorption/desorption peaks of hydrogen were observed between -0.9 V and -10 V vs. SCE. With increasing the sweep rate, the peaks current were nearly proportional to the rates. The specific current density was found to increase with the Ni loading onto the MWCNTs. From the charge-discharge studies, it was found that the capacitance is directly proportional to the Ni nanoparticles loading on the MWCNTs surface. It was also found that MWCNTs coated with Ni nanoparticles significantly increased the hydrogen storage capacity in MWCNTs [44].

Metal nanoparticles such as Cu, Fe and Ni was employed in this dissertation to explore their electrochemical role in storage of hydrogen in CNTs. Nickel nanoparticles were chosen due to recent reports showing a significant increase in hydrogen storage by nickel decorated carbon nanotubes. Copper nanoparticles were chosen due to copper having a high electrical conductivity than other elements. Lack in interest for researchers to study hydrogen storage in iron nanoparticles decorated CNTs prompted us to investigate their electrochemical properties towards hydrogen storage.

2.8 Metal oxides

Metal oxides are probably the most diverse and rich materials that have important applications in science and technology for ferromagnetism, ferroelectricity, piezoelectricity, superconductivity, magnetoresistivity, photonics, separation, catalysis, environmental engineering, etc. [45]. Functional oxides have two unique structural features: switchable and/or mixed cation valences, and adjustable oxygen deficiency, which are the best bases for creating many novel materials with unique electronic, optical, and chemical properties. The oxides are usually made into nanoparticles or thin films in an effort to enhance their surface sensitivity, and they have recently been successfully synthesized into nanowire-like structures [46].

The effect of metal oxides (CuO, Fe_2O_3 and NiO) and metal oxides decorated CNTs towards electrochemical hydrogen storage will be investigated.

2.8.1 Synthesis of metal oxides by calcination (Direct heating)

Growth of oxides nanostructures is an important part of nanomaterial research, and it is the fundamental for fabricating various nanodevices. Metal oxides can be synthesized by hydrothermal synthesis, vapor-liquid-solid (VLS), vapor-solid (VS) and composite-hydroxide mediated synthesis [46]. Metal oxides can also be prepared from the solid metal nitrate by direct heating at high temperatures. The nitrate group decomposes to form metal oxide with the water evaporating.

In 2005, Lee *et al*. [47] prepared high surface area metal oxides by calcination method. In the preparation of the metal oxide sorbents having high surface area, a granular type of activated carbon was used as a matrix and a metal oxide was supported by an impregnation method. Zinc nitrate ($Zn(NO_3)_2*6H_2O$, Aldrich Co.)

was used as a precursor to formulate the metal oxides. The prepared zinc nitrate/activated carbon sorbents were dried to remove moisture from the material at 150 °C. The dried sorbents were then calcined for 2 hrs at 500 °C. [47].

2.9 Methods of decorating carbon nanotubes by metal nanoparticles and metal oxides

An efficient hydrogen storage medium is an inevitable component for the adoption of hydrogen as an energy carrier. Hydrogen in the solid matrices like metals, intermetallics, porous solids and carbon materials appears to be appropriate option [48]. In the case of metals and inter-metallics, the factors adverse to storage purpose are either limitation in storage capacity or the reversibility of stored hydrogen under favorable experimental conditions [49]. After the report by Rodriguez *et al.* [50] that the carbon nanomaterials can store up to nearly 67wt% of hydrogen, the research in this area took a dramatic turn with a variety of investigations dealing with modification of carbon materials like metal loading, preparing carbon materials in different geometrical forms with phase purity and addition of metal oxides [51].

To functionalize the CNTs with metal nanoparticles, an ionic adsorption followed by a direct heating can be adopted. This procedure involve the mixing of CNTs with a known concentration of metal ionic nitrate, and then stirred under argon (Ar) atmosphere at a certain temperature for a known period of time. This wet process enables metal ions to interact with the surface oxygen groups, forming metal ionic adsorption on the CNTs surface. Then, the ionic-adsorbed CNTs tend to be separated from the metal-salt solution by using a filtration apparatus. The direct heating process can be performed at high temperature under mixed H_2/Ar (1/99 in v/v) atmosphere, ensuring reduction of metal oxides to metal particles [52-54].

A known mass of oxidized CNTs can also be sonicated with a known mass of metal nanoparticles or metal oxides with the use of N, N-dimethylformamide (DMF) as a binder. This enables metal oxides or nanoparticles to bind on the surface of the oxidized CNTs as confirmed by current response using cyclic voltammetric studies.

In 2003, Rao *et al*. [55] prepared the working electrode by mixing 10 mg of the carbon nanotubes samples with Cu powder in a ratio of 1:3 with a polytetrafluoroethylene (PTFE) binder. The putty form of the mixture was mechanically pressed on to a current collector (Ni mesh) at room temperature. The electrode was then sintered at 200 ^{o}C for about 1 h under vacuum. The geometric surface area of the electrode was *ca*. 2 cm^{2} [55].

2.10 Structural characterization of the carbon nanotubes, metal nanoparticles and metal oxides

2.10.1 Transmission electron microscopy (TEM)

This technique is used to determine the micro-structural information of the CNTs and coated metal nanoparticles on CNTs. Samples for TEM test are prepared by the drop method. Information at the atomic level will also be given [56]. It is a technique operated at a high resolution where the electron is transmitted through the sample owing to the interest in the internal details thus revealing the morphology (size, shape and arrangement of the particles), the crystallographic information (the atom arrangement) and the compositional information (the elemental composition) of the material examined. The operation of a TEM is similar to that of a slide projector; however, it shines a beam of electrons, instead of light, generated from an electron gun. This stream of electrons is focused by a coherent beam that is restricted by a condenser aperture. The beam striking the sample transmits portions of the sample which are focused by the objective lens

into an image that is projected onto a screen. There are dark and light areas of the image representing the more densely packed section which allowed fewer electrons to pass through and less densely packed section which allowed more electrons to pass through, respectively [56].

2.10.2 Scanning electron microscopy (SEM)

Scanning electron microscopy is used to determine the powder morphology and microstructure of the sample. This technique is used to scan the dry surface of the material where one is only interested in the surface details. The operation of the SEM is as follows: At the top of a SEM column an electron gun generates a beam of electrons which are attracted through the anode, condensed (condenser lens) and focused (objective lens) as a fine point onto the sample. These electrons are collected by a secondary detector or a backscatter detector. The secondary electron detector produces a clear and focused topographical image of the sample whereas the backscatter electron detector reflects an elemental composition of the sample and is used for energy dispersive X-ray analysis [56].

2.10.3 X-ray diffraction (XRD)

It is used to characterize the crystallinity and phase purity of the solid products. Information about the arrangement of surface atom with respect to each other can be obtained; as well as underlying atoms in a solid. It also gives information on particle or crystalline size by the use of Scherrer Formula [56].

2.10.4 Fourier-transform infrared (FT-IR)

Fourier-transform infrared technique is used to determine the nature of acid site (Lewis and Bronsted types) present on the CNTs. CNTs samples are degassed overnight at about 300 ^{o}C and above under vacuum. The FT-IR measurements are made on pellets (5% CNTs in KBr) to record the framework of COOH, OH and/ or CO groups in a suitable frequency [57, 58].

2.11 The hydrogen economy

The never-ending stories on an alternative energy supply for the cleaner environment, recently related with the efforts of decrease global CO_2 emissions, has been revived by the steep increase in oil prices and the parallel controversy about the potential and public acceptance of the nuclear energy [59, 60]. Thus, it is now the right time for the scientific community and energy producers to synthesize their knowledge in order to achieve realistic solutions towards cleaner energy systems. Taking into account the concerns that are related to environmental protection, security in the energy supply and the utilization of energy sources that promote the economic growth of societies, the concept of a hydrogen economy era is moving beyond the realm of scientists and engineers into the political and business leaders. Interest in hydrogen, the simplest and most abundant element in the universe, is also emerging due to technical advances in fuel cells- the potential successor to batteries in portable electronics, power plants, and the internal combustion engine [61].

2.11.1 Hydrogen production

Hydrogen gas (H_2) is almost everywhere, but unfortunately it is hard to find it on earth as a separate element. Instead, it is primarily chemically bonded with oxygen in water, with carbon in a range of hydrocarbon fuel and in plants, animal and other form of life. Hydrogen bound in water and organic forms account for more than 70% of the earth‘s surface [62]. Once extracted, this colourless, odourless and tasteless element becomes a useful feedstock to a variety of industrial activities and a potential fuel sufficient to energize all aspects of society, from homes to electric utilities to business and industry to transportation. The following methods are used to produce hydrogen:

2.11.1.1 Hydrogen from fossil fuels

Fossil fuels such as coal, natural gas and oil are used to produce hydrogen. Carbon dioxide produced as a by-product should be captured and stored to ensure a sustainable (zero emission) process.

2.11.1.2 Hydrogen from splitting of water

Hydrogen can be produced from splitting of water through various processes ranging from water electrolysis, photo (solar) electrolysis and photo-biological production to high-temperature water decomposition. Water electrolysis is the electrochemical process, which involve the use of electricity to split water into its components such as hydrogen and oxygen as depicted in the following equation:

$$H_2O + \text{electricity} \longrightarrow H_2 + \tfrac{1}{2}\, O_2 \qquad \textbf{(Scheme 2.1)}$$

About 4% of the world‘s hydrogen is produced from water electrolysis [63]. This process is cost effective for the production of extremely pure hydrogen in small amounts; however, it remains expensive at large scales, primarily due to electricity, which currently cost more compared to corresponding fossil-fuel feedstock. The total energy that is needed for water electrolysis increases slightly with temperature, while the required electrical energy decreases [64, 65].

2.11.1.3 Hydrogen from biomass

Biomass is a renewable energy source that could play a substantial role in a more diversified and substantial energy mix. It may be defined as any renewable source of fixed carbon, such as wood, wood residues, agricultural crops and their residues. Industrial and municipal wastes are often considered as biomass due to their high percentage of food waste [66].

2.11.2 Hydrogen storage forms

Commercially viable hydrogen storage is considered as one of the most crucial and technically challenging barriers to the widespread use of hydrogen as an effective energy carrier [67]. It is expected that hydrogen economy will require two basic technological frameworks of hydrogen storage systems, one for stationary and another for mobile applications. Mobile applications are more demanding, as they require the following [68]:

- High volumetric and gravimetric hydrogen densities
- Low operating pressures
- Operating temperatures in the range from -50 ^{o}C to -150 ^{o}C

- Fast kinetics for hydrogen charging and discharging
- Reversibility for many cycles during hydrogen charging-discharging
- Reasonable cost of a storage system

Types and properties of hydrogen storage media are as follows:

2.11.2.1 Compressed gas

Since hydrogen has a low energy density, it must be compressed to very high pressures to store sufficient amount of hydrogen, particularly for mobile applications.

2.11.2.2 Liquid hydrogen

Liquid hydrogen is stored in atmospheric pressures in cryogenic tanks at T = 20.3 K with a density of 70.8 g/l, which is nearly twice that of compressed hydrogen at 70 Mpa [69].

2.11.2.3 Solid hydrogen

Traditional method proposed through the use of advanced solid materials as hosting agents for the storage of hydrogen in atomic or molecular form. This type of hydrogen storage is often called solid hydrogen storage since hydrogen becomes part of the solid materials through some physicochemical bonding. Metal hydride and carbon nanotubes falls under solid materials mentioned [70, 71].

2.12 Electrochemistry: an overview

Electrochemistry can be defined as the study of chemical reactions used for the production of electric power or the use of electricity to influence the chemical processes usually occurring at the surface of the electrodes [72, 73]. Electric quantities such as current, potential and charge are measured during electrochemical experiments. These electric quantities are dependent on the chemical parameters. Electrochemical reactions are heterogeneous in nature as they take place at the interfaces, usually electrode-solution [74].

The study employed three (3) electroanalytical techniques, cyclic voltammetry (CV), chronopotentiometry (CP) and controlled potential electrolysis (CPE) with a three electrode systems. All electrochemical cells require at least two electrodes, since the potential of a given electrode can only be measured relative to another electrode, the potential of which must be constant (a reference electrode) [75, 76]. In potentiometric measurements (such as measurement of pH), there is no current through the cell, and these two electrodes are sufficient. It should be noted that many pH and ion-selective electrodes used in potentiometric measurements are combination electrodes, and- both electrodes are contained within the same body.

However, in a cyclic voltammetry experiment, an external potential is applied to the cell, and a current response is measured. Precise control of the external applied potential is required, but this is generally not possible with a two electrode system, due to the potential drop across the cell due to the solution resistance. Potential drop (E) = current (i) * solution resistance (R) and the polarization of the counter electrode that is required to complete the current measuring circuit. Better potential control is achieved using a potentiostat and a three electrode system, in which the potential of one electrode (working electrode) is controlled relative to the reference electrode, and the current passes between the working electrode and a third electrode (the counter electrode) [77, 78].

The working electrode is where the electrochemical reaction takes place and the reference and counter electrodes complete the electric circuit. The working electrode acts as a source or sink of electrons for exchange with molecules in the interfacial region (the solution adjacent to the electrode surface), and must be an electronic conductor. It must also be electrochemically inert (i.e. does not generate a current in response to an applied potential) over a wide potential range (the potential window). Commonly used working electrode materials in electrochemistry include platinum, gold, mercury, and glassy carbon. Other materials such as semiconductors and other metals are also used, for more specific applications.

The best reference electrode is the one whose potential does not shift from equilibrium (i.e. non polarizable) [79]. Therefore, to minimize its polarization, the reference electrode with a very large surface area is used. The reference electrode is always in contact with the concentrated solution of sodium chloride (NaCl) or potassium chloride (KCl), due to the fact that the potential of a chloride-containing reference electrode is sensitive to the chloride concentration. Therefore, the electrode must be stored with the frit immersed in a solution that is identical in composition and concentration to the reference electrode solution [79]. This work employed the glassy carbon as the working electrode, the platinum wire as the counter electrode and the silver-silver chloride as the reference electrode.

2.12.1 Potential electrochemical applications of carbon nanotubes for energy storage

Graphite, carbonaceous materials and carbon fibre electrodes are commonly used in fuel cells, batteries and other electrochemical applications. Advantages of using nanotubes for energy storage are their small dimensions, smooth surface topology and perfect surface specificity. The efficiency of fuel cells is determined

by the electron transfer rate at the carbon electrodes, which is fast on carbon nanotubes following ideal Nernstian behavior [80].

2.12.1.1 Hydrogen storage

Because of their cylindrical and hollow shape geometry and nanoscale diameter, it has been predicted that carbon nanotubes can store gasses in their inner core through capillary effect. As a threshold for economic storage, the department of energy has set storage requirements of 6.5% by weight as the minimum level for hydrogen fuel cells. In electrochemical hydrogen storage, atomic hydrogen is adsorbed on the surface of the CNTs, through chemisorption process [81].

In 1984, Vinden and co-workers [82] found out that large empty space particularly inside the single-walled nanotubes (SWCNTs) provided a possibility to be applied for hydrogen storage vehicles with large storage capacity. It was shown that CNTs have a high capacity, light mass and high stability, which may be applicable for portable electronics and moving vehicles. They also showed chemical stability and low mass density. Vinden *et al*. [83] estimated that 5% to 10% of hydrogen could be stored in bundles of SWCNTs, where H_2 molecules are physisorbed at the exterior surface of CNTs or interstitial spaces between CNTs, separating the intertube distance [83].

In 2000, Seung *et al*. [84] employed the electrochemical charge-discharge cycling method to study the adsorption of hydrogen in CNTs. CNTs-based composite electrodes were fabricated by mixing and grinding first with conductive Ni powders 99.8% for 50 min and later with the organic binder of polytetrafluoetylene PTFE for 20 min with a mixing composition ratio of CNT:Ni:PTFE in a 40:50:10 ratio. They made a pellet by pressing the mixture into a mold of diameter of 10 mm by 2000 atmospheric pressure. They inserted the pellet into Ni mesh and used it as working electrode. The counter electrode metal Ni was separated by a polymer separator. The voltage across the two electrodes

was measured in 6 M KOH solution as a function of time for 10 h, while maintaining a constant current at 0.4 mA. They proposed the following reaction in the working electrode:

$$CNTs + H_2O + e^- \xrightarrow{\text{charge}} CNTs.\ H + OH^-, \qquad \textbf{(Scheme 2.2)}$$

where hydrogen ions are inserted into CNTs during the charging process. It was found that repeating charge-discharge cycle, which involves activation process of working electrode, give rise to the saturation of charge-discharge storage capacity. They noted that several slopes appear in the discharge curves [85].

In 2001, Perng *et al*. [86] investigated the electrochemical storage of hydrogen in carbon nanotubes. They prepare carbon nanotubes by CCVD method using Co and/or Ni as the catalyst. They use nitric acid to remove the residual metallic particles for all samples, and then the CNTs were soaked with $Co(NO_3)_2$ at different atomic ratios, followed by reduction in H_2 at 300 ^oC for 30 min. The maximum discharge capacity of the as-prepared Co-CNT was 200 mAh/g, equal to an H/C value of 0.74wt%. After acid treatment, however, the hydrogen storage capacity of Co-CNT dropped to nearly zero. After decoration of acid treated CNTs with Co, the discharge capacity increased very significantly, and the cyclic stability is improved compared to as-prepared samples. They found out that the discharge capacity for as-prepared Ni-CNT was quite low compared to that of Co-CNT. However, a decrease was observed after removing the Ni metal catalyst. Although Ni is a good catalyst for hydrogen dissociation in alkaline solutions, in their studies, they reported that the catalytic effect of Ni was not as good as Co for the CNT electrode. Perng *et al.* [87] also investigated the electrochemical activity of the commercial CNTs with 95% purity. Their discharge capacity was very low. But after decoration with Co, the discharge capacity was increased markedly. The maximum discharge capacity reached 231 mAh/g when 10at% Co was deposited to the CNTs surface [88].

Ren *et al*. [89] investigated the electrochemistry of carbon nanotubes in 2004. Carbon nanotubes were prepared by CCVD method using acetylene. They deposited Ni nanoparticles on the substrate and used them as catalyst. Cyclic voltammetric analysis showed a rectangular shaped cyclic voltammograms over a wide range of scan rate. This meant that the charge and discharge processes are very fast at the interface between the carbon nanotubes electrode and the electrolyte solution [90].

In 2008, Ramaprabhu *et al.* [91] synthesized CNTs using the catalytic chemical vapor deposition of methane over Mn based alloys hydride catalyst. As-prepared CNTs were purified by the acid-treatment method using concentrated nitric acid. They used the high-pressure sieverts apparatus to study the hydrogen storage in the SWCNTs. The FT-IR spectra of acid treated SWCNTs revealed a broad absorption band at nearly 3452 cm^{-1}, attributed by the hydroxyl group (OH^-). The hydrogen adsorption isotherm of Pt dispersed SWCNT, along with as-grown and purified SWCNT at 25 ^oC and -148 ^oC were studied. The results showed that hydrogen adsorption ability of the purified CNTs was greatly improved compared to the as-grown counterpart in both Pt dispersed and non-dispersed SWCNTs. There was a remarkable increase in the surface area exposed to hydrogen in the purified sample, as amorphous carbon attached to the surface of SWCNT, were removed and open the ends of the SWCNTs. It was also found that Pt dispersed SWCNTs shows a hydrogen uptake up to 3.03wt% at 125 K and 78 bar. It was suggested that it was due to the catalytic activity of the Pt particles which assisted in the dissociation of hydrogen molecules to hydrogen atoms, thereby allowing atomic hydrogen to adsorb chemically at the defective sites of the CNTs [92].

2.12.1.2 Lithium intercalation

The basic principle of rechargeable lithium batteries is the electrochemical intercalation and de-intercalation of lithium in both electrodes. An ideal battery has a high-energy capacity, fast charging time and long cycle life. For lithium, this is the highest in CNTs if all the interstitial sites (inter-shell Van der Waals spaces, inter-tube channels and inner cores) are accessible for Li intercalation [93]. CNTs have shown to possess both highly reversible and irreversible capacities for lithium.

2.12.1.3 Electrochemical supercapacitors

Supercapacitors have a high capacitance and potentially applicable in electronic devices. Typically, they are comprised of two electrodes separated by insulating materials that is ionically conducting in electrochemical devices. This separation is about nanometers for nanotubes in electrodes, very large capacities results from the high nanotubes surface area accessible to the electrolyte [94]

2.12.2 The solvents and salts appropriate for an electrolytic solutions

The salts used in electrochemical experiments must fully dissociate in the solvent in order to generate a conducting (i.e. ionic) solution. The electrolyte solution must be able to dissolve the analyte, must be electrochemically inert over a wide potential range (i.e. no current due to electrolyte solution oxidation/reduction), and must be pure (e.g. the presence of water decreases the size of the potential range). It must also be chemically inert, so that it will not react with any reactive species generated in the experiment. If the temperature is to be varied, the electrolyte solution must have an appropriate liquid range [95].

2.12.3 Ion transport processes

Three processes are involved in the movement of charge or ions in an electrochemical cell.

2.12.3.1 Diffusion

This is spontaneous phenomenon taking place in the presence of a concentration gradient. The fact appears during the process because the discharging species has practically zero concentration near to the microelectrode‘s surface and a spontaneous ion stream originates from the remaining part of the solution in order to compensate for the concentration gradient [96].

2.12.3.2 Migration

This is the motion produced by attraction due to the electrical field generated at the drop surface and acting on the ions of opposite charge present inside the solution [96].

2.12.3.3 Convection

Natural movement of substances, arising from density or temperature gradient inside a solution [96].

2.12.4 Cyclic voltammetry (CV)

Cyclic voltammetry is the most used electrochemical technique and is used to study the electrochemical reactions and provide information about the kinetics of reactions [97]. It is also used to test the properties of the electrodes or solutions. Cyclic voltammetry uses a potentiostat to apply a linearly ramped potential to the working electrode versus the standard reference electrode (Ag/AgCl in this case). To avoid redox reactions at the reference electrode, the reference electrode must have very high impedance. This is accomplished by an amp buffer circuit, which takes the reference electrode potential as an input and supply the necessary current via a counter electrode connected to the op-amp output. The potential provides a cyclic ramp voltage and monitors the working electrode current. In an electrolytic solution, there are positive and negative ions evenly dispersed throughout. When a voltage is applied between the two electrodes, ions respond to the potential by diffusing to the electrodes. These charges surround the oppositely charged electrode in a diffuse layer so that little of the potential penetrate the bulk of the electrolyte outside of the diffuse layer. This layer of charge around an electrode is called the Debye layer. As this potential is increased, more ions are pulled to the surface of the electrode and if the potential at the electrode exceeds that at which redox reaction can occur, electrons are transferred. This transfer constitutes the current through the working electrode. The peak current in CV experiment is given by the following equation:

$$I_p = 2.69 * 105\ n^{3/2}\ ACD^{1/2}\ V^{1/2}, \qquad \textbf{(Eq. 2.2)}$$

where: n = number of electrons transferred/molecule

A = electrode surface area (cm^2)

C = concentration (mol cm^{-3})

D = diffusion coefficient ($cm^2\ s^{-1}$)

Cyclic voltammetric profiles could be reversible, irreversible and quasi-reversible.

Reversible process

The process that obeys the Nernst equation in which the electron transfer is rapid, resulting in both oxidized and reduced species in an equilibrium state [98]

Irreversible process

Only reduction or oxidation peak can be observed in this process due to slow electron transfer at the electrode surface in contrast with the Nernst equation since no equilibrium is maintained [98].

Quasi-reversible process

The intermediate electron transfer process between the reversible and the irreversible reactions. The current is controlled by mass transport and charge transfer kinetics. This process occurs relative to rate of electron transfer with respect to that of mass transport to maintain Nernst equilibrium at the electrode surface [99].

2.12.5 Linear square voltammetry (LSV)

Linear square voltammetry (LSV) is the simplest technique in which the potential range is scanned starting at the initial potential and ending at the final potential. Information about the cathodic or anodic peaks can clearly be obtained by the use of LSV at a low scan rate [100].

2.12.6 Chronopotentiometry (CP)

This technique uses a galvanostat to apply current between the auxiliary and working electrode. The potential of the working electrode (with respect to the reference electrode) is monitored. The basis of controlled current experiments is

that a redox (electron transfer) reaction must occur at the surface of the working electrode in order to support the applied current. Common applications of the galvanostat include constant current stripping potentiometry and constant current electrolysis [101]. One advantage of all constant current techniques is that the ohmic drop due to the solution resistance is also constant, as it is equal to the product of the current and the solution resistance. The ohmic distortion can therefore be simply corrected by a constant potential offset. In contrast, in potentiostatic experiments, the current, and hence the ohmic drop varies with potential, and the correction is more complicated. Chronopotentiometry is the most basic constant current experiment in which a current step is applied across an electrochemical cell without stirring [101].

2.12.7 Controlled potential electrolysis (CPE)

The principle behind the controlled potential electrolysis experiment is simple. If only oxidized species are initially present, then the potential is set at a constant value sufficiently negative to cause a rapid reduction and is maintained at this value until only the reduced species is present in the solution [102]. The total charge passed during the CPE experiment (Q) is calculated by integrating the current and is related to the number of electrons transferred per molecule (n) and the number of moles of the oxidized species initially present (N) through faraday's law:

$$Q = nFN, \qquad \textbf{(Eq. 2.3)}$$

where F is the Faraday's constant (96500 C mol^{-1}).

2.13 Bare electrodes commonly used in electrochemistry

The working electrodes most commonly used in electrochemical laboratories are glassy carbon and pyrolytic graphite [103]. These electrodes have numerous advantages such as low cost, chemical inertness and large potential window as compared to precious metals such as gold electrodes.

2.13.1 Glassy carbon electrode

It is an amorphous form of carbon which is mechanically more durable than the pyrolytic graphite [103].

2.13.2 Pyrolytic graphite electrode

It has a more ordered structure with distinct planes, the basal plane and the edge plane. The edge plane is considerably more conducting than the basal plane [103].

2.14 General methods of bare electrode modification

2.14.1 Drop-dry coating

A few drops of the modifier solution are applied onto the electrode surface and left to stand to allow the solvent to dry out [104].

2.14.2 Electrodeposition

In this method, the electrode is immersed in a concentrated solution (mg/ml) of the modifier followed by repetitive voltammetric scans. Subsequent scans decrease the peak current, followed by the cleaning process which is seen by an increase in peak current [105].

2.14.3 Electropolymerization

In this method, the electrode is immersed in a polymer, modifier or catalyst solution and layers of the electropolymerized material builds on the electrode surface. Generally, the peak current increases with each voltammetric scan [105].

2.14.4 Composite

The electrode is prepared by a simple impregnation of the bulk electrode material with a chemical modifier such as metal nanoparticles [106].

2.15 References

[1] M.S. Dresselhaus, G. Dresselhaus and P.C. Eklund, Carbon, 23 (1996) 123-125.

[2] P.M. Ajayan and T.W. Ebbesen, Reports on Progressing Physics, 60 (2003) 1025-1065.

[3] T. Guo, P. Nikolaev, A. Thess, D.T. Colbert and R.E. Smalley, Chemical Physics Letters, 243 (1995) 1-2.

[4] W.K. Maser, E. Munoz, A.M. Benito, M.T. Martinez, G.F. de la Fuente, Y. Maniette, E. Anglaret and J.L. Sauvajol, Chemical Physics Letters, 292 (1998) 4-6.

[5] A.P. Bolshakov, S.A. Uglov, A.V. Saveliev, V.I. Konov, A.A. Gorbunov, W. Pompe and A. Graff, Diamond and Related Materials, 11 (2002) 3-6.

[6] C.D. Scott, S. Arepalli, P. Nikolaev and R.E. Smalley, Applied Physics A: Materials Science & Processing, 72 (2001) 5-7.

[7] T.W. Ebbesen and P.M. Ajayan, Nature, 358 (1992) 220-222,

[8] H.J. Huang, J. Maria, H. Kajiura and M. Ata, Nanotechnology Letters, 2 (2002) 1117-1119,

[9] Z.F. Ren, Z.P. Huang, D.Z. Wang, J.G. Wen, J.W. Xu, J.H. Wang, L.E. Calvet, J. Chen, J. Klemic and M.A. Reed, Applied Physics Letters, 75 (1999) 8-9.

[10] C.J. Lee, T.J. Lee and C.Y. Park, Carbon, 43 (2005) 1341-1346.

[11] C. Journet and P. Bernier, Applied Physics A-Materials Science & Processing, 67 (1998)

1-9.

[12] A. Yasuda, N. Kawase and W. Mizutani, Journal of Physical Chemistry B, 106 (2002) 51-56.

[13] J.C. Vickerman, Surface Analysis: The Principal Techniques, 1st edn. John Wiley & Sons, Chichester, 67 (1997) 768-769.

[14] H. Goto, T. Furuta, Y. Fujiwara and T. Ohashi, Journal of Material Science, 6 (2003) 200-212.

[15] E. Borowiak-Palen, T. Pichler, X. Liu, M. Knupfer, A. Graff, O. Jost, W. Pompe, R. Kalenczuk, and J. Fink, Chemical Physics Letters, 363 (2002) 567-572.

[16] Z. Bin, C. Robert and H. Hui, Journal of Physical Chemistry, B, 107 (2003) 13838-13842.

[17] M. Huang, A. Yamada, H. Kajiura and M. Ata, Chemical Physics Letters 117 (1995) 2001-2002.

[18] S. Bandow, K.A. Williams, A. Thess, R.E. Smalley and P.C. Eklund, Journal of Physical Chemistry B, 101 (1997) 44-46.

[19] S. Bandow, A.M. Rao, K.A. Williams, A. Thess, R.E. Smalley and P.C. Eklund, Journal of Physical Chemistry B, 101 (1997) 44-47.

[20] E. Farkas, M.E. Anderson, Z.H. Chen and A.G. Rinzler, Chemical Physics Letters, 363 (2002) 111-116.

[21] S. Niyogi, H. Hu, M.A. Hamon, P. Bhowmik, B. Zhao, S.M. Rozenzhak, J. Chen, M.E. Itkis, M.S. Meier and R.C. Haddon, Journal of the American Chemical Society, 123 **(**2001) 733-734.

[22] B. Zhao, H. Hu, S. Niyogi, M.E. Itkis, M.A. Hamon, P. Bhowmik, M.S. Meier and R. Haddon, Journal of the American Chemical Society, 123 (2001) 11673-11677

[23] I.W. Chiang, B.E. Brinson, A.Y. Huang, P.A. Willis, M.J. Bronikowski, J.L. Margrave, R.E. Smalley and R.H. Hauge, Journal of Physical Chemistry B, 105 (2001) 8297-8301.

[24] V. Georgakilas, D. Voulgaris, E. Vazquez, M. Prato, D.M. Guldi, A. Kukovecz and H. Kuzmany, Journal of the American Chemical Society, 124 (2002) 48-49

[25] H. Kajiura, S. Tsutsui, H.J. Huang and Y. Murakami, Chemical Physics Letters, 364 (2002) 586-592.

[26] P. Avouris, Chemical Physics, 281 (2002) 429-445.

[27] M. Damnjanovic, I. Milosevic, T. Vukovic and R. Sredanovic, Physical Review B, 60 (1999) 2728-2739.

[28] S. Niyogi, M.A. Hamon, H. Hu, B. Zhao, P. Bhowmik, R. Sen, M.E. Itkis and R.C. Haddon, Accounts of Chemical Research, 35 (2002) 12-14.

[29] N. Toshima, L.M. Marzan and P.V. Kamat, Nanoscale Materials, 11 (2003) 79-96.

[30] A.S. Edelstein and R.C. Cammarata, Nanomaterials, 31 (1996) 461-466.

[31] U. Kreibig and M. Vollmer, Optical Properties of Metal Clusters, Springer, 16 (1995) 342-344.

[32] A. Hilger, N. Guppers and U. kreibig, European Journal of Physics, 10 (2000) 115-118.

[33] C. Burda, X. Chen and R. Narayana, Chemical Review, 105 (2005) 1025-1102.

[34] P. Sen, J. Ghosh and P. Kumar, Indian Academy of Science, 115 (2003) 499-508.

[35] G. Schmid and C.N.R. Rao, Journal of Material Chemistry, 1 (1999) 1-14.

[36] D.V. Goia and E. Matijevic, New Journal of Chemistry, 119 (1998) 1203-1215.

[37] A. Henglein, Chemical Review, 89 (1989) 1861-1873.

[38] W.J. Zhang, Nanoparticles Reports, 5 (2003) 323-326.

[39] C. Wang and W. Zhang, Environmental Science Technology, 31 (1997) 2154-2157.

[40] Z. Wei-Xian, S. Yuang-Pang and L. Xiao-Qin, Advances in Colloid and Interface Science, 120 (2006) 47-56.

[41] B. Mozghan and D. Sally, Journal of Chemical Education, 84 (2007) 322-324.

[42] Z.I. Kudryavtseva and A.G. Pshenicknikov, Russian Journal of Electrochemistry, 40 (2004) 1208-1213.

[43] Y. Hsieh, H. Chien-Te and C. Yun-Wen, International Journal of Hydrogen energy, 32 (2007) 3457-3464.

[44] J.E.B. Randles, Transcript Faraday Society, 44 (1948) 327-328.

[45] Z.I. Wang, Structural Evolution and Structure Analysis, 13 (1998) 113-116.

[46] C. Hu, H. Liu and Z.L. Wang Synthesis of Oxide Nanostructures, 14 (2008) 30332-30334.

[47] D. Jong and P. Xiao, Journal of Physical Chemistry, 117 (2005) 134-137.

[48] A. Zuttel, Materials Today, 9 (2003) 24-33.

[49] W. Grochala and P.P. Edwards, Chemical Review, 104 (2004) 1283-1316.

[50] N.M. Rodriquez, C. Parks, R.T.K. Baker and A. Chambers, Journal of Physical Chemistry, 102 (1998) 4253-4256.

[51] C. Liu, Y.Y. Fan, M. Liu and M.S. Dresselhaus, Science, 286 (1996) 1127-1129.

[52] Y. Lu, H. Fan, A. Stump, T.L. Ward, T. Rieker and C.J. Brinker, Nature, 398 (1999) 223-226.

[53] J. Zhu, M. Yudasaka, M. Zhang, D. Kasuya and S. Iijima, Nanotechnology Letters, 3 (2003) 1239-1243.

[54 E. Leontidis, M. Orphanou, T. Kyprianidou-Leodidu, F. Krumeich and W. Caseri, Nanotechnology Letters, 3 (2003) 569-72.

[55] C.N.R. Rao and G. Gautam, Journal of Material Chemistry, 13 (2003) 209-213.

[56] C.R. Brundle, C.A. Evans and S. Wilson, Butterworth-Heinemann, Stoneham, 32 (1992) 765-768.

[57] C.R. Brundle and C.A. Evans, Wilson S. Butterworth-Heinemann, Stoneham, 431 (1992) 432-435.

[58] J.C. Vickerman, Surface Analysis: The Principal Techniques, 1st edn. John Wiley & Sons, Chichester, 321 (1997) 567-569.

[59] G. Acres, Journal of Power Sources, 100 (2001) 60-66.

[60] R. Agrawal, M. Offut and M.P. Ramage, Journal of Physical Chemistry, 51 (2005) 1582-1589.

[61] G. Marban and T. Valdes-Solis, International Journal of Hydrogen Energy, 32 (2007) 1625-1637.

[62] S. Dunns, International Journal of Hydrogen Energy, 27 (2002) 235-264.

[63] G. Berry, Encyclopedia of Energy, 31 (2004) 253-265.

[64] K. Alanne, A. Saari, V. Ugursal and J. Good, Journal of Power Sources, 158 (2006) 403-416.

[65] E. Antolini, Applied Catalysis B: Environmental, 74 (2007) 337-350.

[66] M. Ni, D. Leung, M. Leung and K. Sumathy, Fuel Process Technology, 87 (2006) 461-472.

[67] R. Harris, D. Book, P. Anderson and P. Edwards, The fuel Cell Review, 1 (2004) 17-23.

[68] P. Edwards, V. Kuznetsov and W. David, Hydrogen Energy, 365 (2007) 1043-1056.

[69] G.D. Berry, Hydrogen production. Encyclopedia of Energy, 67 (2004) 253-265.

[70] L. Barreto, A. Makihira and K. Riahi K, International Journal of Hydrogen Energy Res, 31 (2007) 637-663

[71] A.E. Kaifer and M. Gomez-Kaifer, Supramolecular Electrochemistry, Wiley-VCH, New York, 43 (1999) 342-346.

[72] J. Wang, Analytical Electrochemical, VCH Publishers Incorporation, New York, 45 (1994) 231-234.

[73] C.M. Harris, Analytical Chemistry A, 74 (2002) 126-128.

[74] P.T. Kissinger and W.R. Heineman, Laboratory Techniques in Electroanalytical Chemistry, Marcel Dekker Incorporation, New York, 234 (1996) 23-27.

[75] K.B. Prater and A.J. Bard, Journal of Electrochemistry Society, 117 (1970) 207-208.

[76] V.J. Puglisi and A.J. Bard, Journal of Electrochemistry Society, 119 (1972) 833-836.

[77] A.J. Bard and L.R. Faulkner, Electrochemical Methods: Fundamentals and Applications, 2nd ed., John Wiley and Sons, 45 (2001) 567-569

[78] F.M. Hawkridge, P.T. Kissinger and W.R. Heineman, Laboratory Techniques in Electroanalytical Chemistry 2nd ed., Marcel Dekker Incorporation, New York, 56 (1996) 786-789.

[79] P.M. Ajayan and O.Z. Zhou, Carbon Nanotubes, 80 (2001) 391-425.

[80] S. Niyogi, H. Hu, M.A. Hamon, P. Bhowmik, B. Zhao, S.M. Rozenzhak, J. Chen, M.E. Itkis, M.S. Meier and R.C. Haddon, Journal of the American Chemical Society, 123, (2001) 733-734.

[81] B. Zhao, H. Hu, S. Niyogi, M.E. Itkis, M.A. Hamon, P. Bhowmik, M.S. Meier and R.C. Haddon, Journal of the American Chemical Society, 123, (47), (2001) 11673-11677.

[82] D. Vinden and R. Maxi, Carbon, 43 (1984) 343-346.

[83] L. Seung Mi, P. Ki Soo and B. Jin Moon, Synthetic Metals, 113 (2000) 209-216.

[84] P. Peng, W. Wang and R. Chung, Carbon, 39 (2001) 2077-2079.

[85] Z.F. Ren and J.H. Chen, Journal of Physical Chemistry, 63 (2004) 347-348.

[86] H. Chien-Te and C. Yun-Wen, International Journal of Hydrogen Energy, 32 (2007) 3457-3464.

[87] S. Ramaprabhu and A. Reddy, International Journal of Hydrogen Energy, 33 (2008) 1028-1034.

[88] R.H. Baughman, A.A. Zakhidov and W.A. de Heer, Science, 297 (2002) 787-792.

[89] E.W. Hooijschuur, A. HuIst, A. de Long, L. de Reuver, S. van Krimpen, B. van Baar, E. Wils, C. Kientz and U.A. Brinkman, Trends in Analytical Chemistry, 21 (2001) 116-118.

[90] Y. Yang, Chemistry Res, 32 (1999) 109-112.

[91] P.A. Christenson and A. Hamnet, Techniques and Mechanisms in Electrochemistry, 1st ed, Blackie Academic and Professional, London, 47 (1994) 768-769.

[92] E.R. Brown, R.F. Large, A. Weissberger and B. Rossiter. Electrochemical Methods Vol.1-Part IIA, Wiley-Interscience, New York, 213 (1971) 765-768.

[93] R.S. Niccholson, Analytical Chemistry, 37 (1965) 1351-1353.

[94] M.H. Pournaghi-Azar and R.J. Sabzi, Electroanalytical Chemistry, 543 (2003) 115-116.

[95] P. Santhosh, K.M. Manesh, P.K. Lee and A.I. Gopalan, Electroanalysis, 18 (2006) 894.

[96] P. Santhosh, K.M. Manesh, P.K. Lee and A.I. Gopalan, Electroanalysis, 18 (2006) 1564.

[97] C.E. Banks and R.G. Compton, Analyst, 131 (2006) 15-16.

[98] N.S. Lawrence, R.P. Deo and J. Wang, Analytical Chimica Acta, 517 (2004) 131-132.

[99] A. Salimi, R. Hallaj and G.R. Khayatian, Electroanalysis, 17 (2005) 873-874.

[100] A.W. Snow, W.R. Barge, A.P.B. Lever and R.T. Leznoff, Pthalocyanines: Properties and Applications Vol 1, VCH Publishers, New York, 324 (1989) 657-658.

[101] M. Musameh, J. Wang and Y. Lin, Electrochemistry Communications, 4 (2002) 743-745.

[102] N. Diab, J. Oni and W. Schuhmann, Bioelectrochemistry, 66 (2005) 105-107.

[103] C. Sivakumar, J.N. Nian and H. Teng, Journal of Power Sources, 144 (2005) 295-297.

[104] E. Mun oz, M.A. Heras, A.I. Colina, V. Ruiz and J. Lopez-Palacios, Electrochimica Acta, 52 (2007) 4778-4779.

[105] Z. Chen and Y. Zhou , Surface and Coating Technology, 201 (2006) 2416-2419.

[106] R. de Levie, Electrochimica Acta, 125 (2003) 14893-14900.

CHAPTER 3

Experimental Methods

3.1 Introduction

The electrocatalytic activity involving carbon nanotubes, metal nanoparticles and metal oxides as supports and catalysts for hydrogen storage largely depends on the active surface area, which is generally a direct function of the degree of metal nanoparticles and metal oxides dispersion. The electrocatalytic activity of the carbon nanotubes is greatly improved when they are finely distributed by metal nanoparticles and metal oxides catalyst. Due to continuing interest in carbon nanotubes activation, a considerable variety of activation procedure for electrochemical application has been developed, such as fine dispersions on metal nanoparticles and metal oxides catalysts, reduction of metal salts in solution or on a solid support interface.

For a conclusive elucidation of the morphology of nanocomposites, which is a prerequisite for understanding the relationship between morphology and electrocatalytic activity, x-ray diffraction scanning electron microscopy and transmission electron microscopy was employed to provide structural information on the atomic scale. The successful incorporation of the functional groups on the surface of the carbon nanotubes can be proved by the use of Fourier-transform infrared spectroscopy.

In electrochemistry, various methods are been employed to modify the glassy carbon electrode with carbon nanotubes, metal nanoparticles and metal oxides. Such methods involve drop-drying, electropolymerisation and electrodeposition. The degree of nanocomposites dispersion on the active surface area of the

glassy carbon electrode is critical in electrochemical applications such as hydrogen storage.

3.2 Reagents and chemicals

All chemicals were generally reagent grade and were used as received except where otherwise mentioned. The water used for all preparations in this dissertation was double-distilled water. Multi-walled carbon nanotubes used in this dissertation was prepared from iron (II) phthalocyanine precursor purchased from Aldrich (90% dye). Synthesized multi-walled carbon nanotubes were purified by refluxing with a mixture of HNO_3 (55% assay) from uniLAB and H_2SO_4 (95-97% assay) from Fluka [1].

The nitrate salt used to prepare iron nanoparticles (Fe) and iron (III) oxide (Fe_2O_3) was iron (III) nitrate nonahydrate ($Fe(NO_3)_3*9H_2O$, 98% assay) from Sigma-Aldrich.

Copper nanoparticles (Cu) and copper (II) oxides (CuO) used were prepared from the copper (II) nitrate pentahemihydrate solution ($Cu(NO_3)_2*2.5H_2O$, 98% assay), from Sigma-Aldrich by reduction method using sodium borohydride (Aldrich) as the reducing agent.

The nickel source used was nickel (II) nitrate hexahydrate ($Ni(NO_3)_2*6H_2O$, 97.0% assay) from Fluka analytical.

Nanocomposites materials were prepared by mixing known amount of metal nanoparticles or metal oxides with a known amount of MWCNTs using the N, N-Dimethylformamide (abbreviated DMF, 99.5% assay) from Saarchem as the binder.

3.3 Synthesis of carbon nanotubes, metal nanoparticles and metal oxides

3.3.1 Preparation of carbon nanotubes

Multi-walled carbon nanotubes were prepared by pyrolysis of 0.31 g of iron (II) phthalocyanine ($C_{32}H_{16}FeN_8$, figure 3.1) which was placed in a boat in the middle of the quartz glass tube. Prior and during pyrolysis, a controlled flow of Ar/H_2 (3:1 v/v, 40 ml/min) mixture was introduced into the quartz tube. Sample was heated by Lenton furnaces with independent temperature controllers. The middle furnace was adjusted to a pyrolysis temperature of 900 ^oC. The temperature ramping rate recorded ranged between 20 to 21 ^oC/min. After the furnace has reached 900 ^oC, the furnace was kept at this temperature for an additional 30 min (pyrolysis time) for deposition of multi-walled carbon nanotubes to be completed. The CNTs formed were scrapped from the boat and quartz tube as a black powder [1].

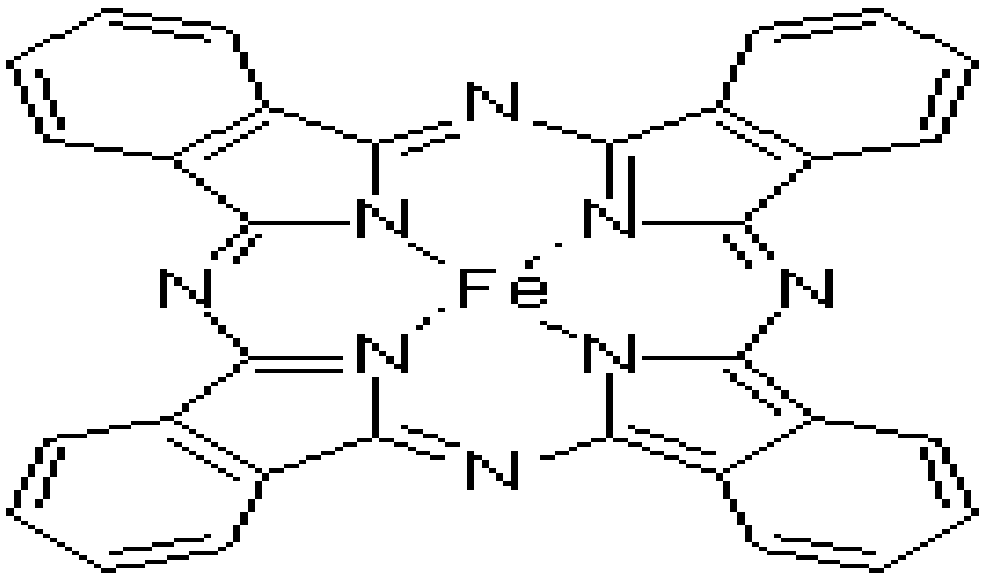

Figure 3.1: Structure of the iron (II) phthalocyanine (FePc) used to prepare MWCNTs [2].

3.3.1.1 Purification of carbon nanotubes

The as-prepared multi-walled carbon nanotubes were purified by refluxing with a mixture of HNO_3 and H_2SO_4 using a 1:3 ratio at 80 ^oC for 30 min. Thereafter, the mixture was diluted with water and filtered while washing with distilled water (about 900 ml). Washed multi-walled carbon nanotubes were dried at 80 ^oC for 4 hrs [3].

3.3.2 Preparation of metal nanoparticles

3.3.2.1 Iron nanoparticles

Iron nanoparticles used were prepared by employing the reduction method using sodium borohydride as the reducing agent. A concentration of 0.1 M $Fe(NO_3)_3*9H_2O$ solution was prepared and a 0.2 M solution of sodium borohydride ($NaBH_4$) was added drop-wise while stirring the mixture at a rate of 100 rpm. After a drop-wise addition of sodium borohydride, the metal nitrate solution was allowed to stir for an additional 30 min to allow for a complete formation of metal nanoparticles. It is worth mentioning that it was of interest to synthesize nanoparticles with a desired optical, magnetic, electrical, surface area and catalytic properties for successful application in gas storages, sensors and high performance nanoscale device. The solutions were prepared using de-ionized water [4, 5].

3.3.2.2 Copper nanoparticles

Copper nanoparticles (Cu) were also prepared from the copper (II) nitrate pentahemihydrate solution ($Cu(NO_3)_2*2.5H_2O$, 98% assay, from Sigma-Aldrich) by reduction method using sodium borohydride as the reducing agent in a 1:1 v/v. The reducing agent was added drop-wise into the aqueous copper source [4, 5]. The rate of the drop was controlled to give a required size and shape of the copper nanoparticles formed. During the process, Cu^{2+} gains electrons and became reduced to electron rich Cu^0. After formation of the nanoparticles, they were filtered and washed with 900 ml of distilled water and thereafter dried at 80 ^oC for 4 hrs. The chemical reaction involves the sodium borohydride reduction of metal nitrate as follows:

$$Cu(NO_3)_2 + 2NaBH_4 \longrightarrow Cu + H_2 + B_2H_6 + 2NaNO_3 \qquad \textbf{(Scheme 3.1)}$$

3.3.2.3 Nickel nanoparticles

Nickel nanoparticles (Ni) were prepared using similar procedure as that of copper nanoparticles and iron nanoparticles reported earlier. The nickel source used was nickel (II) nitrate hexahydrate ($Ni(NO_3)_2*6H_2O$, 97% assay from Fluka analytical).

The chemical reaction involves the sodium borohydride reduction of metal nitrate:

$$Ni(NO_3)_2 + 2NaBH_4 \longrightarrow Ni + H_2 + B_2H_6 + 2NaNO_3 \qquad \textbf{(Scheme 3.2)}$$

It is evident that hydrogen and diborane gasses are possibly to be formed during the reduction reaction. The above chemical equations implies that it requires two (2) moles of $NaBH_4$ to reduce one (1) mole of Cu or Ni nitrate solution to its neutral oxidation state i.e.

$Ni^{2+}/Cu^{2+} + NaBH_4 \longrightarrow Ni^{+}/Cu^{+} + NaBH_4 \longrightarrow Ni^{0}/Cu^{0}$ **(Scheme 3.3)**

Afterwards, the solution was filtered using a 0.45 µm filter paper and washed with 900 ml distilled water to remove the nitrate salts. The remaining metal (Cu, Fe and Ni) nanoparticles were dried in air at 80 ^{o}C for 3 min. Some Ni nanoparticles were calcined in air at 400 ^{o}C for 2 hrs to study the effect of calcination [4, 5].

3.3.3 Preparation of metal oxides

3.3.3.1 Copper (II) oxides

Copper (II) oxide (CuO) was prepared from copper (II) nitrate pentahemihydrate (98%, Sigma-Aldrich) by heating in air at 400 ^{o}C for 2 hrs. High temperature treatment results in decomposition of nitrate from the complex. There are three ways in which the copper metal can form a bond with the oxides group, i.e. CuO, Cu_2O and Cu_3O_2. Depending on the preparation method employed [6]. The typical chemical oxidation reactions for preparation of metal oxides are as follows:

$$Cu(NO_3)_2 \xrightarrow{400\ ^{o}C,\ 2h} Cu^{2+} + 2NO_3$$ **(Scheme 3.4)**

3.3.3.2 Nickel (II) oxides

Nickel (II) oxides (NiO) were prepared by employing the same method as for copper oxides mentioned above. This heat treatment method oxidizes the metals by decomposing the nitrate group (NO_3) from the metal source with water

molecules evaporating [6]. The typical chemical oxidation reactions for preparation of metal oxides are as follows:

$$Ni(NO_3)_2 \xrightarrow{400\ ^oC,\ 2h} Ni^{2+} + 2NO_3 \qquad \textbf{(Scheme 3.5)}$$

3.3.3.3 Iron (III) oxides

Iron (III) oxides (Fe_2O_3) used were also prepared in the same manner as the copper oxides and nickel oxides reported above [6]. The typical chemical oxidation reactions for preparation of metal oxides are as follows:

$$Fe(NO_3)_3 \xrightarrow{400\ ^oC,\ 2h} Fe^{3+} + 3NO_3 \qquad \textbf{(Scheme 3.6)}$$

3.4 Decoration of MWCNTs by metal nanoparticles and metal oxides

Approximately 2 mg of metal nanoparticles or metal oxides were mixed with approximately 2 mg of MWCNTs and 2 ml of N, N-Dimethylformamide (DMF, 99.5% assay, Saarchem) as the binder. The nanocomposites was stirred or sonicated to allow the mixture to dissolve which subsequently resulted in metal nanoparticles or metal oxides being well coated on the surface of the oxidized MWCNTs. The known volume of the putty form of the MWCNT-M (M = metal nanoparticles or metal oxides) nanocomposites was drop-dried on the glassy carbon bare electrode at 80 ^oC for 1 min [7].

3.5 Characterization

3.5.1 Transmission electron microscopy (TEM) analysis

A JEOL 2100 transmission electron microscopy (TEM) with a 200 kV acceleration voltage and LaB6 filament was used in bright field mode to determine the micro-structure of the carbon nanotubes and nickel nanoparticles decorated carbon nanotubes. The microscope has a point resolution of 0.2 nm and is equipped with a Gatan US1000, 2048 x 2048 pixel CCD camera.

Carbon nanotubes and nickel metal nanoparticles were prepared for TEM analysis by adding small quantities of powder to about 5 ml of methanol and facilitating the dispersion of the particles/structures with a sonicator for 5 seconds. A glass pipette was used to collect small amounts of this colloidal liquid from the centre of the dispersant volume. One drop of the solution was released onto the centre of an Agar Scientific 300 µm holey carbon film coated copper grid located on filter paper. The deposited solution was allowed to dry in air.

3.5.2 Scanning electron microscopy (SEM) analysis

Scanning electron microscopy was used to determine the powder morphology and microstructure of the nanomaterial samples. Metal nanoparticles (Fe, Cu and Ni), metal oxides (Fe_2O_3, CuO and NiO), metal nanoparticles decorated multi-walled carbon nanotubes (MWCNT-Fe, MWCNT-Cu and MWCNT-Ni) and metal oxides decorated multi-walled carbon nanotubes (MWCNTs-Fe_2O_3, MWCNTs-CuO and MWCNTs-NiO), were all examined by SEM to investigate their powder morphology.

3.5.3 X-ray diffraction (XRD) spectroscopy analysis

X'pert Pro X-ray spectroscopy instrument from PAN analytical was used to determine the structure of the as-prepared multi-walled carbon nanotubes. The following XRD experimental analysis method was employed: Wavelength of Cu K alpha radiation used was 1.5406 Å with 2 theta = 5 - 100 deg and exposure time of 15 min/s. The Step size was 0.026 deg and the Time / Step was 61.2 s at a scan speed of 0.109 deg/s. The X-ray spectroscopy measurement provided not only structural characterization of MWCNTs but also information about the presence or the catalytic particles in the unpurified sample [8].

3.5.4 Fourier transform-infrared (FT-IR) spectroscopy analysis

FT-IR spectroscopy was used to identify the functional groups present on the surface of the as-prepared and acid treated MWCNTs. FT-IR instrument used was Perkin Elmer spectrum 100 on ATR mode with Resolution of 4 cm^{-1} and 4 scan numbers at a room temperature of 21 ^{o}C. FTIR spectrum of as-prepared CNTs and acid treated CNTs were obtained.

3.6 Electrochemical application at the glassy carbon electrode for hydrogen storage

Cyclic voltammetry (Bioanalytical technique from Basi-Epsilon) with three electrode system as shown in figure 3.2 was used to investigate the electrochemical properties of multi-walled carbon nanotubes for hydrogen storage. The modified GCE was used as the working electrode with the platinum wire and silver/silver chloride as the counter and reference electrode respectively. A 6 M KOH (98% assay, Merck) aqueous solution was used as the

electrolyte for all experimental analysis unless otherwise stated. Prior to the running of experiments, the electrolyte was flushed with N_2 gas to remove the dissolved oxygen and impurities responsible for electron loss. Cyclic voltammetry (CV), chronopotentiometry (CP) and controlled potential electrolysis (CPE) techniques were used to investigate the current responds, charge-discharge voltages and the discharge capacities of glassy carbon modified electrode respectively [9, 10]. In each CV experiment, the potential was scanned from -200 mV to -1200 mV at a known scan rate.

For all electrochemical analysis in this dissertation, the drop-drying method was employed for the modification of the glassy carbon electrode (3 mm in diameter). The known quantity of modifiers were dropped on the active surface area of the GCE and dried in an oven for 1 minute under air atmosphere at a known temperature [11].

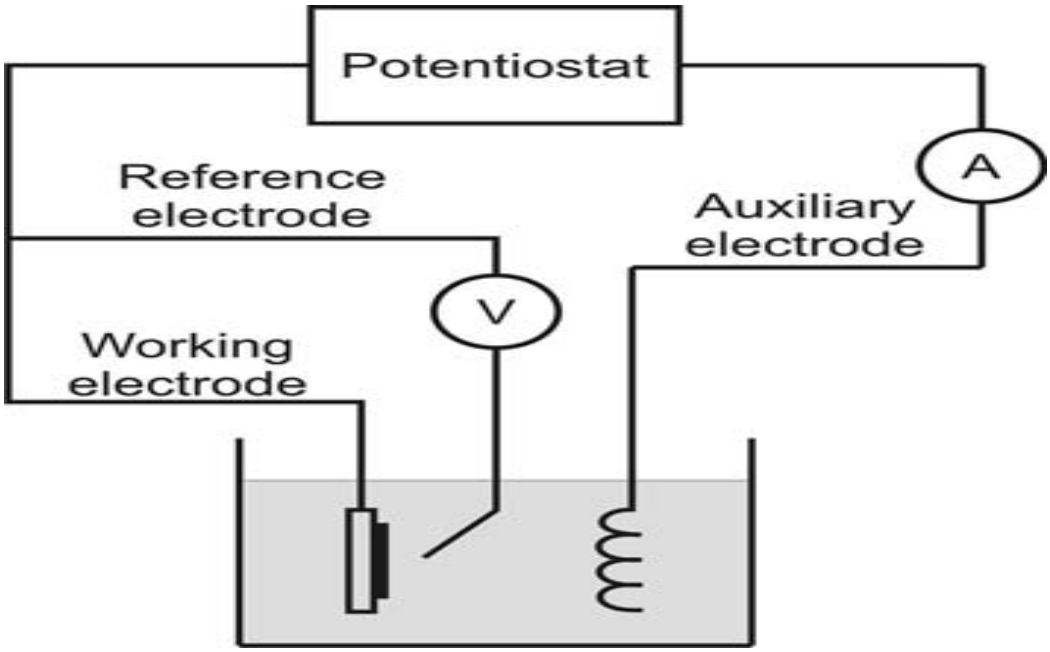

Figure 3.2: Electrochemical cell showing the three-electrode system for the exact control of the electrode potential [12].

After each analysis, the surface of the working electrode was cleaned by light polishing with a 0.05 µm alumina fine polish. A few drops of the polish were placed on a polishing pad (brown texmet for alumina), and the electrode was held vertically and rubbed on the polish in a figure of eight pattern for 30 seconds to a few minutes, depending upon the condition of the electrode surface. After polishing, the electrode surface was rinsed thoroughly with distilled water and allowed to air dry so as to remove any residual alumina particles and obtain a mirror-like surface [13].

Since the potential of a chlorine-containing reference electrode is sensitive to chlorine concentration, the Ag/AgCl electrode used was stored with a frit immersed in a solution of 3 M sodium chloride [14].

3.7 References

[1] D. Liming, H. Showing and M. Albert, Journal of Physical Chemistry B, 103 (1999) 4223-4227.

[2] C.C. Lezneff and A.B.P. Lever, Phthalocyanine Properties and Applications, 1-4 (1996) 1989-1993.

[3] Z. Bin, C. Robert and H. Hui, Journal of Physical Chemistry B, 107 (2003) 13838-13842.

[4] W.J. Zhang, Nanoparticles Res, 5 (2003) 323-326.

[5] C. Wang and W. Zhang, Environmental Science Technology, 31 (1997) 2154-2157.

[6] D. Jong and P. Xiao, Journal of Physical Chemistry, 117 (2005) 134-137.

[7] C.N.R. Rao and G. Gautam, Journal of Material Chemistry, 13 (2003) 209-213.

[8] M.M. Shaijumon, N. Rajalakshmi, H. Ryu and S. Ramaprabhu, Nanotechnology, 16 (2005) 518-519.

[9] J.J.T. Maloy, P.T. Kissinger and W.R. Heineman, Laboratory Techniques in Electroanalytical Chemistry, Marcel Dekker Inc., New York, 234 (1996) 23-27.

[10] K.B. Prater and A.J. Bard, Journal of Electrochemistry Society, 117 (1970) 207-208.

[11] N. Diab, J. Oni and W. Schuhmann, Bioelectrochemistry, 66 (2005) 105-107.

[12] A. Patil, J. Sippel, G.W. Martin and A.G. Rinzler, Nanotechnology Letters, 2 (2004) 303.

[13] V.J. Puglisi and A.J. Bard, Journal of Electrochemistry Society, 119 (1972) 833-836.

[14] F.M. Hawkridge, P.T. Kissinger and W.R. Heineman, Laboratory Techniques in Electroanalytical Chemistry 2nd ed., Marcel Dekker Inc., New York, 56 (1996) 786-789.

CHAPTER 4

Electrochemical activity of metal Oxides (CuO, Fe_2O_3 and NiO) and metal nanoparticles (Cu, Fe and Ni) decorated multi-walled carbon nanotubes (MWCNTs) for hydrogen storage at the glassy carbon electrode (GCE).

4.1 Introduction

Electrochemical activity of metal nanoparticles decorated carbon nanotubes for hydrogen storage was first studied by Nutzenadel *et al*. [1]. Zhang *et al*. [2] recently studied the electrochemical storage of hydrogen at the Cu and Ni decorated MWCNTs. They observe that electrochemical activity of copper was worse than that of nickel, that is to say, Cu-H bond energy is lower than Ni-H. However, copper powder was found to improve the electric conductivity, stability, ability of anti-oxidation and discharge capability. These metal has effect on de-oxidation of electrodes. These strongly suggested that copper powder can make hydrogen diffuse into MWCNTs easily and make MWCNTs fully useful. Thus the hydrogen storage is enhanced [2].

The dissertation objectives were focused mainly on the electrochemical storage of hydrogen on the metal nanoparticles (Cu, Fe and Ni) and metal oxides (CuO, Fe_2O_3 and NiO) decorated MWCNTs. The study hoped to obtain a hybrid or nanocomposite that will give the highest discharge capacity. The study involved the investigation of the role played by purified MWCNTs; Cu, CuO decorated MWCNTs; Fe, Fe_2O_3 decorated MWCNTs; and Ni, and NiO decorated MWCNTs, on the hydrogen storage capacity. The study also focused on the effect of Ni nanoparticles and MWCNTs loadings. Influence of calcining the Ni nanoparticles on the hydrogen storage capacity was also investigated.

4.2 Experimental

4.2.1 Preparation and electrochemical activity of MWCNTs, metal nanoparticles and metal oxides for hydrogen storage

All chemicals were generally reagent grade and used as received except where otherwise stated. Carbon nanotubes, metal nanoparticles and metal oxides have been prepared as described in Chapter 3.

For all electrochemical applications in this dissertation, the direct and fine dispersion method was employed. Almost about 2 mg of the modifier were dissolved in 2 ml DMF (Saarchem, 99.5% assay) which was used as a binder and from that amount, 2 µl was coated on the glassy carbon electrode for reliable comparison unless otherwise stated [3]. This method is explained fully in Chapter 3.

Cyclic voltammetry, chronopotentiometry and controlled potential electrolysis were employed to investigate the current response, charge-discharge voltages and discharge capacities respectively of the glassy carbon modified electrode. In CV studies, the potential was applied externally from -200 mV to -1200 mV using a potentiostat with three-electrode system. Since the potential of the reference electrode is sensitive to the temperature, it is worth mentioning that the temperatures of the 6 M KOH electrolyte used for these experiments were monitored and recorded prior to each electrochemical analysis.

Cyclic voltammetry was scanned three times for consistence and reproducibility of the obtained cyclic voltammogramms. From the CP, the second scan was taken for both charge and discharge voltages. The tenth scan was taken for each CPE analysis for discharge capacity and cycle life studies.

4.2.2 Transmission electron microscope (TEM)

This technique was used to determine the micro-structural information of the as-prepared CNTs, calcined and uncalcine Ni nanoparticles decorated CNTs. Samples for TEM test were prepared as described in Chapter 3. Information at the atomic level was also given [4].

4.2.3 Scanning electron microscopy (SEM)

Scanning electron microscopy was used to determine the powder morphology and microstructure of the nanomaterial samples as mentioned in Chapter 3.

4.2.4 X-ray diffraction (XRD) spectroscopy

X-ray diffraction was used to characterize the crystallinity and phase purity of the as-prepared MWCNTs. The particle or crystalline size can be determined by the use of Scherrer Formula [4]. The method is fully explained in Chapter 3.

4.2.5 Fourier transform-infrared (FT-IR) spectroscopy

The FT-IR was used to identify the functional groups present on the surface of the as-prepared and acid treated MWCNTs. The method is explained fully in Chapter 3.

4.3 Results and Discussions

4.3.1 Transmission electron microscopy (TEM) analysis

The low and high magnification TEM images of the as-prepared MWCNTs produced from pyrolysis of iron (II) pthalocyanine are shown in figure 4.1. Figure 4.1 shows TEM images of as-prepared MWCNTs at a magnification of **(a)** 200 nm, **(b)** 50 nm, **(c)** 20 nm and **(d)** 50 nm. The arrow in figure 4.1 **(a)**, **(c)** and **(d)** shows the tubes of the as-prepared MWCNTs. In figure 4.1 **(a)** and **(b)**, the arrow shows the iron nanoparticles used as catalyst during synthesis. It can be observed from these images that the carbon nanotubes produced are multi-walled. All the CNTs appear as short tubular products. Figure 4.1 **(a)** shows a high magnification TEM image of as-prepared MWCNTs, and it can be seen that most of the compartments were empty while few contained a small iron particles in the middle (figure 4.1 **(b)**) or at the end (figure 4.1 **(c)**) of the nanotubes. The Fe-filled CNTs displayed a dark and uniform contrast with the surrounding CNTs. Figure 4.1 **(a)** also shows stem of the ACNTs, revealing a bamboo-shaped multi-walled structure. From figure 4.1 **(b)**, it is seen that the as-prepared MWCNTs were entangled with amorphous carbon, carbon nanoparticles and Fe catalyst particles. The ACNTs also appeared to be having open tips/caps as shown in figure 4.1 **(a)**.

It is generally accepted that CNTs growth processes involve adsorption and decomposition of gases (or gas phase molecular) containing carbon on metal surfaces, dissolution and diffusion of the released carbon atoms in the catalyst, and precipitation of the graphite-like layers [5].

Liu *et al*. [6] reported that the size of the catalyst Fe nanoparticles continuously increases during the growth of CNTs because Fe clusters originated from FePc continuously supply Fe catalyst nanoparticles, resulting in increased diameter of CNTs during CNTs growth.

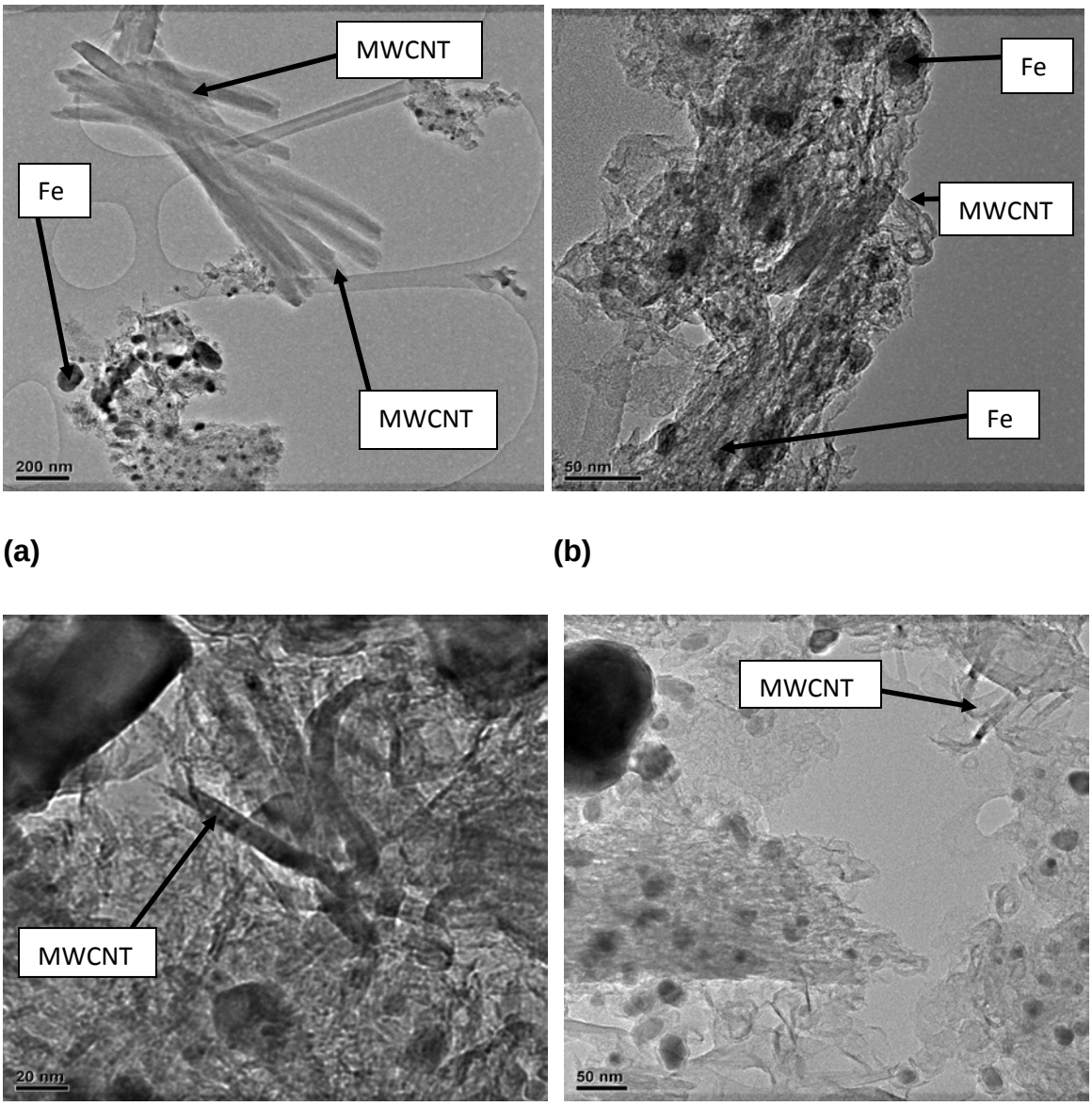

Figure 4.1: TEM images of the as-prepared MWCNTs produced by pyrolysis of iron (II) phthalocyanine at a magnification of **(a)** 200 nm, **(b)** 50 nm, **(c)** 20 nm and **(d)** 50 nm.

TEM images illustrated in figure 4.2 confirm a successful decoration of oxidized MWCNTs with Cu and CuO. Well dispersed images of CuO nanoparticles on the surface of the MWCNTs are clearly shown in figure 4.2 **(b)**.

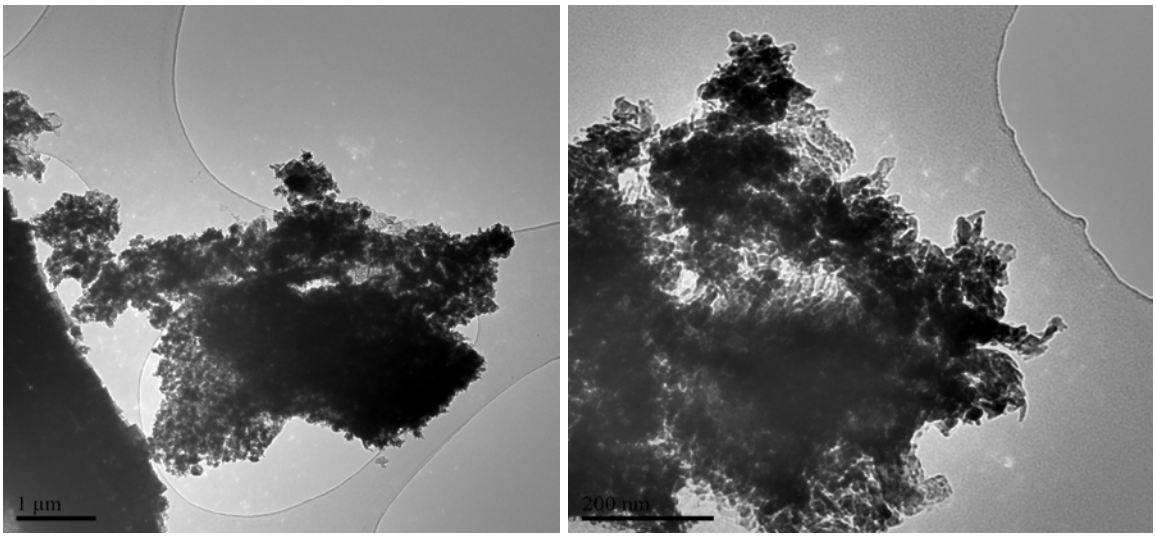

(a)

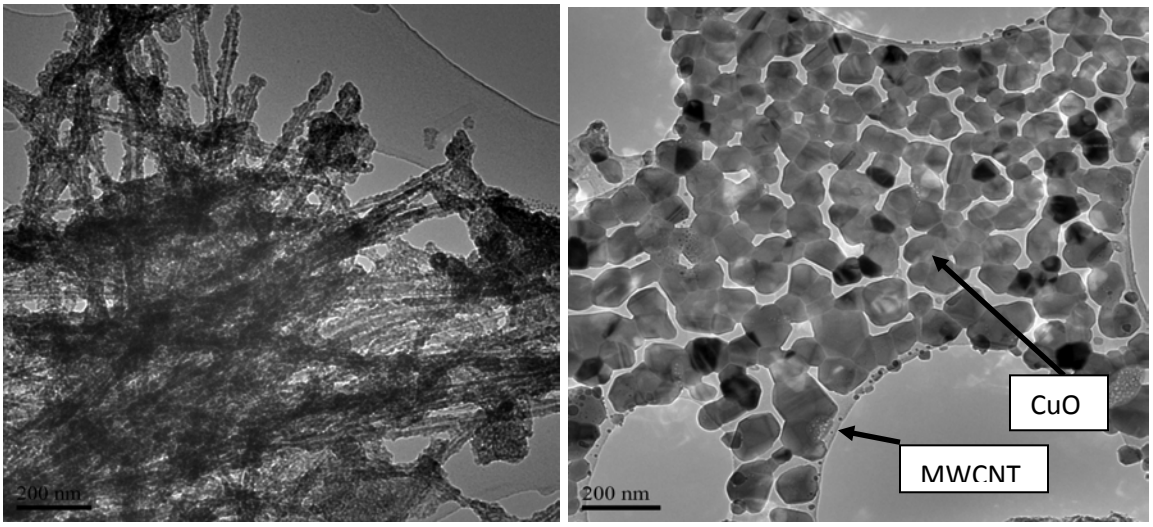

(b)

Figure 4.2: TEM images of **(a)** MWCNT-Cu at a magnification of 1 µm and 200 nm and **(b)** MWCNT-CuO at a magnification of 200 nm.

Transmission electron microscopy images of MWCNT-Fe and MWCNT-Fe_2O_3 are depicted in figure 4.3. Figure 4.3 **(a)** shows MWCNTs coated with Fe nanoparticles. Figure 4.3 **(b)** illustrate a long MWCNTs well coated with Fe_2O_3.

The TEM images in figure 4.3 **(b)** clearly shows several particles of Fe_2O_3 along a strand of MWCNT.

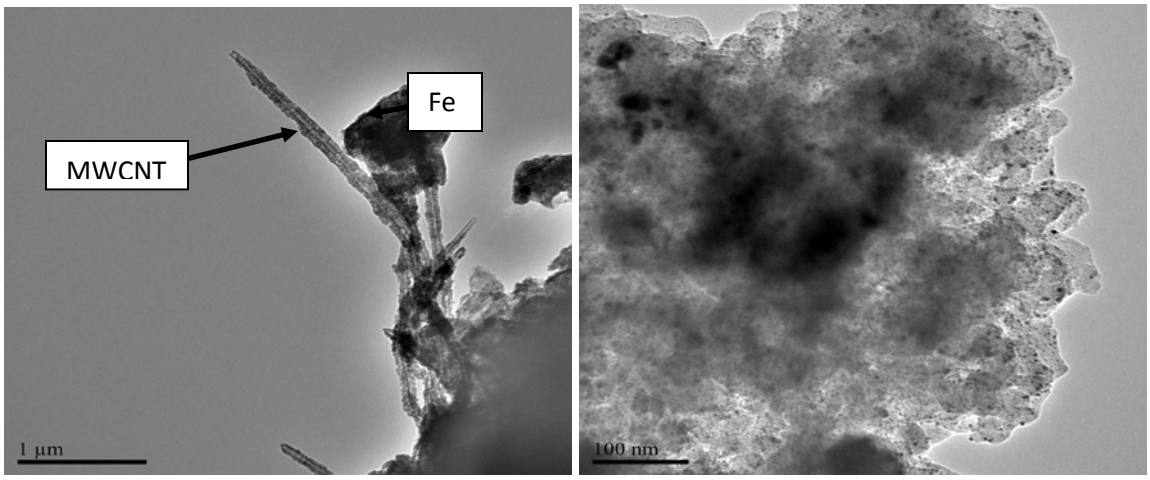

(a)

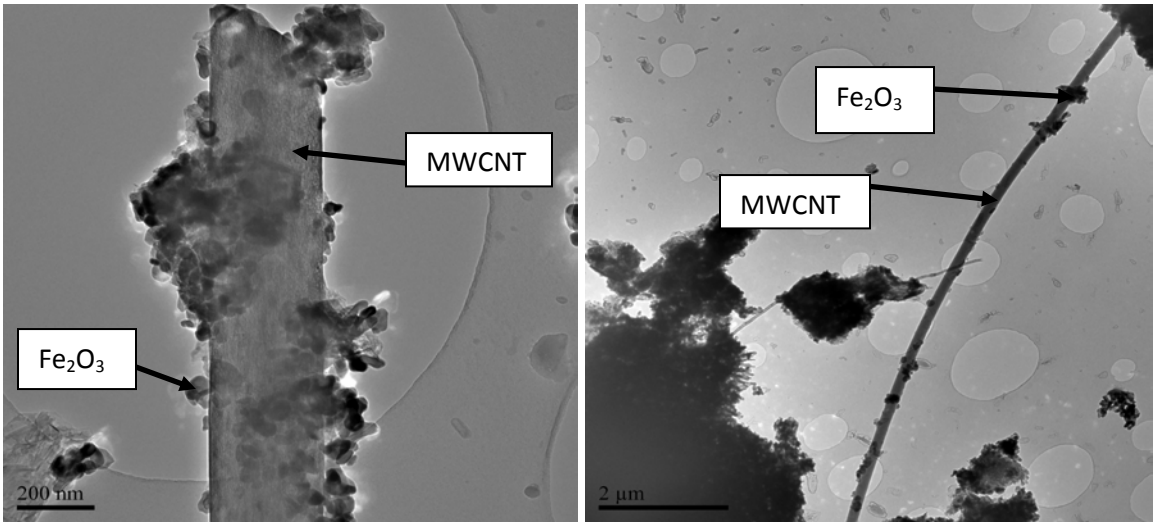

(b)

Figure 4.3: TEM images of **(a)** MWCNT-Fe at a magnification of 1 µm and 100 nm and **(b)** MWCNT-Fe_2O_3 at a magnification of 200 nm and 2 µm.

In figure 4.4, TEM images of MWCNT-Ni nanocomposites are illustrated. MWCNTs appear to have open tips at the end as shown by an arrow in figure 4.4

(a). Ni nanoparticles are seen as a black powder on the surface of the oxidized MWCNT.

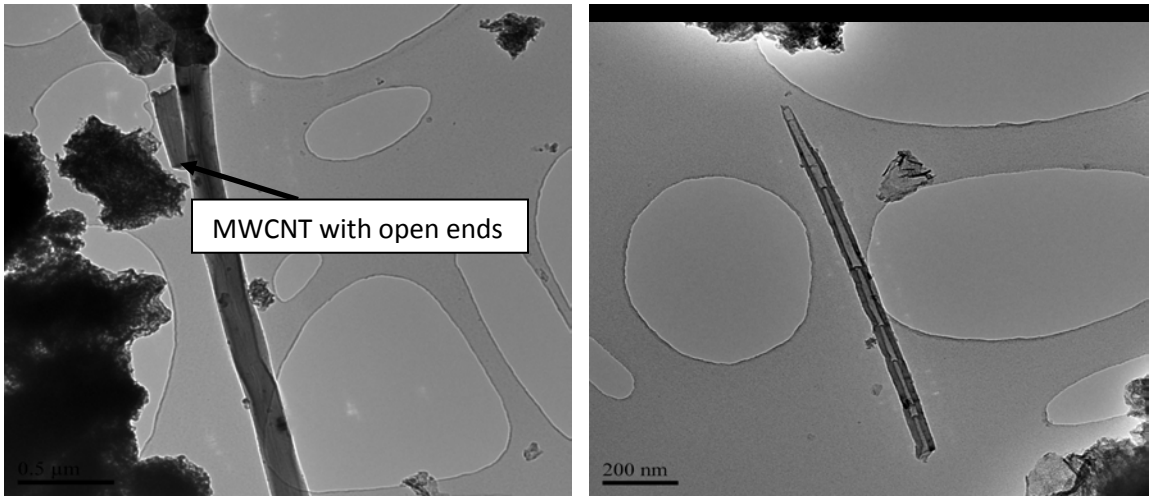

(a) **(b)**

Figure 4.4: TEM images of MWCNT-Ni nanocomposites at a magnification of **(a)** 0.5 µm and **(b)** 200 nm.

The low and high magnification TEM images of the purified carbon nanotubes decorated with uncalcined nickel nanoparticles are displayed in figure 4.5. Figure 4.5 shows TEM images at a magnification of **(a)** 0.5 nm, **(b)** 1 µm, **(c)** 50 nm and **(d)** 10 nm. Uncalcined Ni nanoparticles (as black powder) coated on the surface of the purified MWCNTs are clearly shown in figure 4.5 **(a)** and **(b)**. From the TEM images below, it can be seen that almost no traces of the amorphous carbon, carbon nanoparticles and metal particles were observed, indicating that the proposed purification process for the removal of the impurities coexisting with the MWCNTs was very efficient. Purification also results in opening of the caps which in turn increase the surface area of the MWCNTs [6]. In figure 4.5 **(c)** and **(d)**, a high magnification TEM images of the Ni-decorated MWCNTs are shown. The black powdered material shown by arrow in figure 4.5 **(a)**, **(b)** and **(c)** are the uncalcined nickel nanoparticles coated on the surface of the MWCNTs. The

arrow in figure 4.5 **(d)** shows the MWCNTs coated with uncalcined nickel nanoparticles.

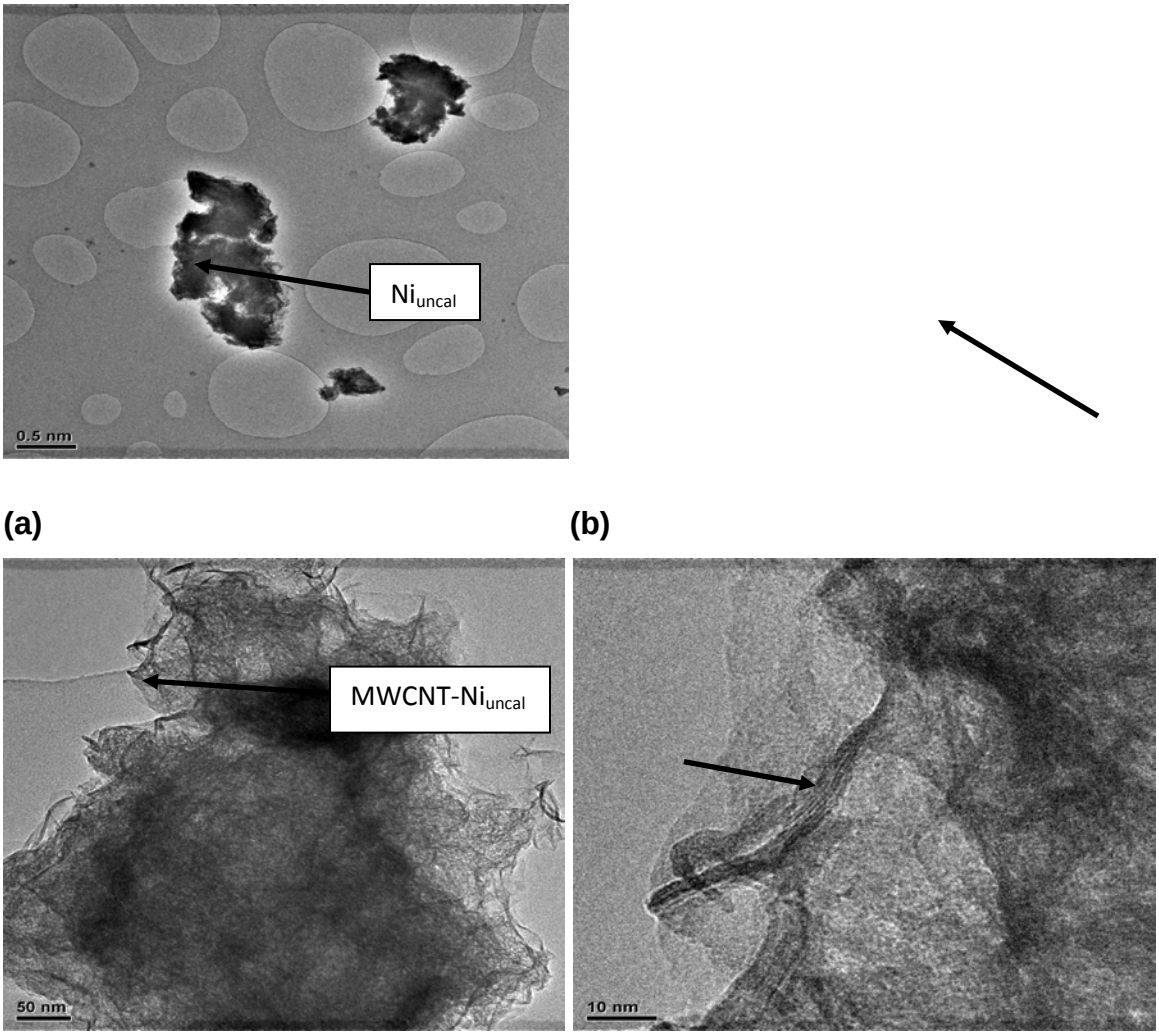

(a) **(b)**

(c) **(d)**

Figure 4.5: TEM images of the purified multi-walled carbon nanotubes decorated with uncalcined nickel nanoparticles (black powder) at a magnification of **(a)** 0.5 nm, **(b)** 1 µm, **(c)** 50 nm and **(d)** 10 nm.

TEM images for the calcined Ni nanoparticles decorated MWCNTs at a magnification of **(a)** 20 nm, **(b)** 50 nm, **(c)** 50 nm and **(d)** 100 nm are shown in figure 4.6. From these images, aggregation of Ni nanoparticles can be observed, and the calcined Ni nanoparticles are highly dispersed on the surface of the

MWCNTs as shown clearly in figure 4.6 **(c)** and **(d)**. Almost all uncalcined Ni nanoparticles are coated on the MWCNTs surface. From these TEM images, it can be said that the method employed for decoration of MWCNTs with metal oxides and metal nanoparticles was efficient. The arrow in figure 4.6 **(a)**, **(b)** and **(c),** shows the calcined nickel nanoparticles as a black powder. The arrow in figure 3.5 **(d)** shows MWCNTs well dispersed with calcined nickel nanoparticles.

The deposition of uniformly dispersed nanoparticles on the CNTs is believed to be due to the results of uniform surface functional sites on all nanotubes that can be created in the chemical-wet oxidation of nitric acid. During the surface modification process, the surface oxides may act as active sites in adsorbing with Ni ions, thus forming intermediate complex in aqueous phase. It is well known that oxygen functional groups such as carboxyl, hydroxyl and carbonyl impart the surface polarity, i.e., surface electrostatic field, to carbon surfaces [7]. Therefore, it can be said that it was these oxygen functional groups (as shown in the FT-IR spectra below) that has made it possible for Ni nanoparticles to be successfully coated on the MWCNTs.

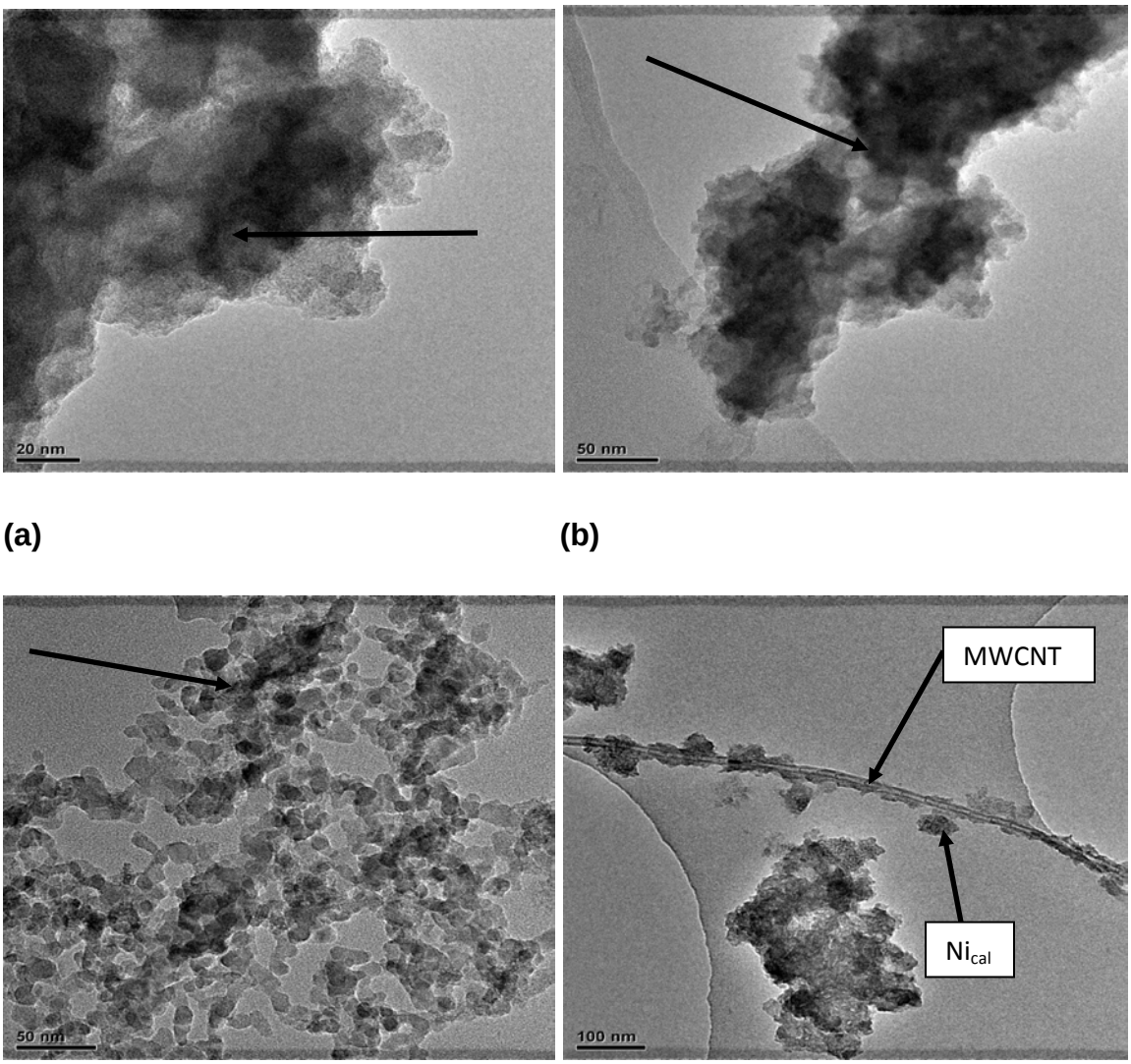

Figure 4.6: TEM images for the calcined Ni nanoparticles decorated MWCNTs at a magnification of **(a)** 20 nm, **(b)** 50 nm, **(c)** 50 nm and **(d)** 100 nm.

4.3.2 Scanning electron microscopy (SEM) analysis

SEM images of Cu and CuO nanoparticles are shown in figure 4.7 **(a)** and **(b)** respectively. CuO appears to be spongy with defective sites. The nanocomposite powders images of MWCNTs dispersed with Cu and CuO nanoparticles are shown in figure 4.7 **(c)** and **(d)** respectively. As compared to figure 4.7 **(a)** and **(b)**, MWCNTs seems to be successfully attached with Cu and CuO powders.

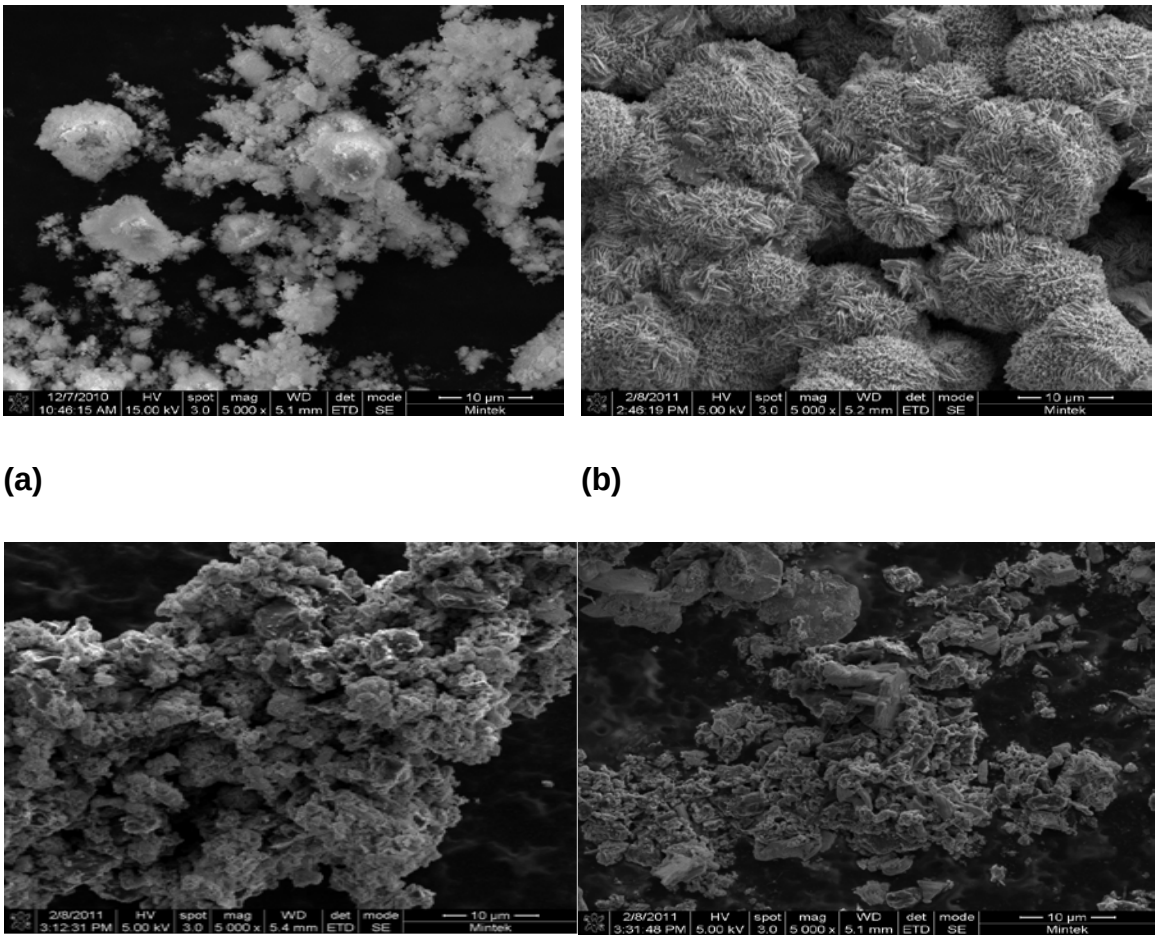

(a) **(b)**

(c) **(d)**

Figure 4.7: SEM images illustrating **(a)** Cu, **(b)** CuO, **(c)** MWCNT-Cu and **(d)** MWCNT-CuO at a magnification of 10 µm.

The SEM images of Fe and Fe_2O_3 nanoparticles are presented in figure 4.8 **(a)** and **(b)** respectively. Both nanoparticles appear to be bulky in size. Figure 4.8 **(c)** and **(d)** illustrate the SEM images of the MWCNT-Fe and MWCNT-Fe_2O_3 nanocomposites respectively. Some of the Fe_2O_3 nanoparticles appear to be spherical in shape. The single headed arrow in figure 4.8 **(c)** shows the oxidized MWCNTs with the double headed arrow depicting the Fe nanoparticles. In figure 4.8 **(d)**, the single headed arrow also represents MWCNTs with the double headed arrow showing Fe_2O_3 on the surface of the MWCNTs.

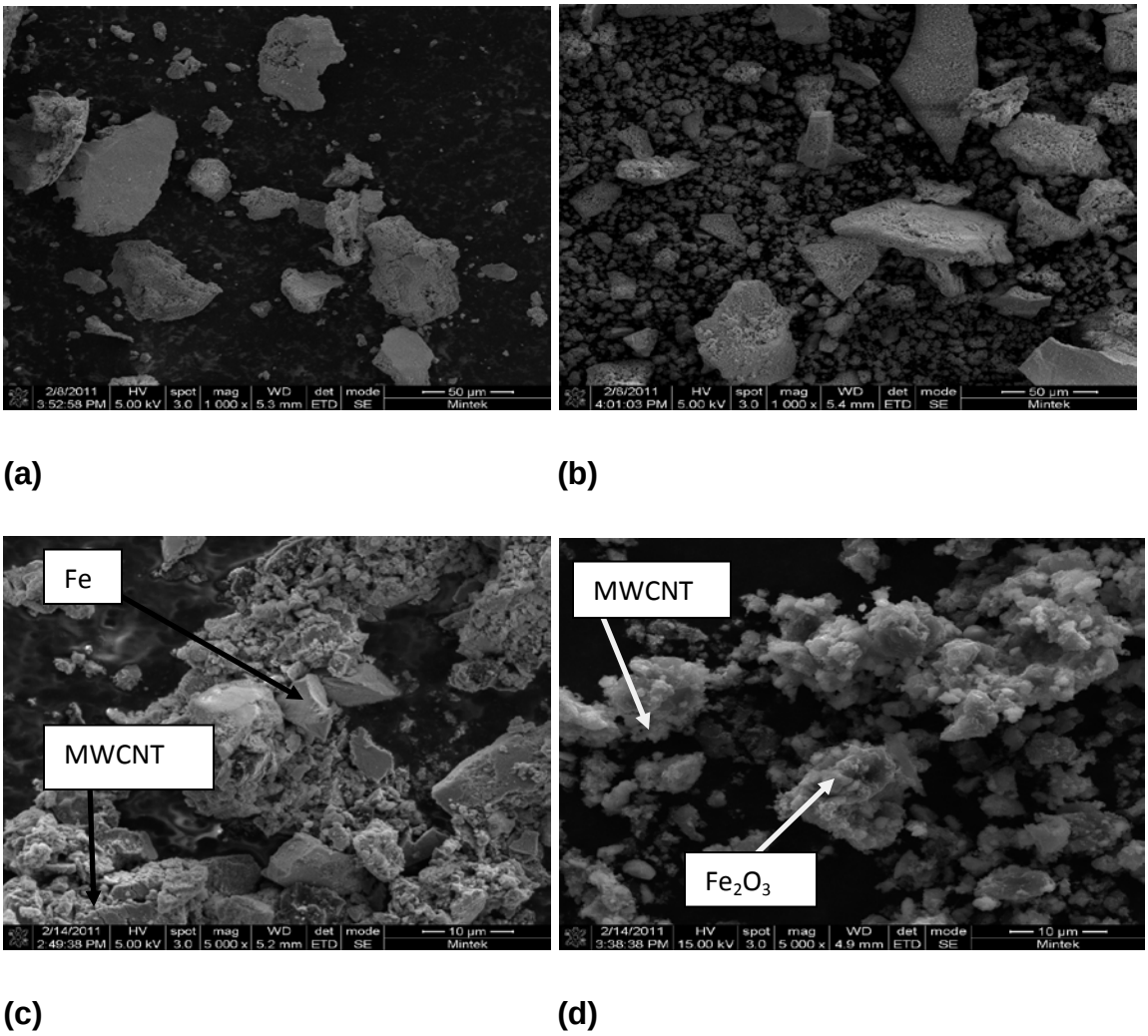

(a) **(b)**

(c) **(d)**

Figure 4.8: SEM images showing **(a)** Fe, **(b)** Fe_2O_3, **(c)** MWCNT-Fe and **(d)** MWCNT-Fe_2O_3.

The surface morphology of Ni and NiO nanoparticles is shown in figure 4.9 **(a)** and **(b)** respectively. At the same magnification, SEM images shows Ni nanoparticles being smaller in size than the NiO nanoparticles as shown in figure 4.9 **(a)** and **(b)**. The SEM images in figure 4.9 (a) also shows a very small spherical shaped Ni nanoparticles similar to the ones synthesized by Haque *et al*. [8]. SEM morphological images of MWCNT-Ni nanocomposite are depicted in figure 4.9 **(c)** and **(d)** at a magnification of 100 µm and 10 µm respectively. SEM images shows Ni nanoparticles well dispersed on the surface of the MWCNTs.

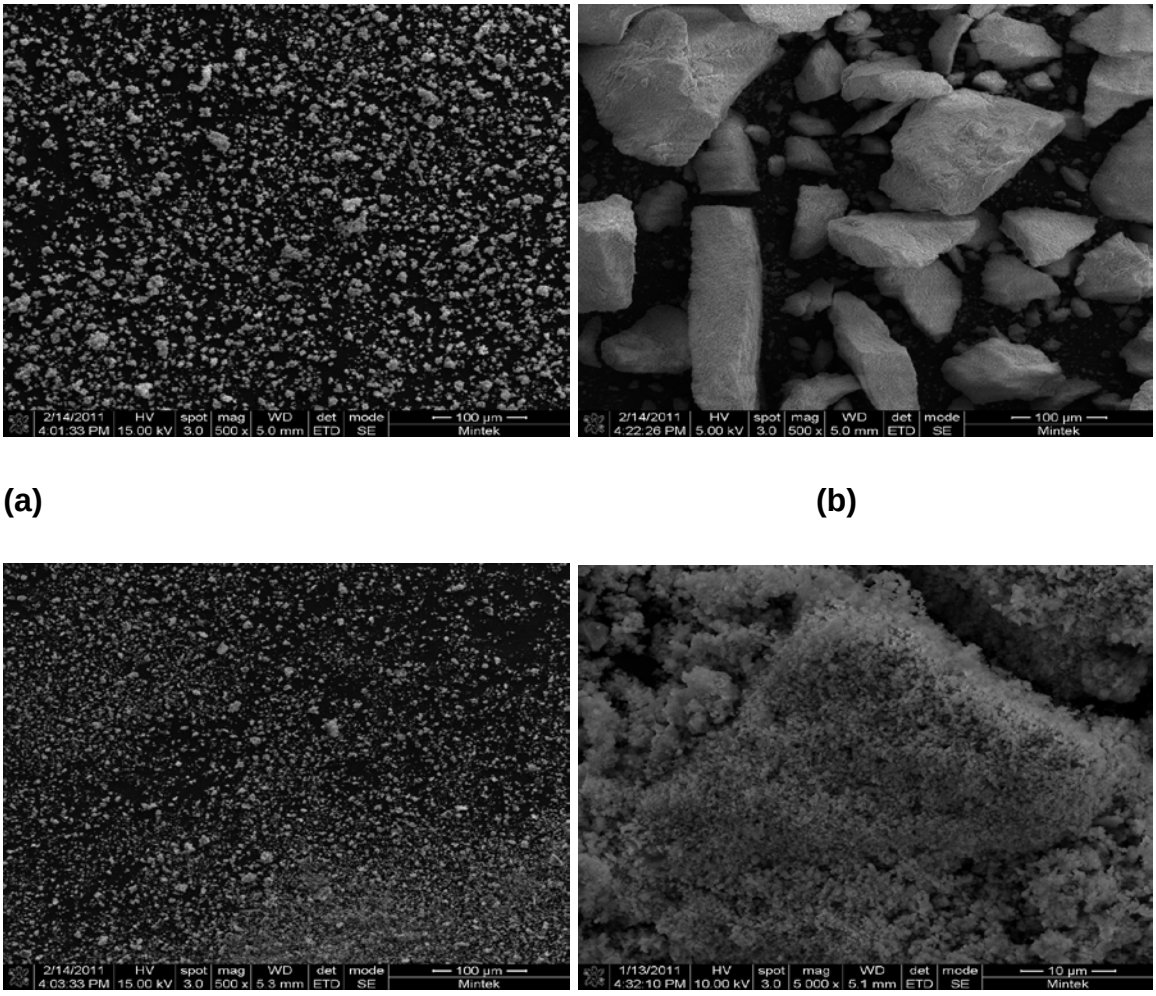

Figure 4.9: SEM micrographs depicting **(a)** Ni, **(b)** NiO, **(c)** MWCNT-Ni at a magnification of 100 µm, and **(d)** MWCNT-Ni at a magnification of 10 µm.

4.3.3 X-ray diffraction (XRD) results

The powder XRD pattern (Cu Kα λ = 1.5406 Å) of the as-synthesized MWCNTs samples prepared by the pyrolysis of iron (II) phthalocyanine is shown in figure 4.10. The peaks for the as-prepared MWCNTs arrays are indexed to (002), (101) and (004) reflections of hexagonal graphite and catalytic impurities, similar to the XRD pattern of the as-prepared MWCNTs studied by Mahanandia *et al*. [9]. It is expected from the XRD pattern of the purified MWCNTs not to contain the diffraction peak for the catalytic impurities and amorphous carbon.

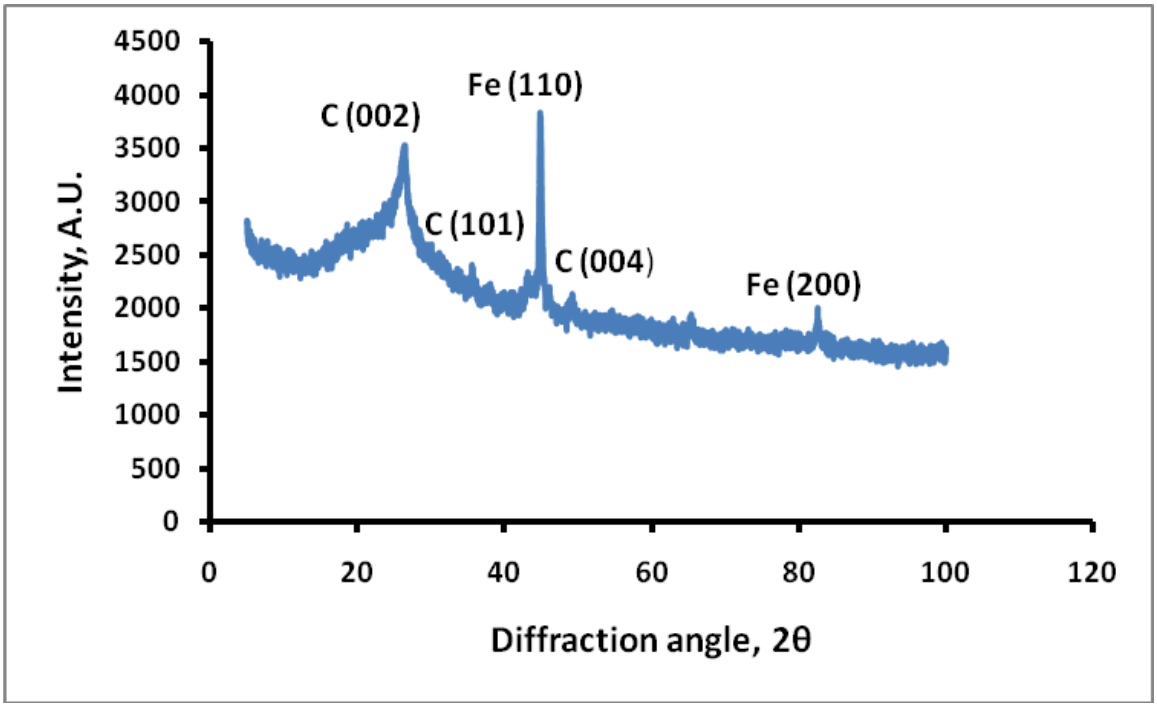

Figure 4.10: XRD pattern of the as-prepared MWCNTs synthesized from pyrolysis of iron (II) phthalocyanine.

4.3.4 Fourier transform infrared (FTIR) analysis

Figure 4.11 represents the FTIR spectrum of the as-prepared MWCNTs. A sharp band at 3746 cm^{-1} and broad one at 2628 cm^{-1} are attributed to the presence of the O-H groups of the monomeric carboxylic acid and hydrogen bonded carboxylic acid respectively on the surface of the as-prepared MWCNTs. It is believed to be resulting from ambient atmospheric moisture or oxidation during preparation of the MWCNTs [10, 11]. Similar results were reported by Vesali *et al*. [12]. The C=C group for MWCNTs is represented by the frequency at 1546 cm^{-1}, which was also reported by Vesali *et al.* [12] in their FT-IR studies of the as-prepared MWCNTs.

A broad band at 1888 cm^{-1} is due to the C=O stretch of the carboxylic acid (COOH) group. The peaks at 2286 cm^{-1} and 2101 cm^{-1} are attributed to the CΞN and CΞC respectively [13].

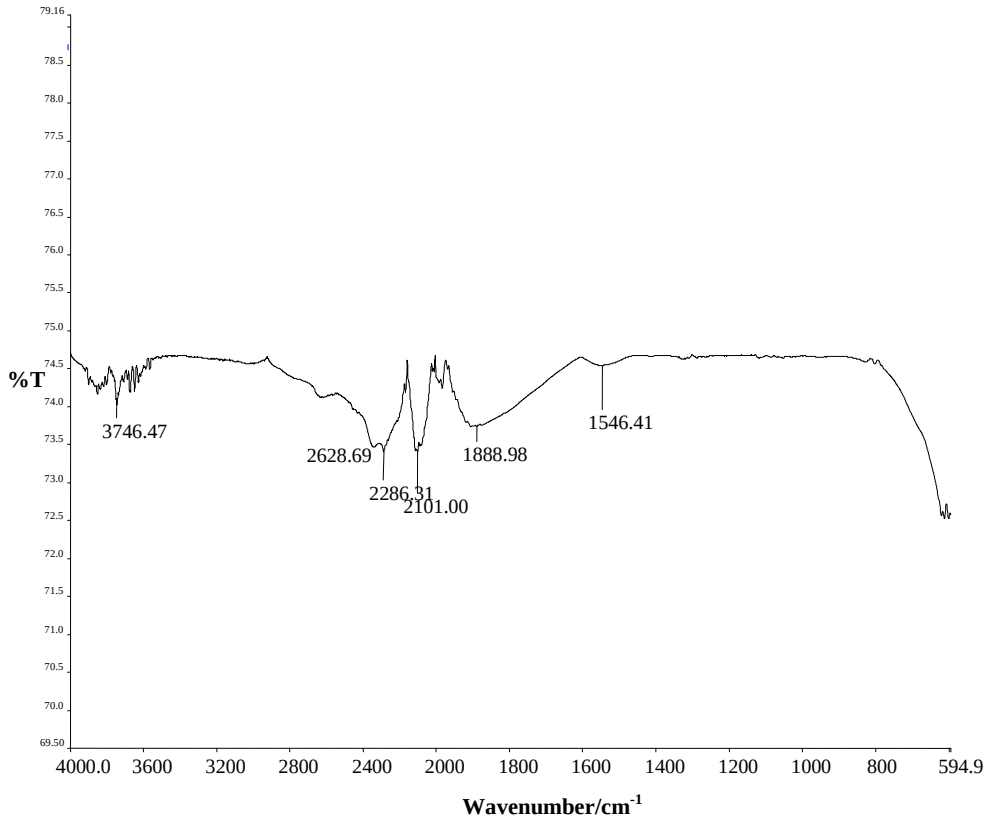

Figure 4.11: FTIR spectrum of the as-prepared MWCNTs from pyrolysis of iron (II) phthalocyanine.

FT-IR spectrum of MWCNTs purified by treatment with a mixture of H_2SO_4 and HNO_3 in a 3:1 ratio respectively for 30 min at 80 ^oC and washed with 900 ml distilled water and thereafter dried at 80 ^oC for 4hrs is shown in figure 4.12. Figure 4.12 shows the disappearance of the band at 3746 cm^{-1} and the appearance of a band at a lower frequency of 1358 cm^{-1} assigned for the presence of C-H group of the alkane [14]. The band for the O-H group of the carboxylic acid is attained at a frequency of 2654 cm^{-1}. The presence of new sharp bands at a lower frequency range of 500-600 cm^{-1} confirms the presence of the C-H functional group of the alkene. All the difference peaks of the as-prepared MWCNTs and purified MWCNTs confirm a successful purification of the CNTs [15].

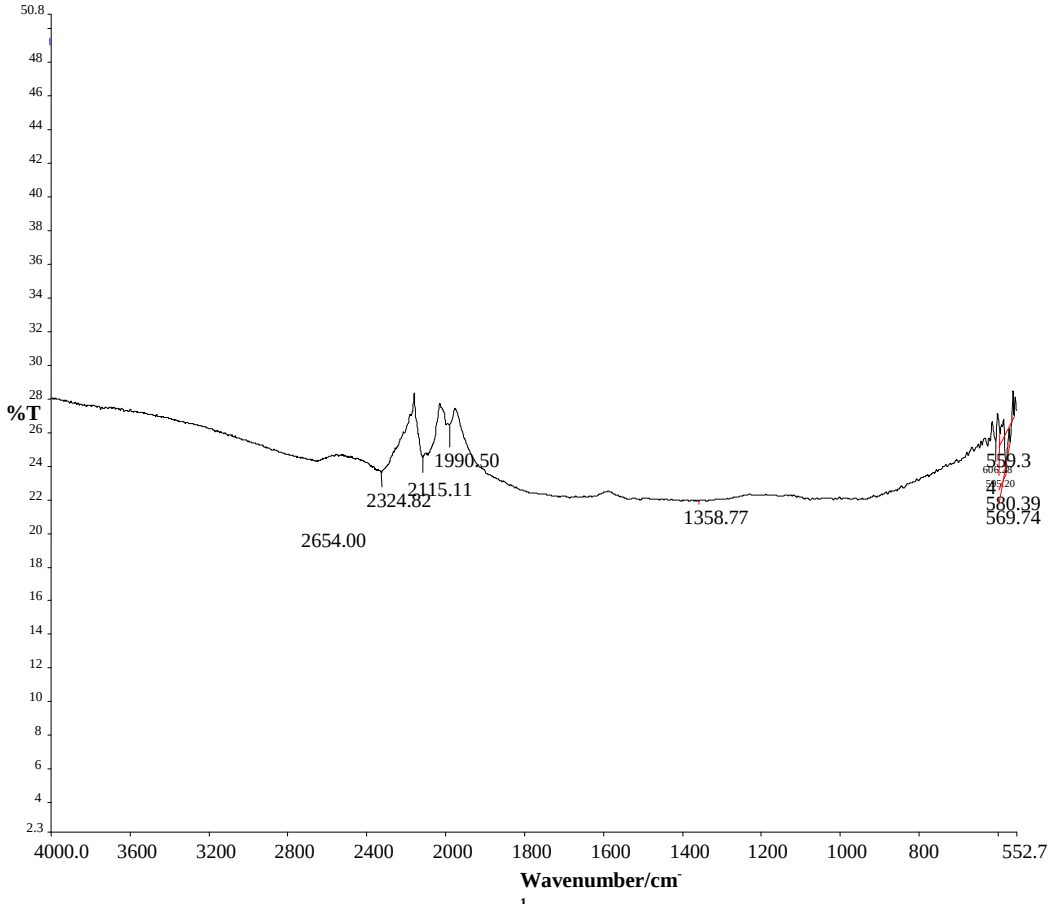

Figure 4.12: FT-IR spectrum of MWCNTs purified by treatment with a mixture of H_2SO_4 and HNO_3 in a 3:1 ratio for 30 min at 80 ^oC.

4.3.5 Electrochemical activity of MWCNTs, Fe_2O_3, Fe, CuO, Cu, NiO and Ni towards hydrogen storage

Since their discovery, carbon nanotubes (CNTs) have attracted much attention due to a variety of technological applications such as gas separation, catalyst support, energy storage, environmental protection, and so on [16-19]. Among these applications, there has been increasing interest in CNTs as heterogeneous catalyst support Pioneer studies have pointed out that metal nanoparticles supported on CNTs provide an excellent catalytic activity [20-25]. For instance,

Xing has used sonochemical technique to deposit Pt nanoparticles onto the surface of the CNTs, exhibiting a great activity in electrochemical adsorption and desorption of hydrogen [20]. Fazle *et al*. [21] have indicated that Li-doped CNTs produced a higher hydrogen-storage capacity, which is six times higher than undoped CNTs. Kim *et al.* [22] also indicated that Ni nanoparticles impregnated MWCNTs improves the hydrogen uptake capacity.

Herein, the results for the effect of decorating carbon nanotubes with metal oxides and metal nanoparticles are discussed.

4.3.5.1 Effect of purifying the MWCNTs

Hydrophobic and inert nature of the surface of as-prepared carbon nanotubes is unfavorable for their applications. In order to improve the interaction of CNTs and foreign molecules it is necessary to modify the surface of carbon nanotubes. Oxygen-containing groups which are interesting to improve the interaction of carbon nanotubes with the solvent matrix are formed on the surface of the carbon nanotubes by chemical treatment such as nitric acid [23-25]. The purification of carbon nanotubes has attracted great attention because of their many applications such as their use in electronic devices, gas storage, chemical and biological sensor [19]. The presence of impurities hinders their applications and therefore, the carbon nanotubes used must be of high purity [26]. The carbon nanotubes are usually contaminated with metal catalyst, amorphous carbon and graphitic nanoparticles. A large number of purification methods have been reported, but refluxing with nitric acid has been the treatment that has been employed most often [27]. The major function of nitric acid treatment is to remove the metal catalyst, perhaps together with some of the amorphous carbon. Because it is an oxidant, nitric acid may serve to oxidize the carbon atom at the end of the carbon nanotubes. It was reported that refluxing CNTs in nitric acid opens the ends of the CNTs and introduces the carboxylic acid groups at the

open ends and at defect sites of the CNTs [28, 29]. This study was conducted with a KOH electrolyte temperature of 25 ^{o}C.

4.3.5.1.1 Cyclic voltammetric response for the as-prepared and purified MWCNTs

Cyclic voltammetric measurement is helpful to understand the macroscopic electrochemical surface reactions at the electrode during charging and discharging process [30]. Figure 4.13 compares the exchange current density for as-prepared MWCNTs with the purified MWCNTs. Purified MWCNTs shows a high current respond due to their high conductivity, surface area and pore structure. The presence of acidic groups on the surface of the oxidized MWCNTs was confirmed by the FT-IR in figure 4.11 and 4.12. The cyclic voltammogram for oxidized MWCNTs is more rectangular in shape than for as prepared MWCNTs, indicating a typical electric double layer behavior [30]. The as-prepared MWCNTs clearly show faradaic redox reactions which are observed at a potential of -0.4 V (vs. Ag/AgCl), reference electrode representing oxidation and reduction processes. This is an indication of the reversible electron transfer behavior of as-prepared MWCNTs. Bare GCE is shown by a blue color with no peak. Since MWCNTs were prepared from pyrolysis of iron (II) phthalocyanine, the impurities expected are amorphous carbon and iron nanoparticle [31]. The peaks may be due to the iron nanoparticles present on the surface of the MWCNTs as was shown by the XRD in figure 4.10 and TEM (see TEM images in figure 4.1). At high scan rate, the width of the CV wave tend to increase as shown by that of the purified MWCNTs below which indicate the transfer on more ions to the surface of the electrode.

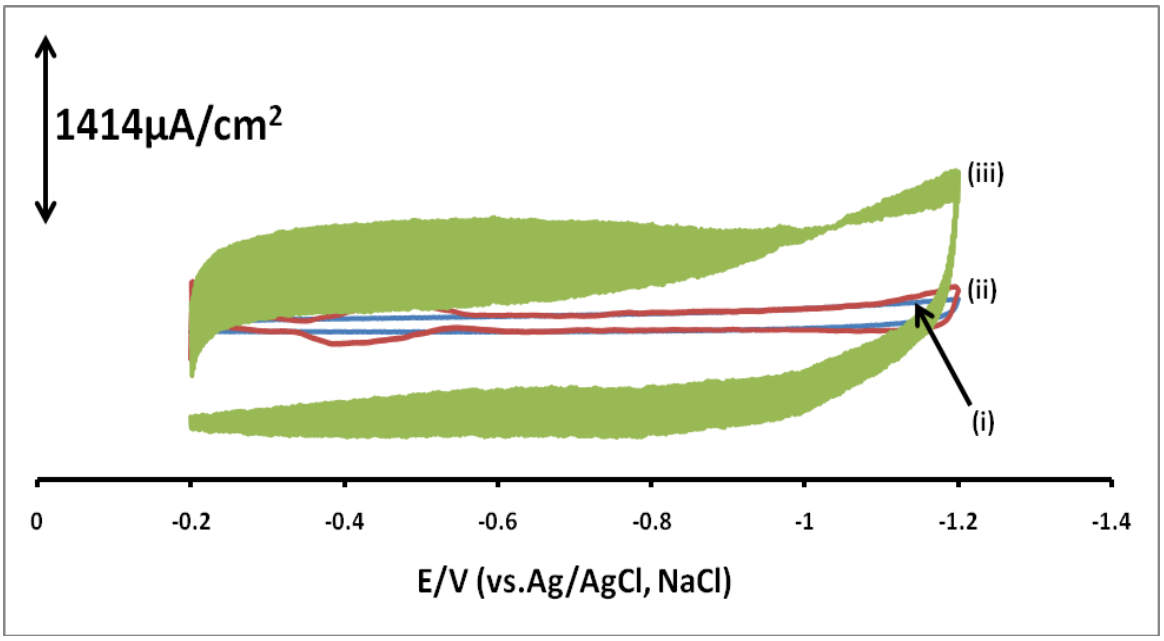

Figure 4.13: Cyclic voltammetric profiles for **(i)** bare GCE, **(ii)** As-prepared MWCNTs and (iii) Oxidized MWCNTs showing the purification effect in a 6 M KOH electrolyte. Scan rate=100 mV/s.

4.3.5.1.2 Controlled potential electrolysis studies for the as-prepared and purified MWCNTs

High discharge capacity for hydrogen depends on the MWCNTs surface area, presence of metal nanoparticles, pore volumes of the MWCNTs and the openness of the pores of the MWCNTs. Transmission electron microscopy in figure 4.4 showed that the synthesized MWCNTs have open ends responsible for hydrogen to diffuse. The discharge voltages of as-prepared MWCNTs, and purified MWCNTs as obtained in chronopotentiometry (*applied current of 1 µA*) are - 0.525 V and - 0.510 V respectively. These discharge voltages were applied in the following CPE studies. The as-prepared MWCNTs show a high discharge capacity than purified MWCNTs as shown in figure 4.14. These results are consistent with the charge-discharge profiles were the as-prepared MWCNTs

were discharged and charged to high voltages. This may be due to the presence of iron nanoparticles which tend to increase the catalytic activity and surface area of the MWCNTs. Iron nanoparticles were reported to promote the formation of defective sites on the MWCNTs surface where hydrogen adsorb chemically [32]. The chemical adsorption process is improved by the presence of iron catalyst in which the atomic hydrogen occupies sites which would be prevented from adsorption in purified MWCNTs. Dispersion on iron nanoparticles over MWCNTs creates defect sites which enhance the hydrogen storage by adsorption of atomic hydrogen at these sites. The opening of the caps results in an increase in the exposed surface area of the MWCNTs. However, the acid treatment to open the caps did not significantly increase the discharge capacity. Similar results were observed by Hyeok *et al*. [30] during high capacitance studies using nanocomposite electrode of single-walled carbon nanotubes and polypyrrole.

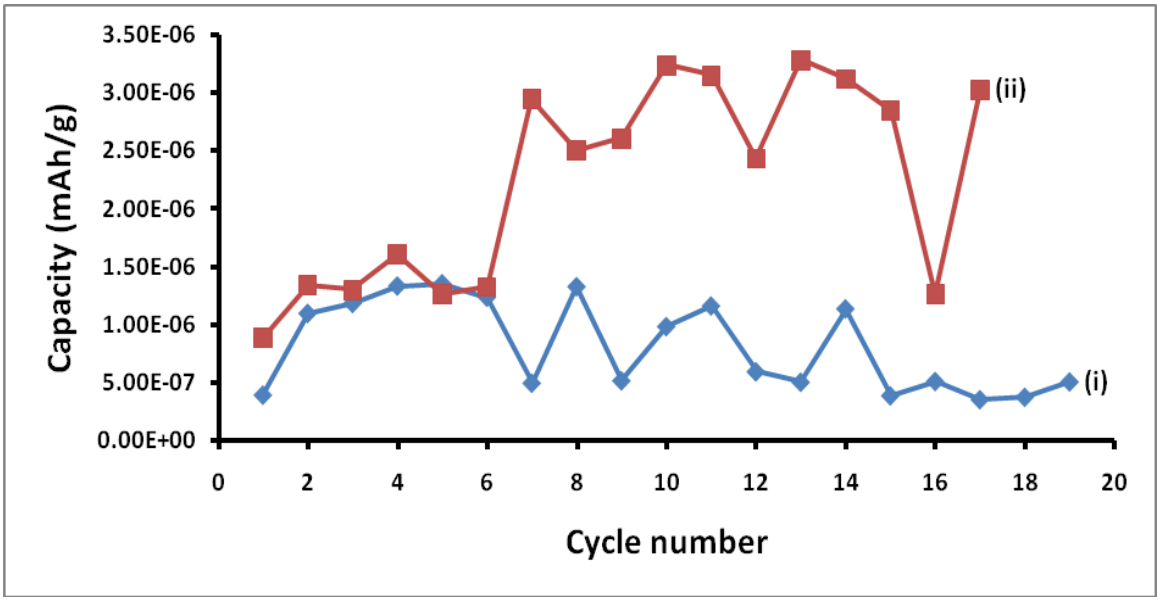

Figure 4.14: Plots comparing the discharging capacity of **(i)** purified MWCNTs and **(ii)** as-prepared MWCNTs as a function of cycle number.

The as-prepared MWCNTs have a short cycle life compared to the oxidized MWCNTs with the maximum capacity of as-prepared MWCNTs obtained at cycle

number 13 and cycle number 5 (five) for the purified MWCNTs. Hydrogen atoms appears to favor binding on the sidewalls of the MWCNTs where there is Iron nanoparticles than on the inside of the purified MWCNTs after the caps and pores have been opened. The result shows that the discharge capacity of acid treated MWCNTs decreases dramatically compared to the as-prepared MWCNTs. It is expected that after decoration with metal catalyst, the capacity should increase significantly. This indicates that the electrochemical hydrogenation of MWCNTs is influenced by the catalytic effect. It is therefore suggested that MWCNTs of higher purity or acid treated MWCNTs have a lower discharge capacity.

4.3.5.2 Effect of the NaOH and KOH electrolyte types

Electrolytes are substances that consist of charged particles called ions. When electrolyte dissolves in water or polar solvents, they are ionized into positive and negative ions. In dilute aqueous solutions, the degree of ionic association and dissociation of NaOH and KOH is relatively stronger than their common salts at high temperatures [33-35]. Electrical conductance measurement of dilute aqueous alkali hydroxide solutions at high temperatures provide a unique means of determining the extent of the association of alkali metal ions with the OH^- ions. This knowledge is important in interpreting the thermodynamics of ion-ion and ion-water interaction and the pH of the solution [36, 37]. One of the disadvantages of alkali hydroxide electrolyte is that they are corrosive in nature. Especially NaOH and KOH, since they are strong bases and therefore strong electrolyte-dissociate almost completely into ions [38, 39].

$$KOH \text{ or } NaOH \xrightarrow{H_2O} K^+ \text{ or } Na^+ + OH^- \text{ , 100\% ionized.} \qquad \textbf{(Scheme 4.1)}$$

In dilute aqueous solutions, the degree of ionic dissociation of LiOH, NaOH and KOH is relatively stronger than their common salts at high temperatures and low densities, while LiOH (aq) is significantly higher than for NaOH (aq) and KOH (aq). Electrical conductance measurements of dilute aqueous alkali hydroxide solutions at high temperatures provide a unique means of determining the extent of dissociation of alkali metal ions with OH^- ions [24, 25]. Knowledge of the association constant of these hydroxides is important in interpreting the thermodynamics of ion-ion and ion-water interactions, as well as providing a fundamental parameter in determining the pH of the solutions in extreme conditions [40, 41].

4.3.5.2.1 Comparative cyclic voltammetric response for the NaOH and KOH electrolytes

The cyclic voltammetry curves in figure 4.15 compares the effect of electrolyte type on the current density produced by using the GCE-MWCNT-Ni (2wt% MWCNTs and 4wt% Ni) electrode (2wt% MWCNTs and 4wt% Ni nanoparticles were chosen due to high discharge capacities produced during MWCNTs and Ni nanoparticles loading studies). In figure 4.15, it can be observed that the 6 M NaOH electrolyte have a high current density at an applied potential of -1.17 V (vs. Ag/AgCl) compared to the 6 M KOH electrolyte.

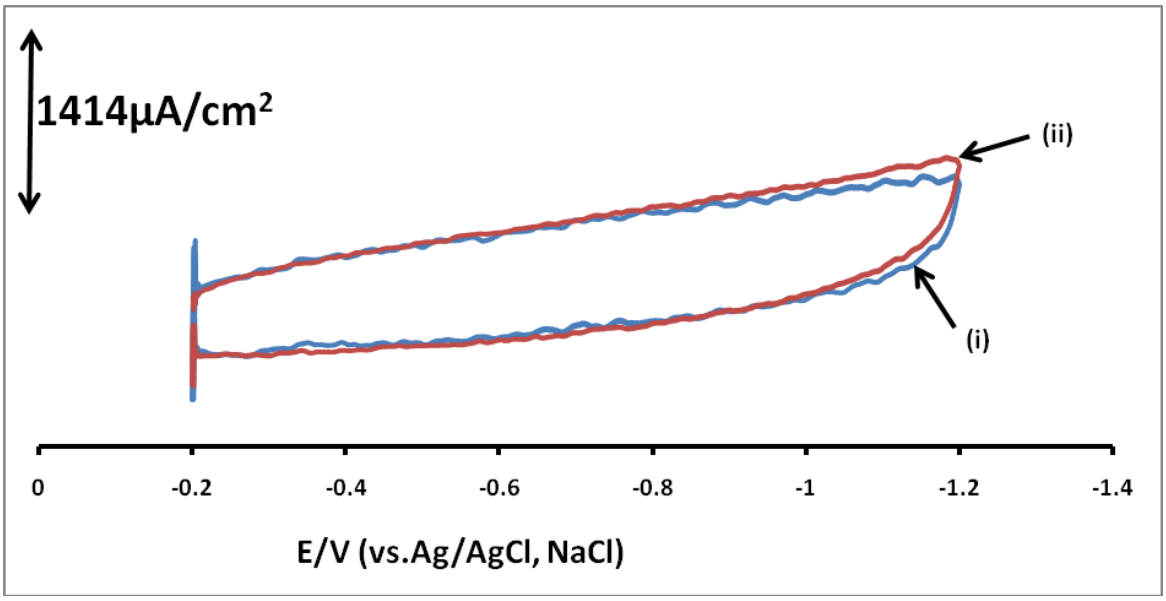

Figure 4.15: Cyclic voltammograms of **(i)** 6 M KOH and **(ii)** 6 M NaOH electrolytes at a scan rate of 100 mV/s using GCE-MWCNT-Ni (4wt% Ni).

4.3.5.2.2 Charge-discharge studies for the NaOH and KOH electrolytes

The use of the 6 M KOH electrolyte results in high charge voltage (-0.073 V), as shown in figure 4.16. This is due to KOH electrolyte having ions that conduct high electricity than the NaOH electrolyte. The 6 M NaOH gave a high discharge voltage (-0.944 V) than 6 M KOH. Aqueous sodium hydroxide solution is the electrolyte preferred to be used in supercapacitive studies due to its salt resistance, low reactivity and less corrosive than KOH (aq) [42]. KOH (aq) is more powerful in both gasification and intercalation, providing too much porosity useful for hydrogen storage in MWCNTs and useless for double layer capacitance than NaOH (aq) [42].

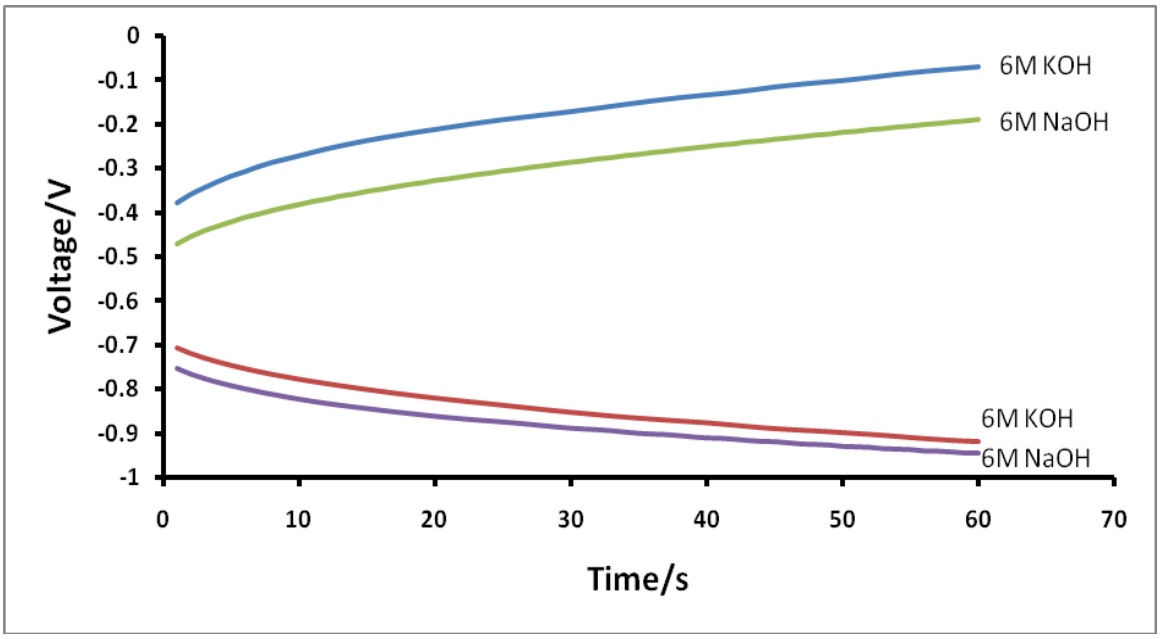

Figure 4.16: Voltage profile showing charge and discharge curves for 6 M NaOH and 6M KOH from an applied current of 1 µA.

4.3.5.2.3 Discharge capacity studies for the NaOH and KOH electrolytes

The plot of discharge capacity against cycle number in figure 4.17 compares the discharge capacity of 6 M NaOH and 6 M KOH electrolyte. It can be seen that GCE-MWCNT-Ni (4wt% Ni) in 6 M KOH electrolyte (7.9E-06 mAh/g) gave more than half the discharge capacity of 6 M NaOH electrolyte (3.04E-06 mAh/g). These results are consistent with the charge profile were 6 M KOH electrolyte was charged to a high voltage than the 6 M NaOH electrolyte. The 6 M KOH electrolyte shows a short cycle life compared to 6 M NaOH which last up to cycle number 21. The 6 M NaOH electrolyte nearly lost capacity to zero at cycle number 9 (nine) before reaching stability in discharge capacity.

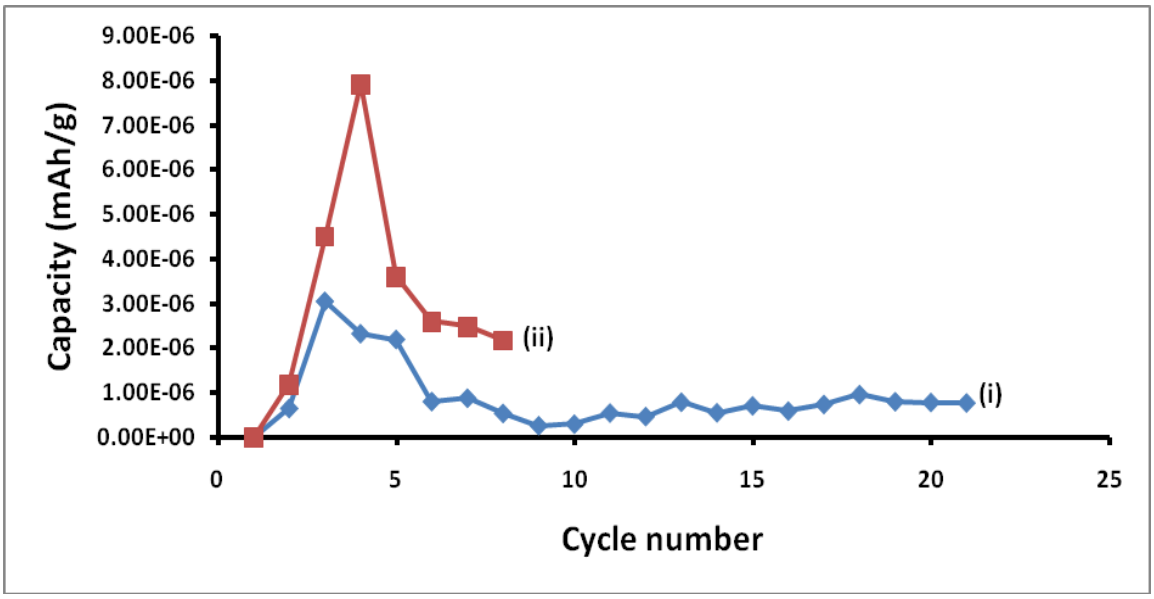

Figure 4.17: Plots comparing the discharge capacities of **(i)** 6 M NaOH and **(ii)** 6 M KOH electrolytes as a function of cycle number.

4.3.5.3 Effect of the KOH electrolyte concentrations

The concentration of the electrolyte solution determines the amount of the hydrogen ions (H^+) and hydroxyl ions (OH^-) present [43]. Therefore it is of interest to obtain the appropriate electrolyte concentration that will results in the maximum hydrogen storage in CNTs. The following studies investigate the effect of KOH electrolyte concentration on the current response, charge-discharge voltages and discharge capacity of the GCE-MWCNT-Ni (4wt% Ni) electrode for hydrogen.

4.3.5.3.1 Current response studies at different KOH electrolyte concentrations

The following study investigates the effect of the 2 M, 4 M, 6 M and 8 M KOH electrolyte concentration on the current response. The CV results in figure 4.18 **(a)** indicate that the electrolyte concentration has a great influence on the current density of GCE-MWCNT-Ni (4wt% Ni) electrode at 25 ^{o}C. The highest current density was obtained at 2 M KOH and the lowest at 6 M KOH. The results indicate that as the concentration of the electrolyte increases, the current density of GCE-MWCNT-Ni (4wt% Ni) decreases. Similar results were observed by Zhang *et al*. [44]. A change in current density with concentration implies that hydrogen diffusion was the control step at room temperature of 25 ^{o}C for discharge process of GCE-MWCNT-Ni (4wt% Ni) electrode [44].

Figure 4.18 **(b)** clearly shows the relationship between the current density and the electrolyte concentration. A decrease in current density can clearly be seen as the concentration increases. An increase in peak current is obtained at a concentration of 8 M KOH after a sharp fall as seen. Different electrolyte concentrations affect the surface state of the electrode. With an increase of electrolyte concentration, OH^- concentration of the electrode surface increases, but viscosity of the electrolyte also increases, slowing the diffusion velocity of the OH^-; so the OH^- concentration at the electrode surface decreases. When the electrolyte concentration is low, electrolyte concentration plays a role on OH^- concentration of the electrode surface, so the value of the diffusion coefficient is low [44]. This behavior is stressed by a CV profile in figure 4.18 **(a)**, which shows a decrease in current density as the KOH electrolyte concentration increases.

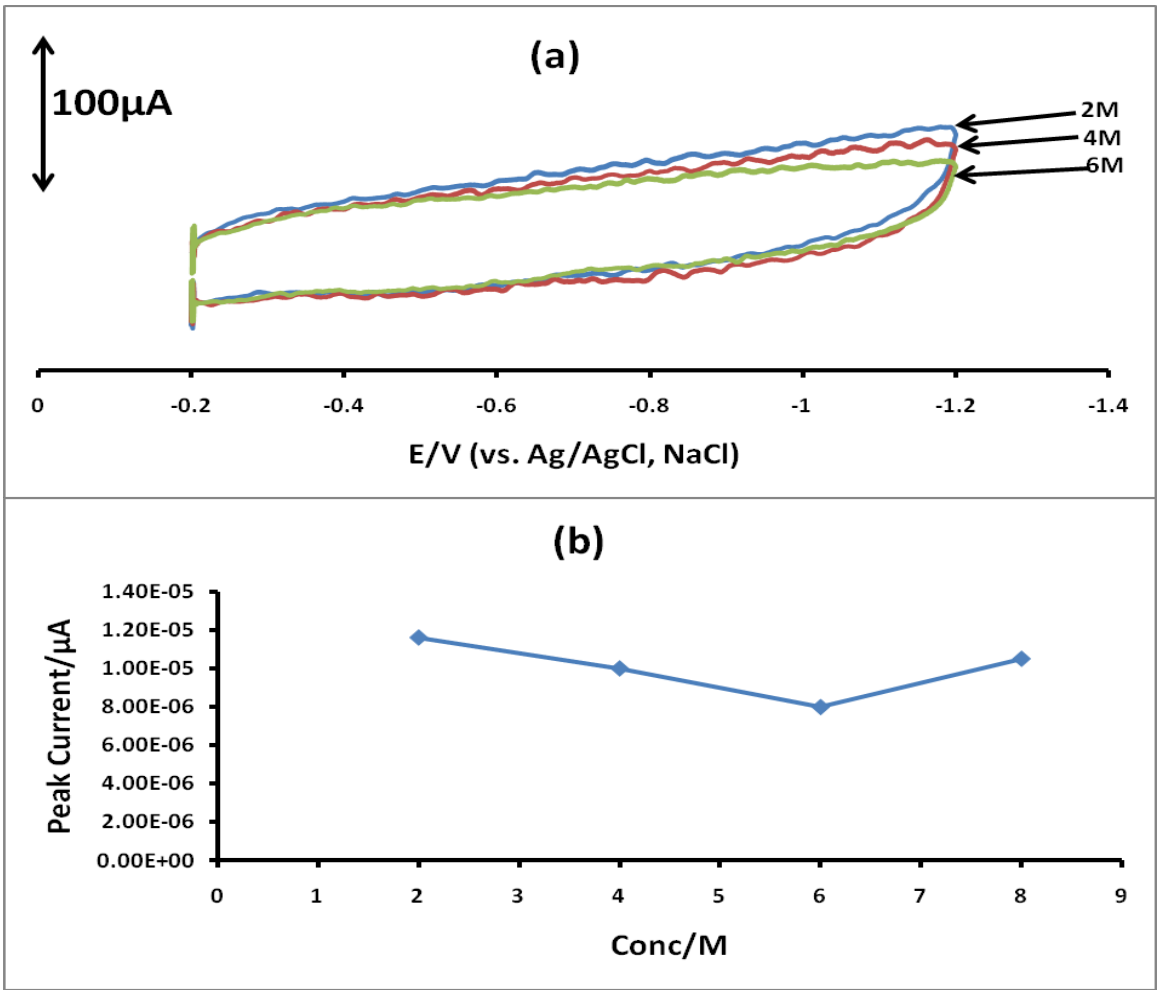

Figure 4.18: (a) Cyclic voltammetric profiles clearly showing a decrease in current density as the concentration of the electrolyte increases from 2 M to 6 M and **(b)** A plot of cathodic peak current against the concentration of the electrolyte. Scan rate = 100 mV/s.

4.3.5.3.2 Controlled potential electrolysis studies for different KOH electrolyte concentration

Figure 4.19 **(a)** shows that the maximum discharge capacity is reached at an electrolyte concentration of 6 mol/L, while the minimum discharge capacity is obtained by 8 M KOH electrolyte. A 6 M KOH electrolyte concentration has a

short life cycle compared to 8 M KOH electrolyte concentration. A maximum discharge capacity for 8 M KOH electrolyte concentration is reached at a small cycle number compared to the other electrolyte concentrations. Therefore, from figure 4.19 **(b)**, we can conclude that the 6 mol/L electrolyte concentration is the suitable concentration for hydrogen storage studies in GCE-MWCNT-Ni (4wt% Ni) and other working electrodes such as LaNi5 alloys. The kinetic property of the hydrogen storage alloy electrodes is related to electrochemical reaction on the surface of alloy particles and diffusion of hydrogen within the alloy, which are characterized by exchange current density and diffusion coefficient, respectively [44].

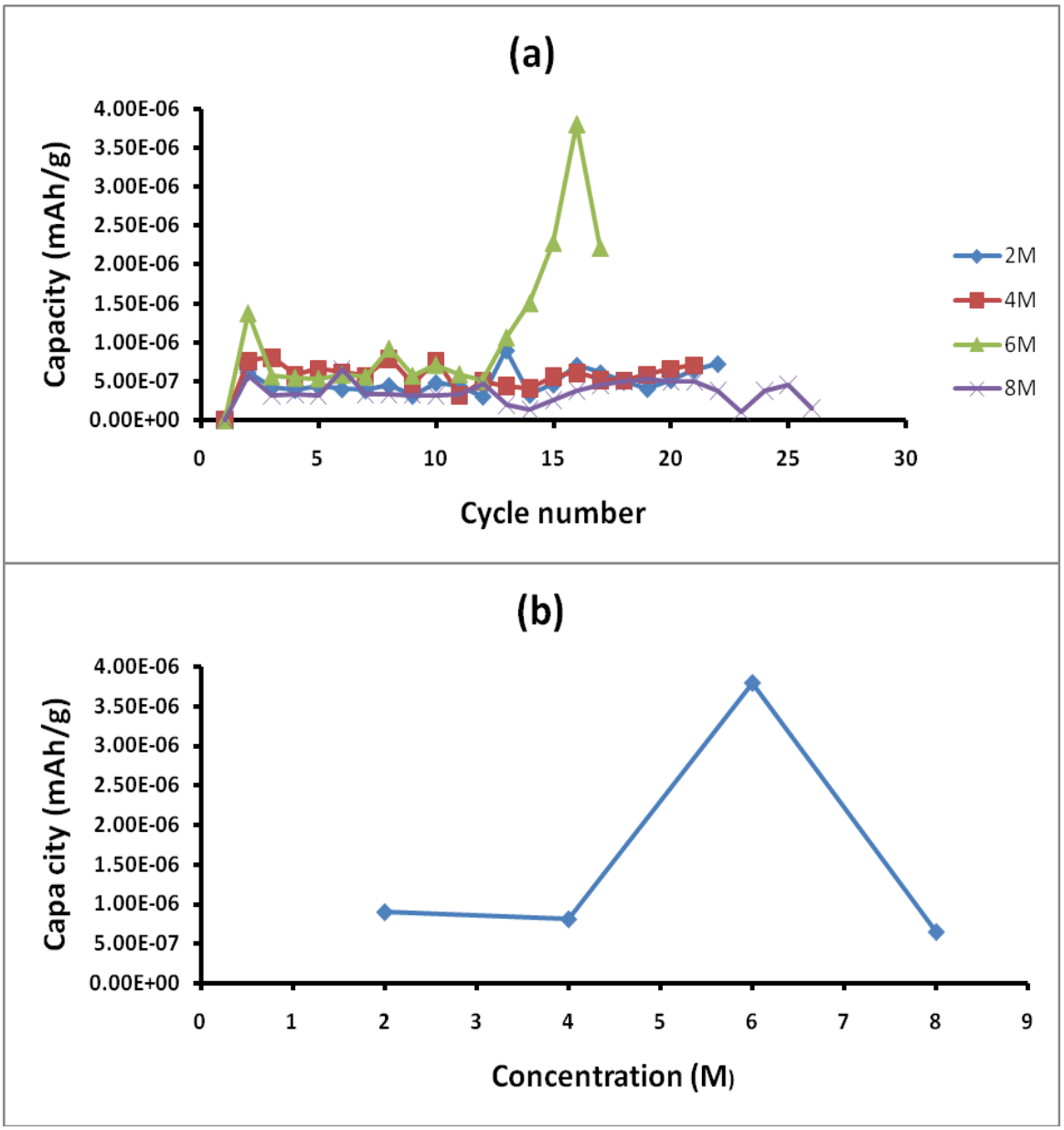

Figure 4.19: (a) The plots comparing the discharge capacity as a function of cycle number for different concentrations of the KOH electrolyte using GCE-MWCNT-Ni (4wt% Ni) and **(b)** the resulting plot of maximum discharge capacity against the concentrations.

4.3.5.4 Effect of the CuO decorated MWCNTs

Copper is a chemical element with atomic number 29. It is a ductile metal with very high thermal and electrical conductivity. The high electrical conductivity of copper is due to virtually all the valence electrons taking part in conduction [45-47]. Common oxidation states of copper include the less stable copper (I) state, Cu^{+}, and the more stable copper (II) state, Cu^{2+}, which forms a blue or blue-green salts and solutions [45].

There are two stable copper oxides, copper (II) oxide (CuO) and copper (I) oxide (Cu_2O). Copper (I) oxide was the first substance known to behave as a semiconductor [48, 49]. Much more interest focuses on the use of nano-scale copper oxide for catalyst use. The copper oxide may be used as a solid solution or as a mixture of mixed oxides [50, 51]. These nano-scale chemicals are produced through the thermal activation of copper salts such as copper nitrates [52].

4.3.5.4.1 Cyclic voltammetric analysis at the GCE-MWCNT-CuO electrode

Figure 4.20 shows the combined CV profiles of GCE, GCE-MWCNT, GCE-CuO and GCE-MWCNT-CuO electrodes. Note the absence of peaks in GCE. It is of interest to obtain cyclic voltammogram of rectangular in shape, as it is an indication of supercapacitive properties of MWCNTs. Supercapacitor are known for their high power density and longer cycle life compared to ordinary batteries which have only high energy density [30]. Two broad anodic peaks (at -0.5 and -1 V versus Ag/AgCl, NaCl) are observed for GCE-MWCNT in figure 4.20.

Transmission electron microscopy (see TEM images in figure 4.2) and scanning electron microscopy (see SEM images in figure 4.7) images showed CuO nanoparticles well dispersed on the surface of the oxidized MWCNTs. GCE-CuO

shows a sharp anodic peak at nearly -0.5 V. The broad peak is observed at similar position for GCE-MWCNT-CuO. This is an indication of good desorption (discharge) behavior of hydrogen from the working electrode. Similar results were reported by Feng *et al*. [53], who noted that the hydrogen reduction is observed during the cathodic potential sweep when the Ni-MWCNTs electrode is charged and the hydrogen oxidation peaks are observed during the anodic potential sweep when the electrode is discharging.

GCE-MWCNT-CuO shows a broad cathodic and anodic peak at a potential of -1 V. This shows that MWCNT are good material for storing and releasing hydrogen effectively. The synergistic effect of both CuO and MWCNTs can clearly be seen. As expected, GCE-MWCNT-CuO showed a high current respond compared to GCE-CuO and GCE-MWCNT electrodes.

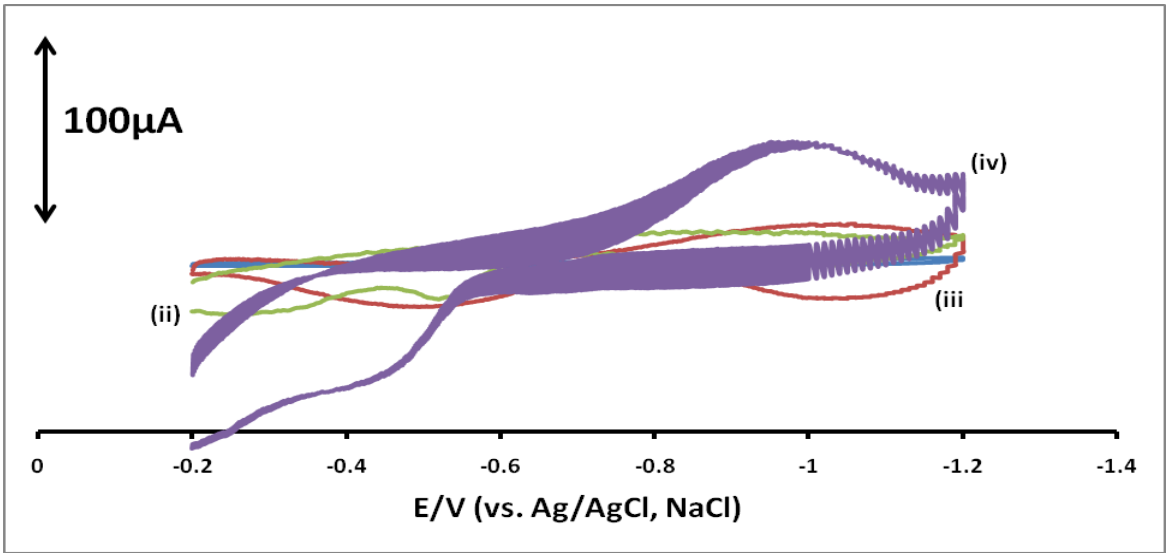

Figure 4.20: Cyclic voltammetric profiles of **(ii)** GCE-CuO, **(iii)** GCE-MWCNT and **(iv)** GCE-MWCNT-CuO at a scan rate of 50 mV/s.

Note that the CV profile of GCE (blue in color) is shielded due to its low current respond. The increase in current response is as follows: GCE < GCE-CuO < GCE-MWCNT < GCE-MWCNT-CuO.

4.3.5.4.2 Linear square voltammetry analysis at the GCE-CuO electrode

The stability of the GCE-CuO electrode was further investigated by the linear square voltammetry (LSV) to determine the anodic peak potentials and change in current response as the scan number is increased. It can be observed in figure 4.21 that as the scan number is increased, the anodic peaks shift to a more positive potential and the current response decreases. The decrease in catalytic current subsequent to repetitive scans is an implication of electrode contamination [54].

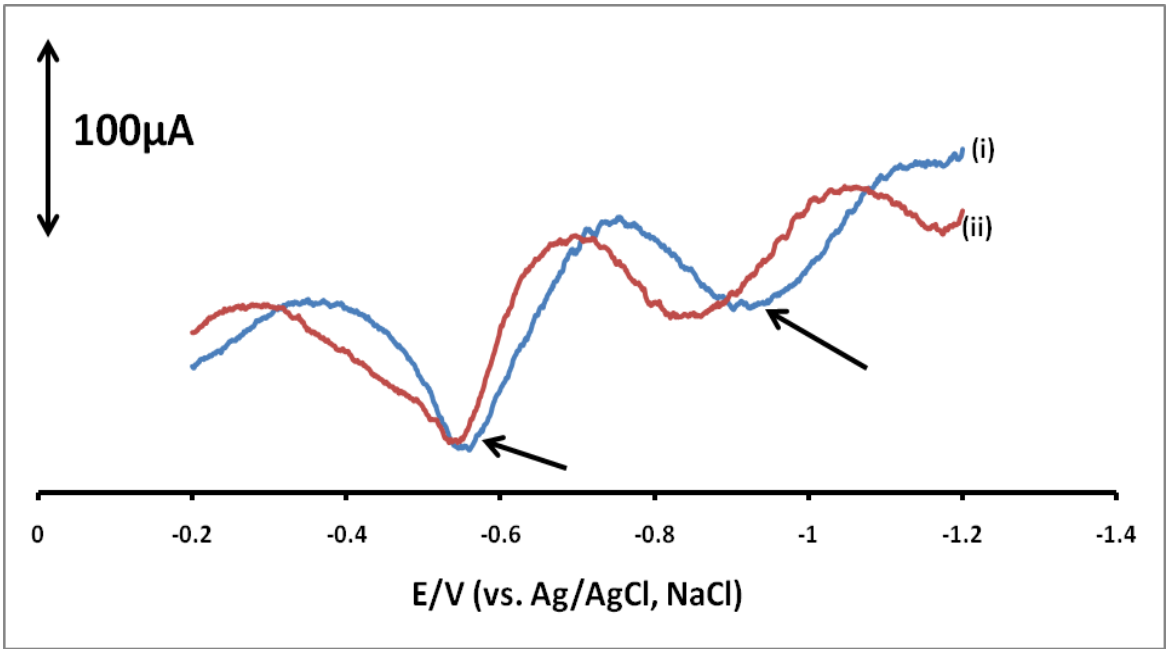

Figure 4.21: Linear square voltammetric profile for the reverse reaction of GCE-CuO at the **(i)** 1st and **(ii)** 2nd scan showing the two anodic peaks. Scan rate= 50 mV/s.

The second anodic peaks remained slightly at a potential of 0.55 V vs. Ag/AgCl reference electrode. At this stage it is not known what really caused the peak shifting observed in figure 4.21.

4.3.5.4.3 Effect of applied discharge current on the discharge voltage at the GCE-MWCNT-CuO electrode

As the applied discharge current is increased, the discharge voltage tends to decrease as shown in figure 4.22. This shows that the voltage is inversely proportional to the discharge current applied. Similar results were observed by Sabina *et al*. [55].

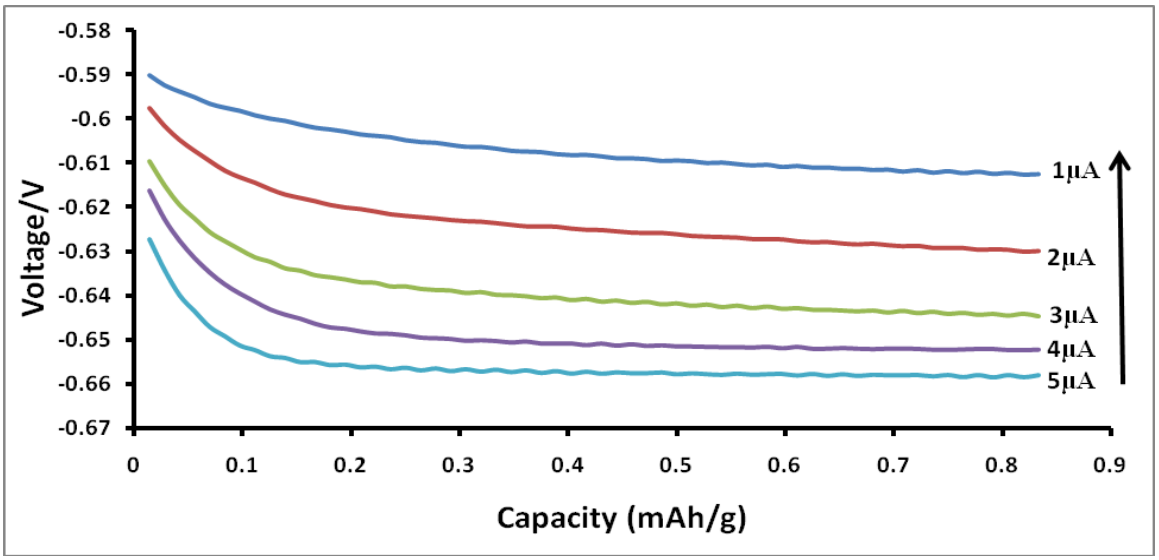

Figure 4.22: Voltage profiles depicting the effect of applied discharge current using GCE-MWCNT-CuO. The single headed arrow is meant to shows the direction of the voltage decrease.

4.3.5.4.4 Discharge capacity studies

Controlled potential electrolysis was employed to investigate the effect of cycle number on the capacity of the working material for hydrogen. It is of interest to retain a large hydrogen capacity for a longer cycle life. Therefore, materials that do not easily lose capacity are required. In controlled potential electrolysis, a

potential obtained from chronopotentiometry is applied and the discharge capacity of a material is obtained from the discharge current and time.

The above CPE information is summarized in figure 4.23, which also shows a resemblance in the behavior of GCE-MWCNT and GCE-MWCNT-CuO. The discharge voltages of GCE-CuO, and GCE-MWCNT-CuO as obtained in chronopotentiometry (*applied current of 1 μA*) are – 0.716 V and – 0.609 V respectively. These discharge voltages were applied in the following CPE studies. GCE-CuO shows a high hydrogen storage capacity but falls sharply at nearly cycle number twenty (20) compared to GCE-MWCNT and GCE-MWCNT-CuO which maintain a constant capacity at the same cycle number.

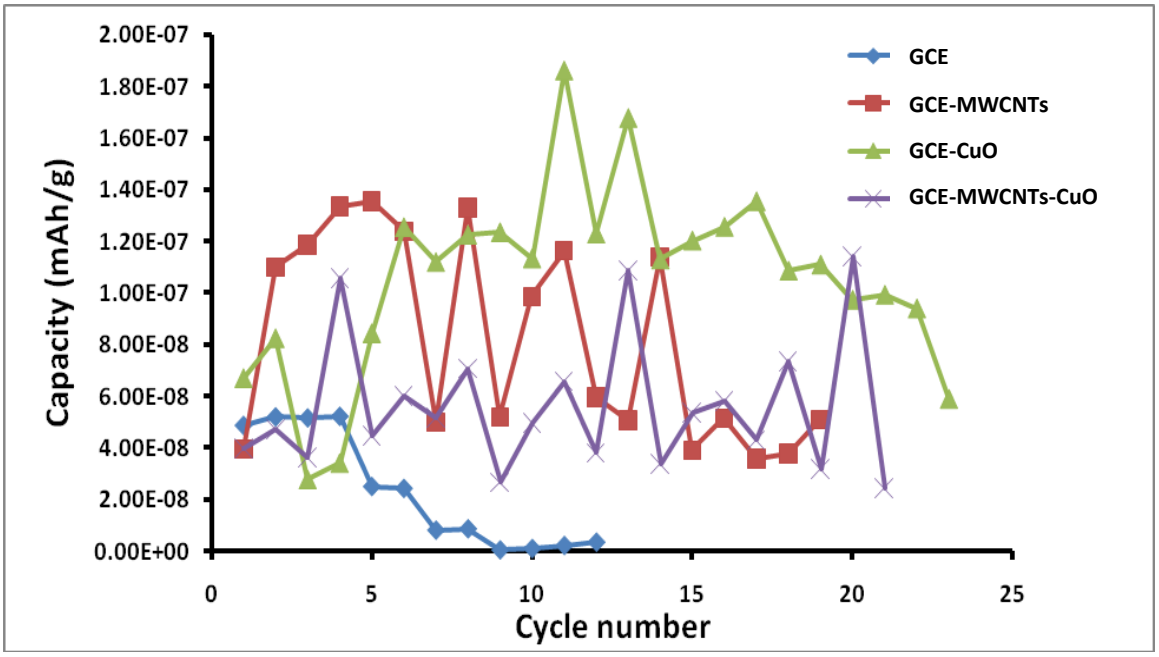

Figure 4.23: The plot comparing the discharge capacity behavior of GCE, GCE-MWCNT, GCE-CuO and GCE-MWCNT-CuO as a function of cycle number.

The bare GCE easily lose capacity and falls sharply to zero capacity, after which it shows signs of regaining capacity, possibly due to electrode cleaning effect as the scan number increases.

The bar graph in figure 4.24 clearly shows the discharge capacities of different materials modified on glassy carbon electrode. As can be seen both the GCE and GCE-MWCNT electrodes attain their maximum capacities at the same cycle number of 5. The GCE-MWCNT-CuO electrode shows a small discharge capacity compared to both GCE-MWCNT and GCE-CuO electrodes. These results are consistent with the charge profile results where GCE-CuO was charged to a high voltage. This may be due to the CuO blocking the pores/caps of the MWCNTs, preventing the adsorption of hydrogen.

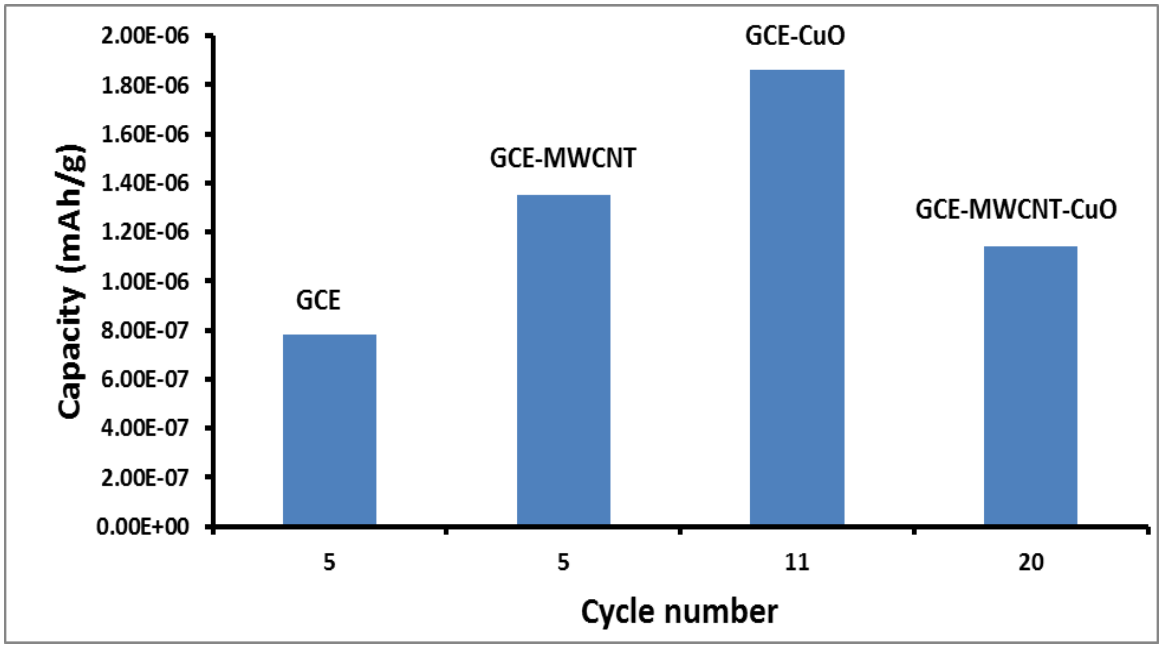

Figure 4.24: The bar graph clearly showing the discharge capacities for modified glassy carbon electrode.

4.3.5.5 Effect of the Cu decorated MWCNTs

Copper nanoparticles synthesized by reduction with sodium borohydride are mainly cubic in shape. Nanoparticles are known for their high surface area and their high respond to applied potential in electrochemistry (especially copper and nickel nanoparticles). The size and shape of nanoparticles is controlled during

their synthesis by the rate of the drop of sodium borohydride and the stirring rate. It is of interest to synthesize nanoparticles of a desired size to avoid blockage of the MWCNTs caps during modification, since this caps plays a major role in hydrogen being stored in the inside of the MWCNTs [56].

4.3.5.5.1 Cyclic voltammetry analysis at the GCE-MWCNT-Cu electrode

The GCE-Cu shows two cathodic peaks possibly due to the reduction of Cu^{2+} to Cu^{+} and to electron rich Cu^{0} as shown in figure 4.25 **(c)**. No cathodic peak is observed for GCE-MWCNT-Cu, but only the anodic peak. Similar results were reported by Reinaldo *et al*. [57], during studies of electrochemical activity of copper nanoparticles in DMF binder. They found two anodic current plateaus, associating the first with the electro-oxidation of Cu to Cu (I) and further oxidation to Cu (II). They derived the reaction scheme as follows:

$$2Cu + H_2O \longleftrightarrow Cu_2O + 2H^+ + 2e^- \qquad \textbf{(Scheme 4.2)}$$

$$Cu_2O + H_2O \longleftrightarrow 2CuO + 2H^+ + 2e^- \qquad \textbf{(Scheme 4.3)}$$

The GCE-MWCNT electrode was observed to continue showing its redox activity by showing two broad anodic peaks.

A sharp anodic peak is observed in both GCE-Cu and GCE-MWCNT-Cu at a potential of nearly -0.5 V (vs. Ag/AgCl) as depicted in figure 4.25, which is consistence with the theory [56]. No significant synergistic effect is seen for MWCNTs and Cu, except for the fact that the peak becomes more sharp and long in size and also the peak at a potential of nearly -0.27 V (vs. Ag/AgCl) disappears. The successful decoration of Cu nanoparticles on the surface of the

MWCNTs was verified by TEM (refer to TEM images in figure 4.2) and SEM (see SEM images in figure 4.7) micrographs.

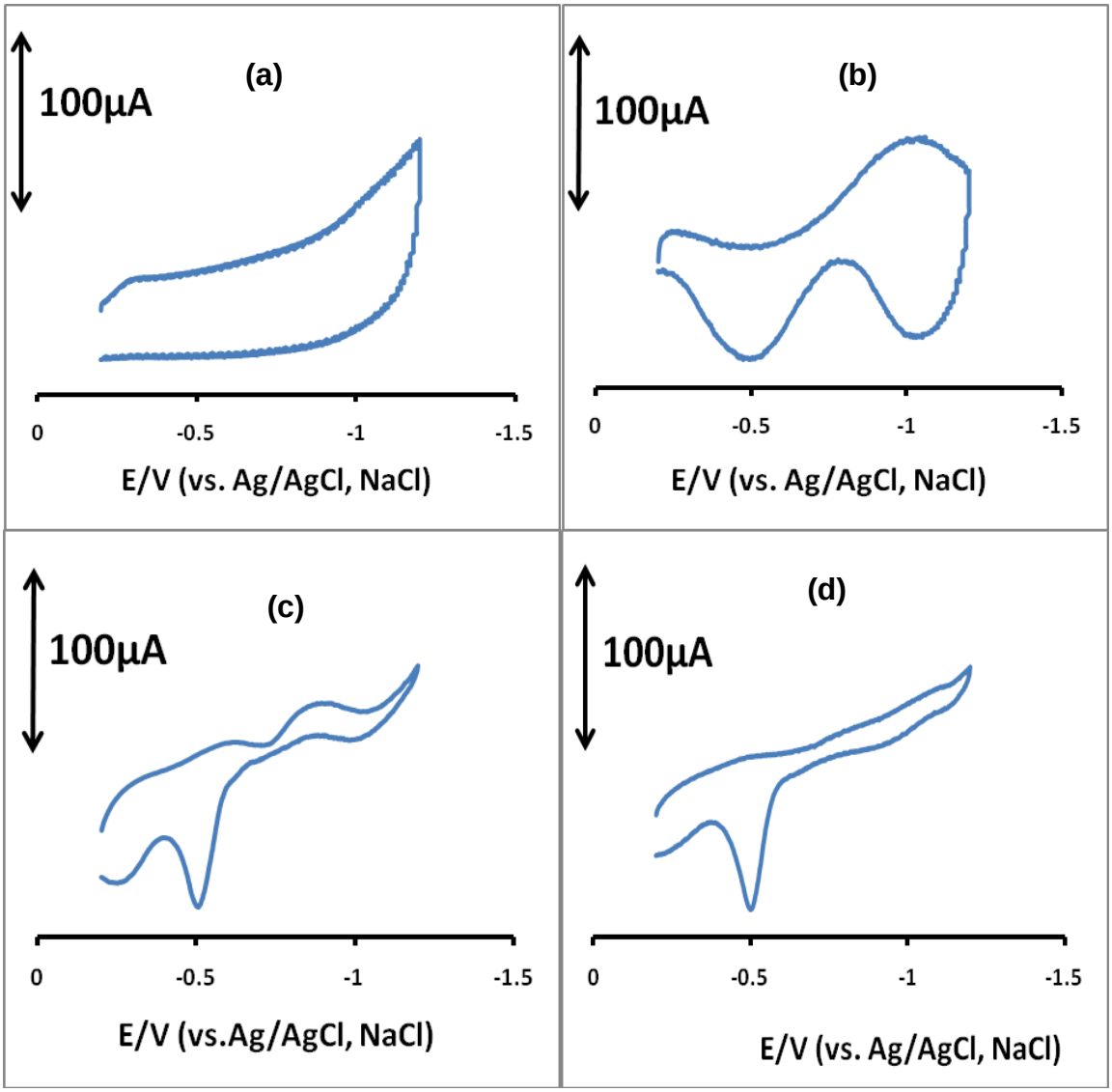

Figure 4.25: Cyclic voltammetric profiles of **(a)** GCE, **(b)** GCE-MWCNT, **(c)** GCE-Cu and **(d)** GCE-MWCNT-Cu at a scan rate of 50 mV/s.

4.3.5.5.2 Effect of the CV scan number on the current response using the GCE-MWCNT-Cu electrode

The effect of scan number is one of the important factors that need to be investigated. From figure 4.26, it can be seen that as the scan number increases, the anodic peak shift to a less negative current. The separation of the second anodic peak (broad one) also increases as compared to the first anodic peak. Therefore it can be observed that as the scan number increases the anodic peak current shift to a more positive potential and tend to decrease the anodic current. At the same instances the cathodic peak current tends to decrease shifting the peak to a more negative potential. It is therefore suggested that the electro-catalytic activity of the GCE-MWCNT-Cu electrode on the current response is influenced by the scan number [58]. From figure 4.26 **(a)** it is evident that as the scan number increases, the GCE-MWCNT-Cu electrode gets passivated as seen by a decrease in anodic current response [58].

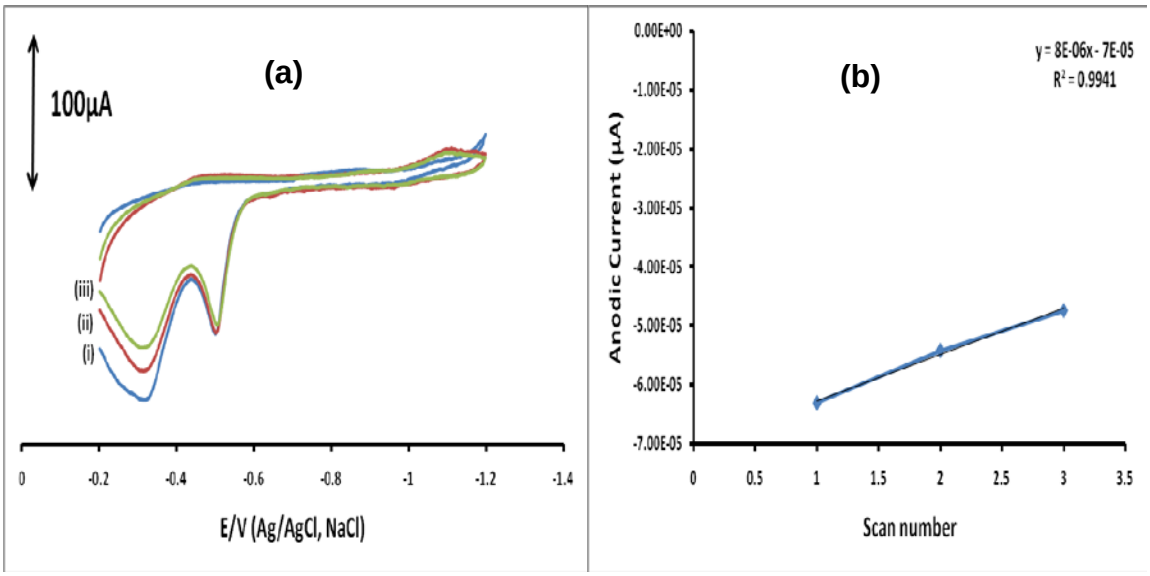

Figure 4.26: (a) The CV profiles showing the effect of the scan number on both the anodic and cathodic peak current using GCE-MWCNT-Cu at a scan rate of 10 mV/s and **(b)** plot of anodic current against scan number.

4.3.5.5.3 Charge-discharge voltage studies

As shown in figure 4.27, the charge-discharge cycle affect both the discharge and charge voltages. Figure 4.27 **(a)** shows that as the charge cycle increases, the GCE-Cu tend to be charged to a high voltage and also figure 4.27 **(b)** shows that the discharging voltage tend to increase as the discharge cycle increases. Similar results were reported by Seung *et al*. [59]. They observed that repetitive charge-discharge cycle tend to cause the activation process of the GCE-Cu working electrode as seen by an increase in charge-discharge voltages until the saturation of the charge-discharge storage capacity is reached [59].

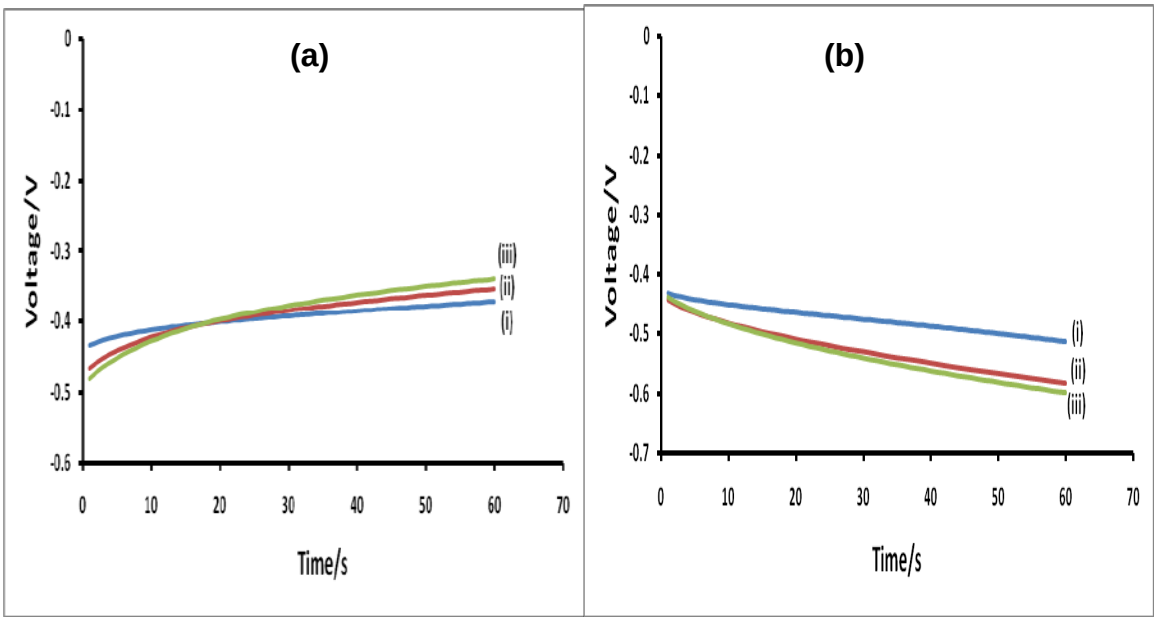

Figure 4.27: Voltage profiles of GCE-Cu depicting the effect of multi-running using GCE-Cu for both **(a)** charging (i) 1st, (ii) 2nd and (iii) 3rd scans and **(b)** discharging processes at **(i)** 1st, (ii) 2nd and (iii) 3rd scans.

4.3.5.5.4 Comparative discharge capacity studies

Figure 4.28 clearly shows the synergistic effect (combined power) between GCE-MWCNTs and GCE-Cu. The discharge voltages of GCE-Cu, and GCE-MWCNT-Cu as obtained in chronopotentiometry (*applied current of 1 μA*) are – 0.600 V and – 0.670 V respectively .As expected, GCE-MWCNT-Cu shows highest hydrogen storage capacity due to its high surface area and catalytic activity has improved due to presence of MWCNTs and Cu nanoparticles respectively. Therefore, the increase in the hydrogen storage capacity is in the order: GCE < GCE-MWCNT < GCE-Cu < GCE-MWCNT-Cu.

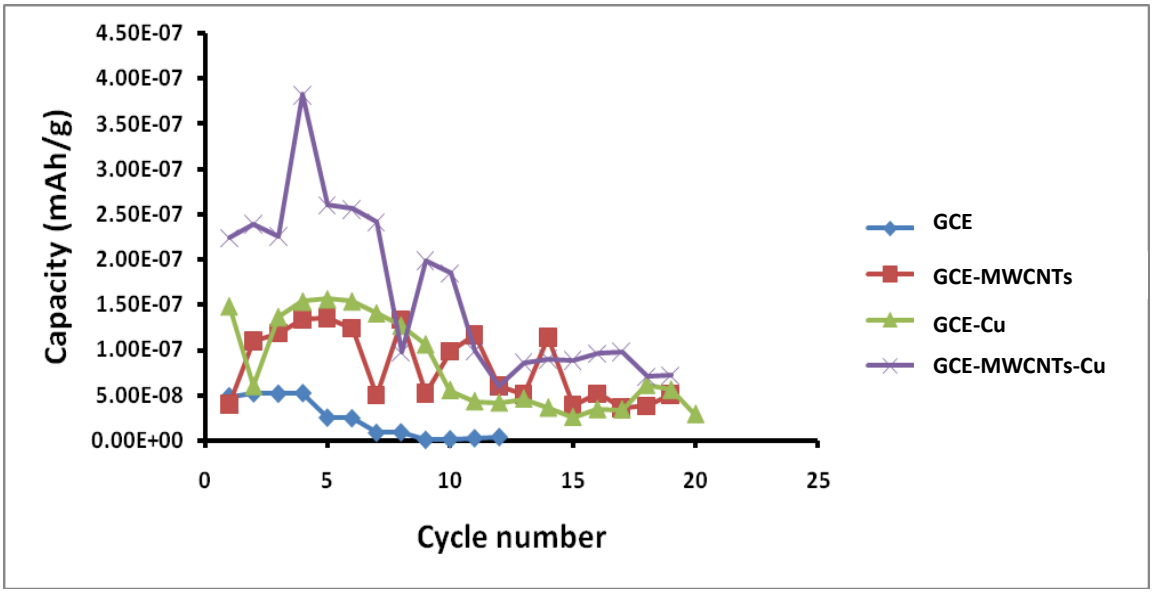

Figure 4.28: The plots of discharge capacity against cycle number for GCE, GCE-MWCNT, GCE-Cu and GCE-MWCNT-Cu.

Note that as the cycle number increases, the capacity of GCE-Cu falls below that of GCE-MWCNT. GCE-MWCNT-Cu has a maximum capacity of approximately 0.383 nAh/g at cycle number 4 compared to 0.041 nAh/g of GCE (excess of 0.342 nAh/g by GCE-MWCNT-Cu) at the same cycle number.

The bar graph is figure 4.29 below shows the synergistic effect between the GCE-MWCNT and GCE-Cu. It is interesting to note that the discharge capacity of the GCE-Cu electrode is higher than that of the GCE-MWCNT electrode. The GCE-MWCNT-Cu electrode doubles the capacity for the GCE-Cu electrode indicating the combined power of the copper nanoparticles and the carbon nanotubes. The maximum capacities are obtained at the same cycle number for all the electrodes except the GCE-MWCNT-Cu electrode.

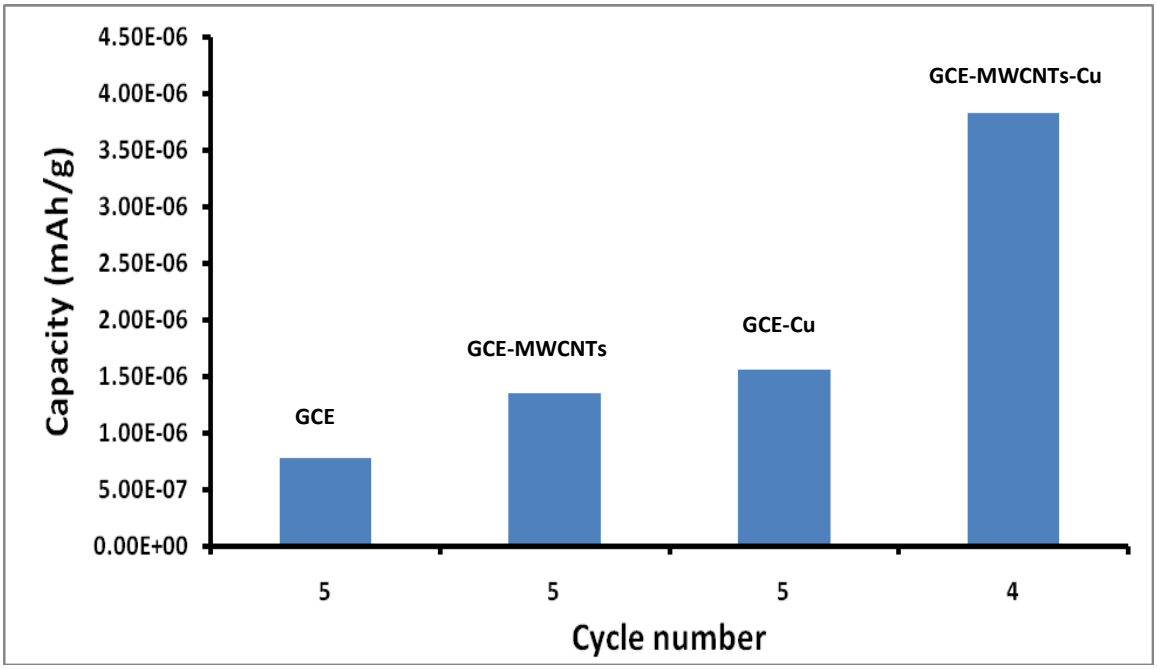

Figure 4.29: The bar graph clearly showing the discharge capacities of a modified glassy carbon electrodes.

4.3.5.6 Effect of the Fe decorated MWCNTs

Iron is a metallic chemical element with atomic number 26. Iron and iron alloys are by far the most common metals and they forms compound mainly in the +2 and +3 oxidation state. Traditionally, iron (II) compounds are called ferrous, and iron (III) compounds are called ferric. Industrially, iron is produced from iron ores,

principally hematite (Fe_2O_3) and magnetite (Fe_3O_4). Iron has a low cost and high strength [60, 61]. The current high interest in iron/iron oxide nanoparticles applications can be partly attributed to their presumed ease of injection and faster reactivity. Under environmental conditions, nanoparticles with Fe(0) cores persist because they are passivated by a shell of oxides. Iron oxides are chemical compound composed of iron and oxygen. Iron (III) oxide (Fe_2O_3, hermatite) is a common form of iron with a reddish brown color and was the one used in this dissertation [62].

The MWCNTs used throughout the experiment were prepared from iron (II) pthalocyanine (Sigma-Aldrich, 90% assay). As expected, iron nanoparticles are one of the impurities with amorphous carbon and carbon nanoparticles. From the previous report, the current response, charge and discharge voltages and the discharge capacities of the as-prepared and purified MWCNTs were investigated, and the as-prepared MWCNTs outperformed the purified MWCNTs. This indicates that the iron nanoparticles play a role in enhancing the electrochemical activity of the MWCNTs for hydrogen storage [63].

Despite huge literature for hydrogen storage in CNTs, little has been studied on the electrochemical activity of iron nanoparticles decorated CNTs for hydrogen storage as compared to the nickel nanoparticles and nickel oxides decorated CNTs [64]. Iron and silver nanoparticles are mainly used as cleaning agents for contaminated ground water and site remediation. They are able to degrade the chlorinated compound found in water to harmless products as it was proven in previous research report. In this report, the objective is to investigate the electrochemical activity of MWCNTs decorated with iron nanoparticles and its oxides for hydrogen storage. The glassy carbon (0.07 cm^2) was used as a support for the MWCNTs-M (M = Fe or Fe_2O_3) hybrid due to its low cost, chemical inertness and wide potential window which are advantages over the precious metal electrodes such as gold.

4.3.5.6.1 Cyclic voltammetric response at the GCE-MWCNT-Fe electrode

The cyclic voltammetric responses of the GCE-Fe and GCE-MWCNT-Fe electrodes at a scan rate of 100 mV/s are compared in figure 4.30. As can be seen, the GCE-Fe electrode shows a high current response compared to the GCE-CNT-Fe electrode. The presence of the MWCNTs tends to decrease the current response as compared to its absence which increases the current response. In this case, the MWCNTs do not efficiently serve as the conducting carbon material between the metal nanoparticles and the glassy carbon electrode. TEM (see TEM images in figure 4.3) and SEM (see SEM images in figure 4.8) clearly showed Fe nanoparticles well coated on the surface of the oxidized MWCNTs, justifying that the method employed for decoration of MWCNTs with metal nanoparticles and metal oxides was efficient.

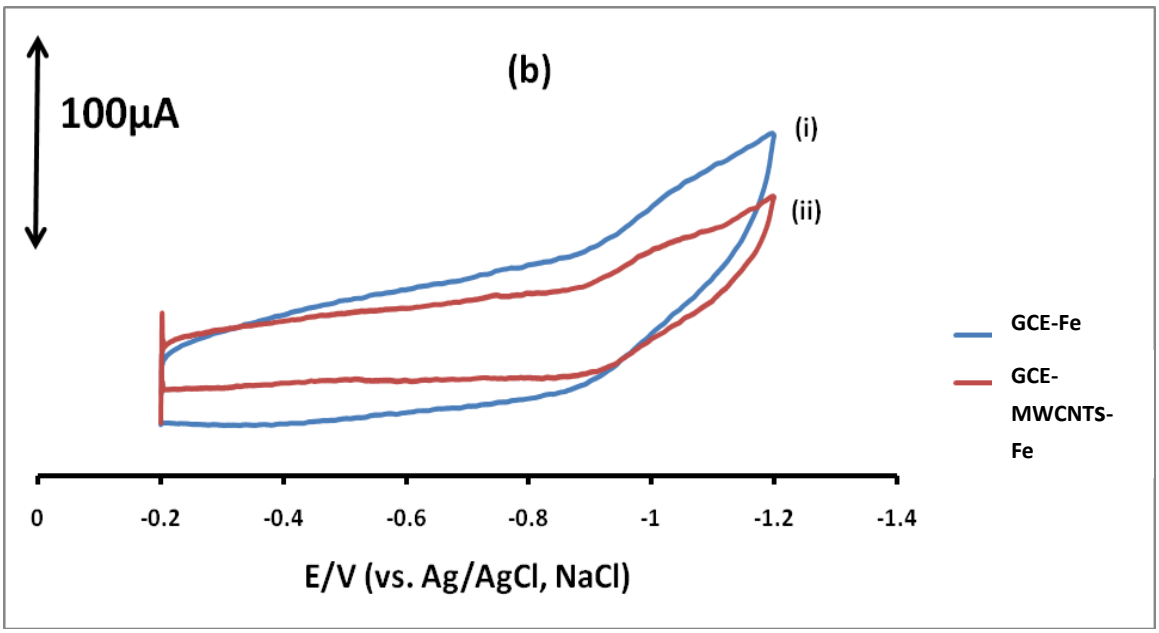

Figure 4.30: Cyclic voltammetric profiles comparing the current density for the **(i)** GCE-Fe and the **(ii)** GCE-MWCNT-Fe electrodes at a scan rates of 100 mV/s.

4.3.5.6.2 Controlled potential electrolysis studies

The discharge capacities as a function of cycle number for various glassy carbon modified electrode are shown in figure 4.31. The discharge voltages of GCE-Fe, and GCE-MWCNT-Fe as obtained in chronopotentiometry (*applied current of 1 μA*) was – 0.899 V for both electrodes. As can be seen, the GCE-MWCNT electrode shows a high discharge capacity for hydrogen followed by the GCE-MWCNT-Fe electrode. A sharp fall in discharge capacity for the bare GCE is observed. The GCE-Fe electrode shows a low discharge capacity but tend to have a long cycle life. A short cycle life is seen for the GCE-MWCNT-Fe electrode, living up to 11th cycle number.

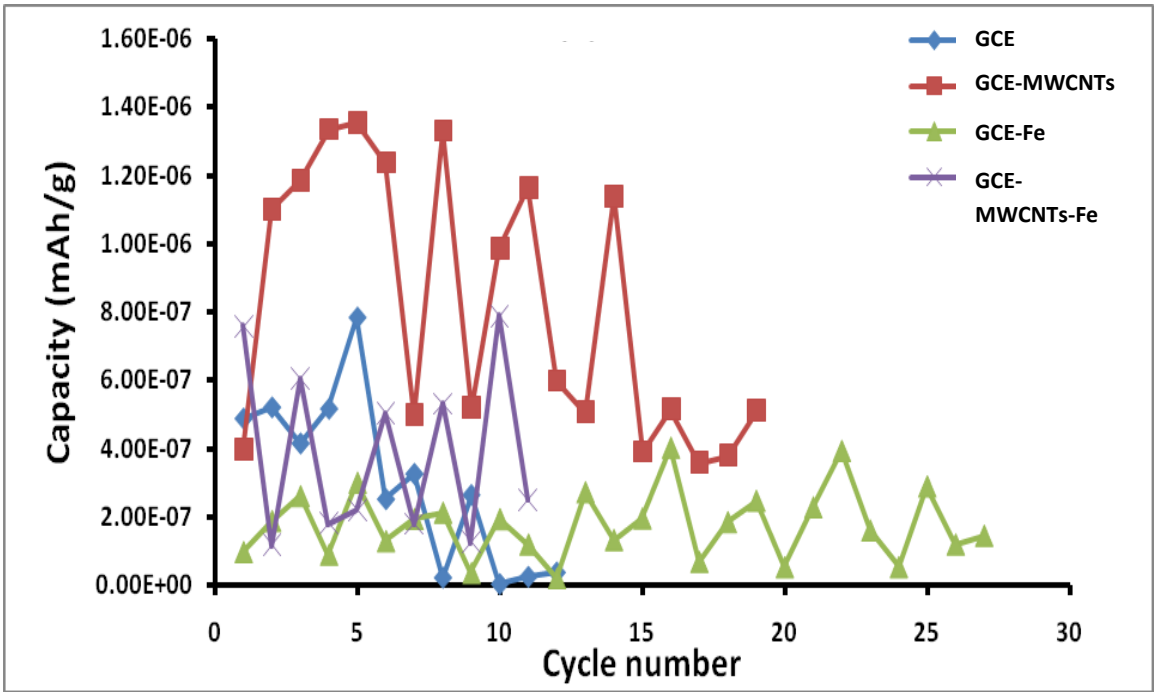

Figure 4.31: The plots of discharge capacity against cycle number for GCE, GCE-MWCNT, GCE-Fe and GCE-MWCNT-Fe.

Figure 4.32 is the bar graph clearly showing the maximum discharge capacity for the bare GCE, GCE-MWCNT, GCE-Fe and the GCE-MWCNT-Fe electrodes. It

can be clearly seen that the GCE-MWCNT electrode have the highest discharge capacity followed by the GCE-MWCNT-Fe and bare GCE respectively, with the lowest discharge capacity attained by the GCE-Fe electrode. Note that as MWCNTs are integrated with Fe nanoparticles, the discharge capacity tend to be lower than that of the GCE-MWCNTs but higher than of the GCE-Fe electrode, this is an indication that MWCNTs have a high electrochemical activity that the Fe nanoparticles for hydrogen storage. This suggests that, iron nanoparticles are not an active catalyst to electrochemically catalyze the hydrogenation reaction in MWCNTs. The high discharge capacity for the GCE-MWCNT-Fe electrode is in contrast with the CV and CD studies where a low current respond and low charge voltage was attained by the GCE-MWCNT-Fe as compared to the GCE-Fe electrode.

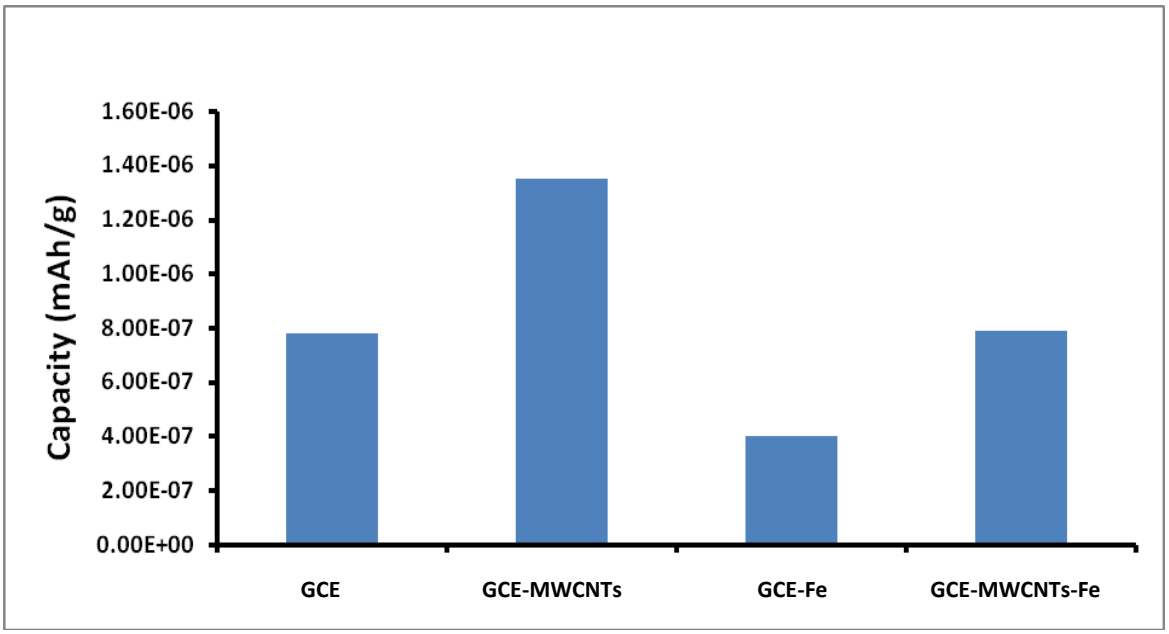

Figure 4.32: The bar graph clearly showing the maximum discharge capacities of the specified electrodes.

4.3.5.7 Effect of the Fe_2O_3 decorated MWCNTs

4.3.5.7.1 Cyclic voltammetric behaviors at the GCE-MWCNT-Fe_2O_3 hybrid electrode

Cyclic voltammetric profiles for the GCE-MWCNT-Fe_2O_3 at various scan rates are depicted in figure 4.33. A broad anodic peak was reproducible at scan rates of 10 mV/s, 50 mV/s and 100 mV/s at a potential of about -0.7 V vs. Ag/AgCl reference electrode. Such peaks tend to be absence at a high scan rate of 150 mV/s. It can be seen that as the scan rate was increased, the cyclic voltammograms become rectangular in shape, typical of a high energy and power density supercapacitors. More redox waves can be seen at a scan rate of 50 mV/s, indicating a reduction of Fe^{3+} to Fe^{2+} and to Fe^{+} and finally to Fe^{0} (a zero-valent iron). During oxidation process, the same mechanism take place with the Fe^{0} starting to lose electrons to form Fe^{+} which also tend to lose electrons to form Fe^{2+} and finally Fe^{3+}.

As expected, figure 4.33 **(b)** shows that as the scan number is increased the anodic peak at a potential of approximately -0.7 V tend to shift to a more positive current and less negative potential. Note that as the scan rate is increased, the current response tend to be great, as shown by the current full scale being 1 mA from a scan rate of 50 mV/s to 150 mV/s. The featureless CV's with no faradic peaks is observed in figure 4.33 **(d)**. From figure 4.33 **(a)**, it is notable that even at a low scan rate of 10 mV/s, the CV was more or less rectangular in shape. The rectangular shaped CV over a wide range of scan rates is the ultimate goal in electrochemical double-layer capacitors which have a high energy (duration at which the strength of the given current and voltage combination can be applied) and power density (strength of the current and voltage combination). Therefore, these findings suggest a possible application of GCE-MWCNT-Fe_2O_3 electrode in supercapacitors. These results are consistent with the literature whereby it is

said that the main classes of supercapacitors are metal oxides, electronically conducting polymers and carbon-based supercapacitors [42]. The GCE-MWCNT-Fe_2O_3 is an example of a hybrid supercapacitor which can attract great attention to researchers. These CV results are consistent with the TEM (see TEM images in figure 4.3) and SEM (see SEM images in figure 4.8) images which showed Fe_2O_3 well decorated on the surface of the MWCNTs.

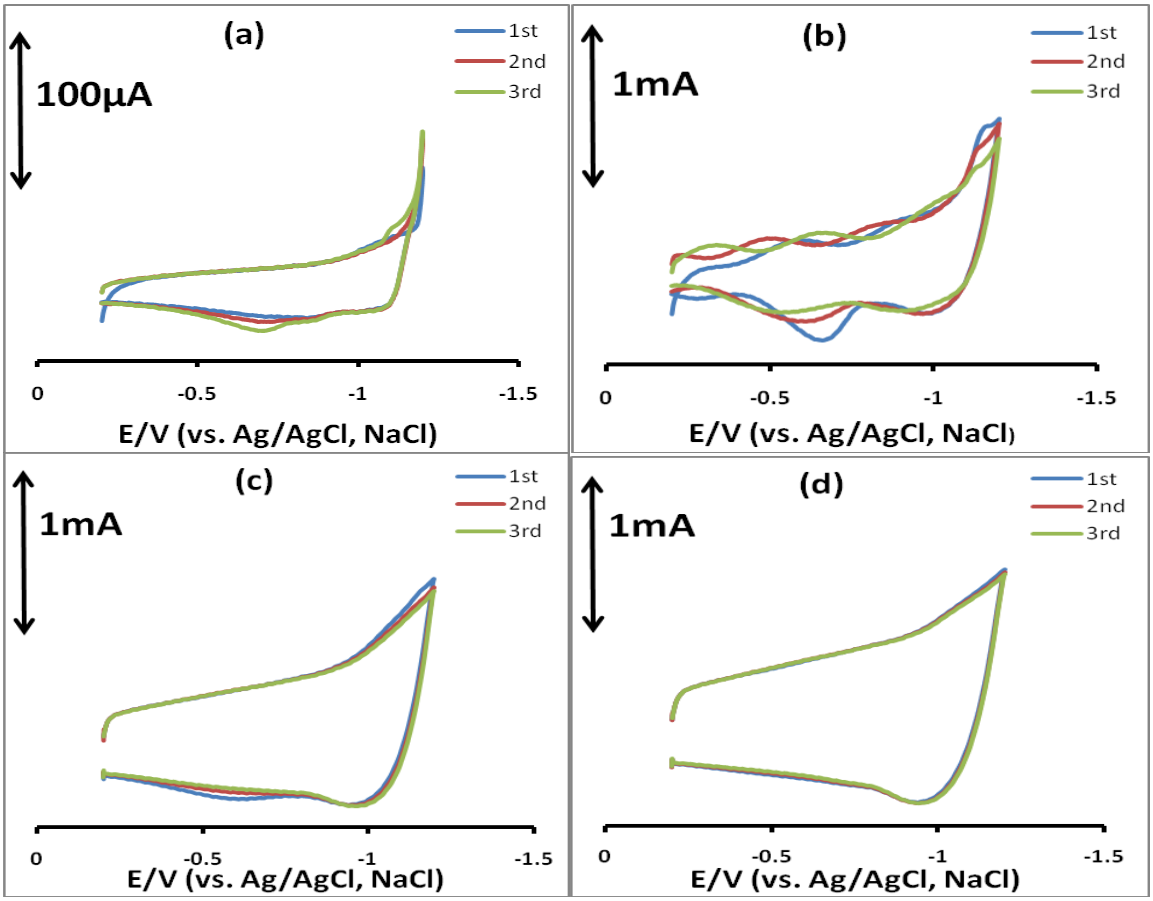

Figure 4.33: Cyclic voltammetric profiles for the GCE-MWCNT-Fe_2O_3 electrode depicting the effect of scanning the potential at a scan rate of **(a)** 10 mV/s, **(b)** 50 mV/s, **(c)** 100 mV/s and **(d)** 150 mV/s on the shape of the cyclic voltammogram.

4.3.5.7.2 Controlled potential electrolysis profiles of the Fe_2O_3 decorated MWCNTs

The GCE-Fe_2O_3 electrode shows the highest discharge capacity than the GCE, GCE-MWCNT and GCE-MWCNT-Fe_2O_3 electrodes as shown in figure 4.34 **(a)**. The discharge voltages of GCE-Fe_2O_3, and GCE-MWCNT-Fe_2O_3 as obtained in chronopotentiometry (*applied current of 1 μA*) are – 0.900 V and – 0.500 V respectively. The maximum capacity for the GCE-MWCNT-Fe_2O_3 electrode is even lower than for the bare GCE. The bare GCE, GCE-Fe_2O_3 and the GCE-MWCNT-Fe_2O_3 electrodes have equal cycle life of 12, whereas the GCE-MWCNT shows a long cycle life living up to 19^{th} cycle number.

The bar graph in figure 4.34 **(b)** clearly shows the maximum capacity attained by each electrode. The increase in the discharge capacity followed the order: GCE-MWCNT-Fe_2O_3 < GCE < GCE-MWCNT < GCE-Fe_2O_3. The discharge capacity of the GCE-Fe_2O_3 is higher than of the GCE-Fe electrode. It can be seen that the GCE-Fe_2O_3 gave a high discharge capacity than the GCE-MWCNT electrode in contrast to the GCE-Fe electrode. As Fe_2O_3 are added to the MWCNTs materials, the discharge capacity tends to decrease. In this case it is obvious that the MWCNTs are not playing their role for hydrogen storage. The low discharge capacity for the GCE-MWCNT-Fe_2O_3 electrode was consistent with the CP studies where a low charge and discharge voltages were attained. Contradiction was observed with the CV studies where the GCE-MWCNT-Fe_2O_3 electrode gave a high current response than the GCE-Fe_2O_3 electrode.

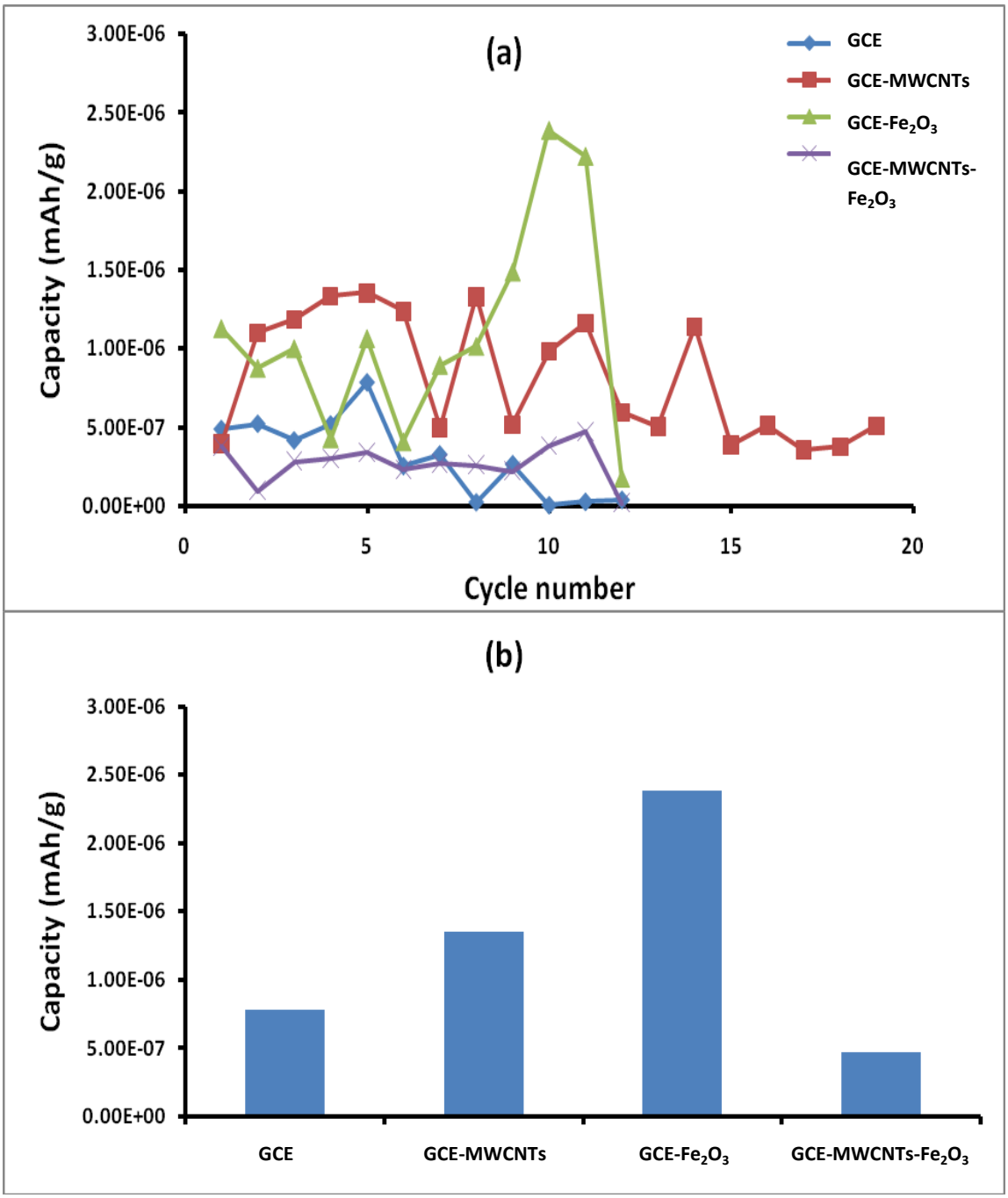

Figure 4.34: (a) The discharge capacities for different glassy carbon modified electrodes as a function of cycle number. **(b)** Bar graph clearly showing the maximum discharge capacities attained by electrodes.

4.3.5.8 Effect of NiO decorated MWCNTs

Nanosized materials, such as metal oxides and metal nanoparticles have attracted much attention recently because of their unusual chemical and physical properties which are different from those of bulk materials. Nickel is a chemical element with atomic number 28 [65-67]. It is a silvery white lustrous metal. The nickel metal is corrosion resistant, finding many uses in alloys and as a catalyst for hydrogenation. Nickel foam and nickel mesh are used in gas diffusion electrodes for alkaline fuel cells [68, 69].

Nickel (II) oxide is a chemical compound with formula NiO. It is notable as being the only well characterized oxides of nickel (although nickel (III) oxide, Ni_2O_3 and NiO_2 have well-being claimed). NiO can be prepared by multiple methods, upon heating above 400 ^oC, nickel powder react with oxygen to give NiO [70, 71]. The simplest and most successful method of preparation is through pyrolysis of nickel (II) compounds such as nitrate and hydroxides. Recently, NiO was used to make the NiCd rechargeable batteries found in many electronic devices [72-75]. NiO is also a versatile hydrogenation catalyst [76]. Nanosized nickel oxides, NiO, are widely used in many technological applications because they exhibit particular catalytic, analogous electronic and magnetic properties [77]. Another important application of NiO is in a battery system [78-80]. Non-stoichiometric nickel oxide is a good P-type semiconductor owing to its defect structure and it is also a potential gas sensor for H_2. These applications can be enhanced by decreasing the particle size, preferably to less than 10 nm [81, 82]. All electrolysis reaction studies discussed under this section were undertaken at 24 ^oC.

4.3.5.8.1 Cyclic voltammetric response at the GCE-MWCNT-NiO hybrid electrode

Figure 4.35 compares the CV profiles of bare GCE, GCE-MWCNT, GCE-NiO and GCE-MWCNT-NiO electrodes. It can be seen that the GCE-MWCNT outperform the bare GCE electrode due to its high conductivity, high surface area and pore structures. These characteristics make MWCNTs good materials for hydrogen storage. Figure 4.35 also indicate the good conductive behavior of MWCNT. Two broad anodic peaks are observed compared to other materials. This may be caused by the fact that MWCNTs may act as a mix of metallic, semiconducting and insulating materials, depending on the chirality of the tubes, i.e. geometry or arrangements of the tube structures.

A small cathodic peak is observed for GCE-NiO and anodic peak for GCE-MWCNT-NiO. This shows an increase in electron transfer kinetic rate due to the presence of nickel oxide which promotes the multiple redox reactions. This will in turn increase the hydrogen storage capacity. More cathodic current is seen for GCE-MWCNT-NiO compared to GCE-NiO which shows a good oxidation behavior and confirms a synergy between NiO and MWCNTs. Successful modification of MWCNTs with NiO was clearly confirmed by the SEM images in figure 4.9.

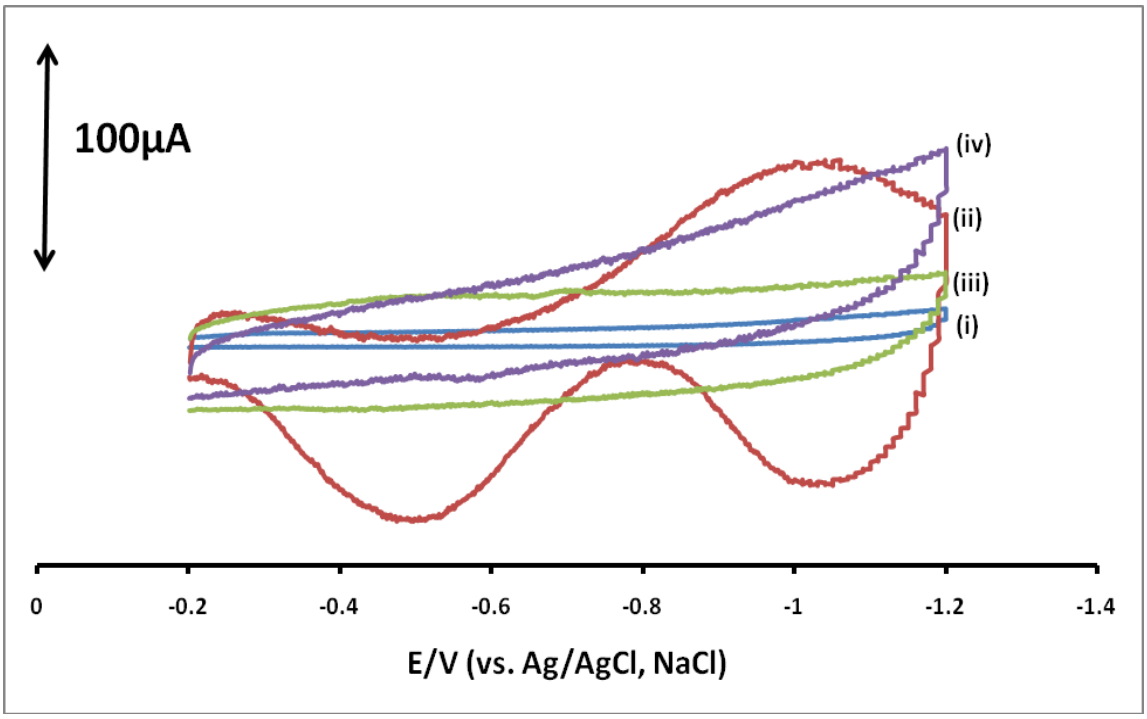

Figure 4.35: Cyclic voltammograms of **(i)** Bare GCE, **(ii)** GCE-MWCNT, **(iii)** GCE-NiO and **(iv)** GCE-MWCNT-NiO electrodes depicting their synergistic effect at a scan rate of 50 mV/s.

4.3.5.8.2 Effect of scan rate on the current response using the GCE-NiO electrode

Figure 4.36 shows the effect of scan rate on the current response using the GCE-NiO electrode. As the scan rate increases more ions tend to diffuse to the electrode surface area resulting in an increase in current respond. Similar results were reported by Swamy *et al*. [83]. As seen below, the voltammogram tend to become more rectangular as the scan rate increases, indicating an increase in energy density. Rectangular-shaped cyclic voltammograms over a wide range of scan rates is the ultimate goal in the electrochemical double-layer capacitors [42]. This behavior is very important for practical applications. The GCE-NiO electrode retains its rectangular shape of CVs up to a high scan rate of 150 mV/s. This

means the charge and discharge processes are very fast at the interface between the GCE-NiO and the electrolyte solution. The rectangular CVs and high speeds of charge and discharge suggest a possible application of GCE-NiO to supercapacitors.

The cathodic peak for GCE-NiO is retained even at higher scan rates with the voltammograms being wider in size which is an indication of more ions diffusing through the electrode. Higher scan rates increases the electron transfer mechanism at the surface of the electrode [83].

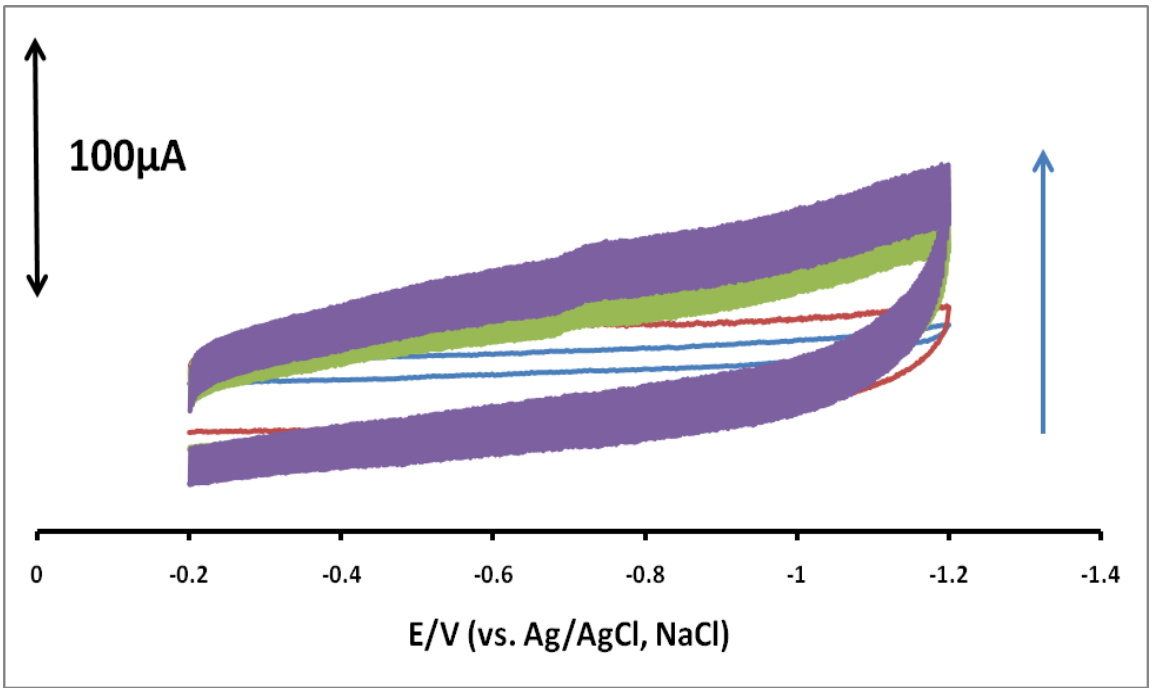

Figure 4.36: Combined CV profiles at 10 mV/s, 50 mV/s, 100 mV/s and 150 mV/s, with an arrow showing an increase in cathodic peak current using GCE-NiO electrode.

Figure 4.37 clearly shows the relationship between current and square root of scan rate. A direct proportion can be seen using GCE-NiO which agrees with the following Ilkovic equation:

$$i_p = 2.69 * 10^5 \, n^{3/2} \, ACD^{1/2} \, v^{1/2}, \qquad \textbf{(Eq. 4.2)}$$

with v representing the scan rate.

This stresses the fact that more ions diffuse to the electrode at higher scan rate due to absence of hindrance on the surface of the electrode. This linear dependence of the reduction peak current on the scan rate showed that the process was diffusion-controlled [83]. The proposed behavior of NiO at the glassy carbon electrode in the presence of the 6 M KOH electrolyte might arise from the diffusion of 6 M KOH at the electrode surface and the interaction between 6 M KOH and NiO [83]. The relationship between square root of the scan rate and cathodic peak current is a good linearity and it is in the range of 10-150 mV/s.

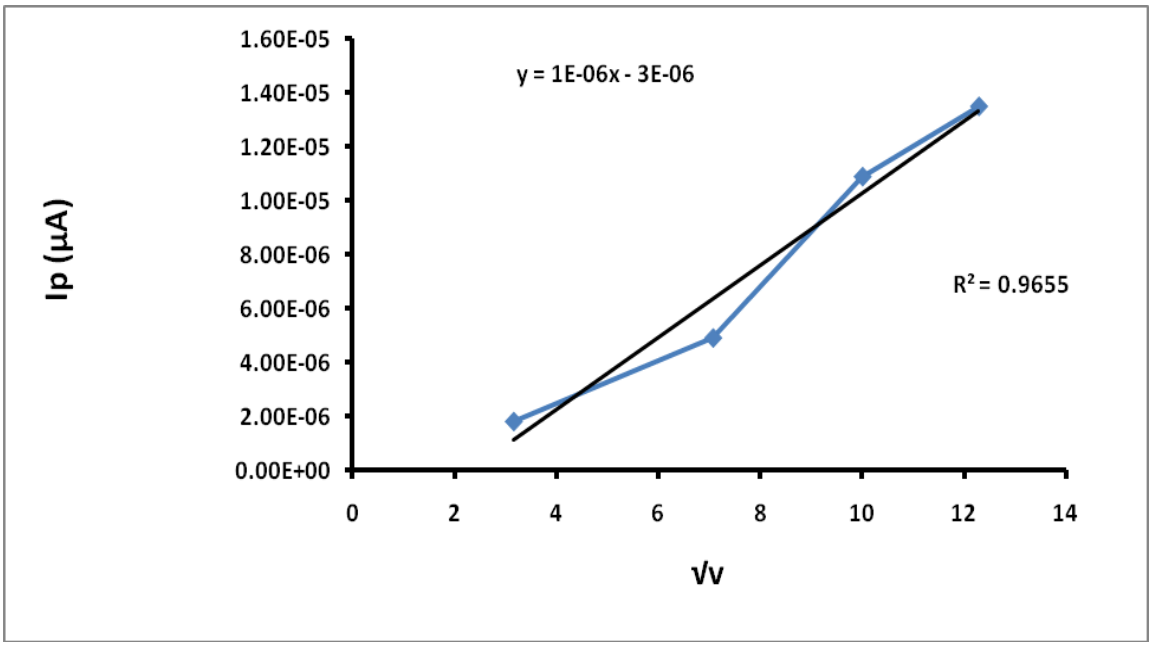

Figure 4.37: A plot of the cathodic peak current against the square root of the scan rate using GCE-NiO electrode.

4.3.5.8.3 Effect of the amount of current applied in chronopotentiometric studies on the charge and discharge voltages

The amount of current applied in chronopotentiometry determines the amount of voltage produced. Figure 4.38 investigate the effect of applied current on the voltage for both charging and discharging processes. It can be seen that as the applied charging current is increased, the voltage tend to decrease compared to an increase in discharge voltage (more negative) as the current increases. From the discharge voltage profile, it can be seen that the polarization was relatively low even for the discharge current of 6 µA [61]. The results obtained emphasize that the adsorption of hydrogen (charging) is promoted by a more negative current, and desorption (discharging) is promoted by a less positive current. In cyclic voltammetry, the reduction (charging) was observed to takes place at a more negative potential while oxidation (discharging) occurs at a more positive potential resulting in an negative current produced to make the redox reaction continuous (i.e. initiate the charging process).

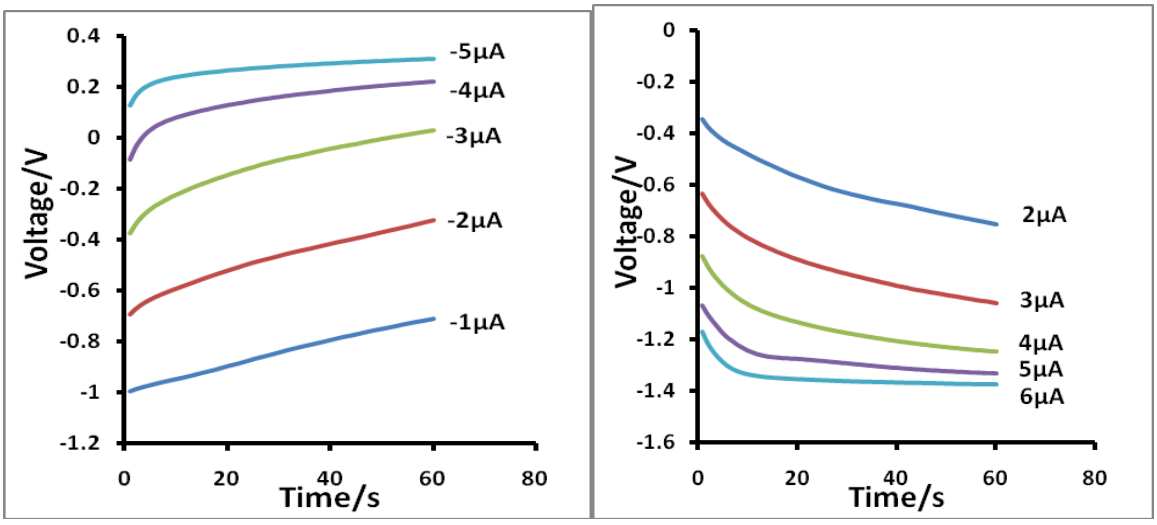

(a) **(b)**

Figure 4.38: Voltage profiles showing the effect of applied **(a)** charge and **(b)** discharge current using GCE-NiO electrode.

4.3.5.8.4 Effect of scan number on the charge-discharge voltage using the GCE-MWCNT-NiO electrode

As the GCE-MWCNT-NiO tends to be charged continuously, the voltage tends to increase as shown in figure 4.39 **(a)**. And also discharge voltage increases as the GCE-MWCNT-NiO is discharged continuously. Repeated charge-discharge cycles results in the activation process of the GCE-MWCNT-NiO working electrode until the saturation point is reached, as depicted in figure 4.39. Similar results were observed by Reinaldo *et al*. [57]. It can be seen that as both the charging and discharging numbers increase, the voltage tend to increase at a low amount compared to initial charging and discharging voltages. This may be due to GCE-MWCNT-NiO electrode losing capacity or being poisoned so as to reach the saturation point. Several slopes are observed in discharge curves, indicating the existence of different adsorption sites.

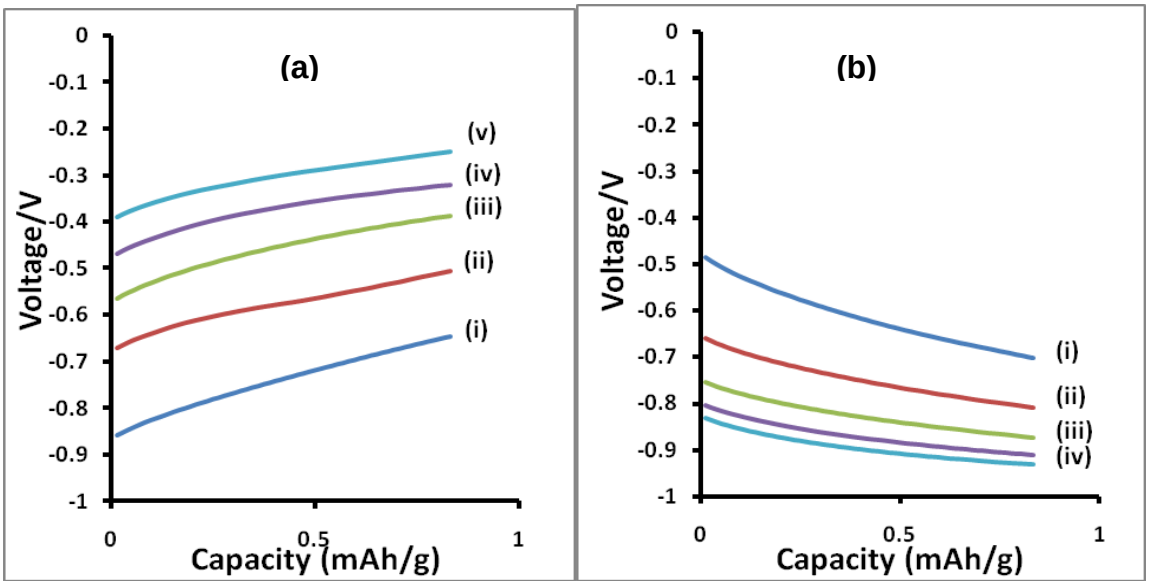

Figure 4.39: Voltage profile showing the effect of **(i)** 1st, **(ii)** 2nd, **(iii)** 3rd, **(iv)** 4th and **(v)** 5th **(a)** Charge and **(b)** Discharge current on the GCE-MWCNT-NiO.

4.3.5.8.5 Discharge capacity studies

Figure 4.40 shows the combined discharge capacity plots, clearly comparing the effect of cycle number on the capacity for **(i)** GCE, **(ii)** GCE-NiO, **(iii)** GCE-MWCNT and **(iv)** GCE-MWCNT-NiO electrodes. The discharge voltages of GCE-NiO, and GCE-MWCNT-NiO as obtained in chronopotentiometry (*applied current of 1 μA*) are – 0.600 V and – 0.809 V respectively. It can be seen that GCE-MWCNT-NiO exhibit high hydrogen storage capacity than the other materials. GCE-NiO gave a high capacity at cycle number 6, but falls sharply until reaching zero at cycle number 17 after which it gains capacity. GCE-MWCNT-NiO shows the best results, but has a short cycle life compared to GCE-MWCNT and GCE-NiO. Electrochemical discharge capacities of both GCE-MWCNT-NiO and GCE-CNT initially increase with cycle number compared to GCE-NiO which shows an initial decrease in capacity. The maximum capacity of GCE-MWCNT-NiO reached at a lower cycle number (5) compared to cycle number 6 of GCE-NiO. This is an indication of the fast kinetics of hydrogen adsorption in these systems.

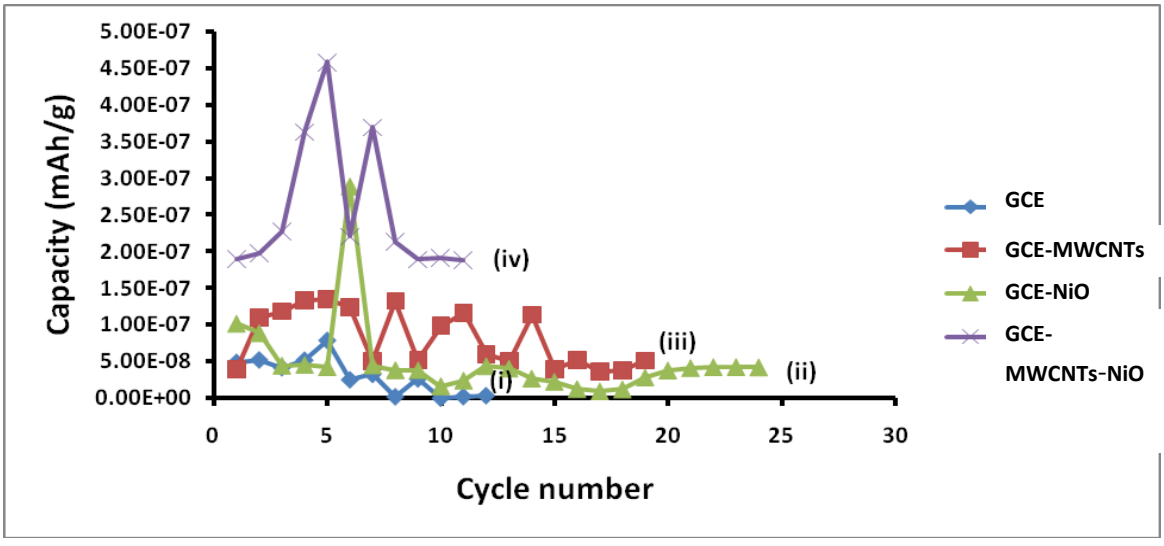

Figure 4.40: A plot of discharging capacity against cycle number showing the synergistic response of both MWCNTs and NiO (**(i)** Bare GCE, **(ii)** GCE-NiO, **(iii)** GCE-MWCNT and **(iv)** GCE-MWCNT-NiO electrodes).

The bar graphs in figure 4.41 clearly shows the synergy between the GCE-NiO and GCE-MWCNT electrode as compared to GCE-CuO and GCE-MWCNT electrodes where no synergy was observed (figure 4.41 **(b)**). This may be due to the small size of the synthesized NiO as compared to CuO (refer to SEM images). It is known that small materials have a high surface area which results in high hydrogen uptake as compared to bulky materials [51]. These discharge capacity studies are consistent with the CV studies where GCE-MWCNTs-NiO electrode gave the highest cathodic current response. It can be seen that the maximum capacities are attained at approximately the same cycle number of 5.

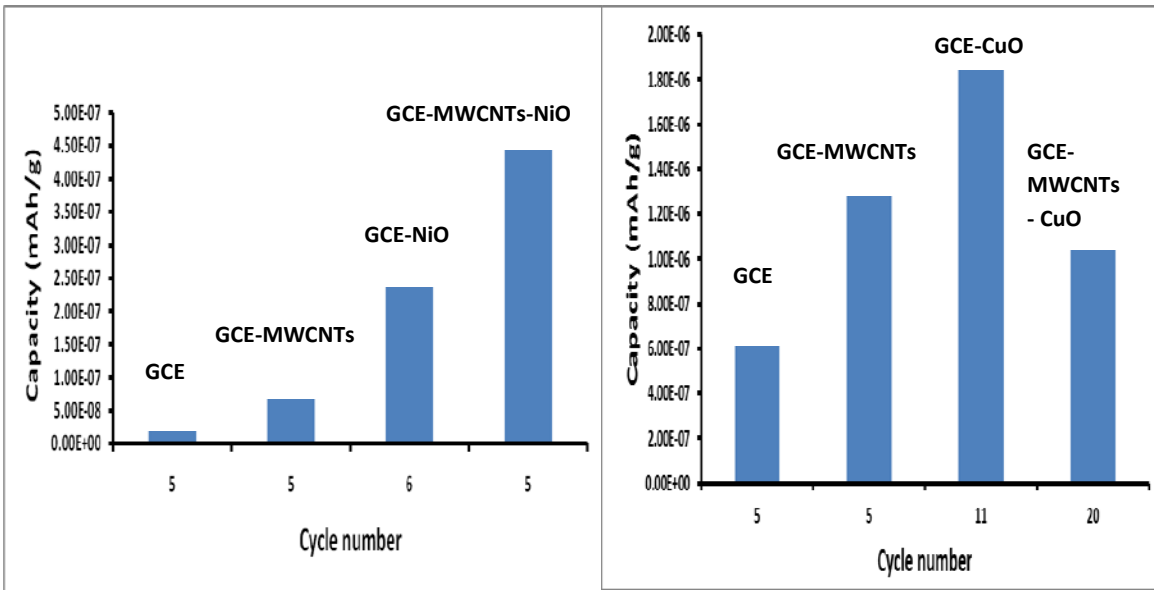

(a) **(b)**

Figure 4.41: (a) The bar graph clearly depicting the synergistic response between MWCNTs and NiO and **(b)** the absence of synergy between MWCNTs and CuO.

4.3.5.9 Effect of the Ni decorated MWCNTs

Herein, the study investigate the effect of Ni decorated CNTs on the current response, charge-discharge voltages and discharge capacity for hydrogen storage. The small sized Ni nanoparticles were clearly seen on the SEM images in figure 4.9.

4.3.5.9.1 Cyclic voltammetric response at the GCE-MWCNT-Ni electrode

Two broad cathodic and anodic peaks are observed for GCE-Ni as shown in figure 4.42 **(c)**. For GCE-MWCNT-Ni the voltammogram becomes rectangular in shape with a sharp cathodic peak at a voltage of -0.69 V. The MWCNTs-Ni hybrid is clearly depicted by SEM (refer to SEM images in figure 4.9) and TEM (see TEM images in figure 4.4). Two small anodic peaks are also retained. The rectangular voltammogram is due to the present of carbon nanotubes in the composite. Similar results were reported by Chien-Te *et al*. [84], where also the Ni-CNT electrode gave the highest current response than the fresh CNTs electrode [84]. As expected, no peaks are observed for bare GCE. Although the mechanism leading to the enhancement of capacitive current are not well understood for the Ni-attached MWCNTs, it is believed that Ni-coated on MWCNTs may very well contribute to it [84].

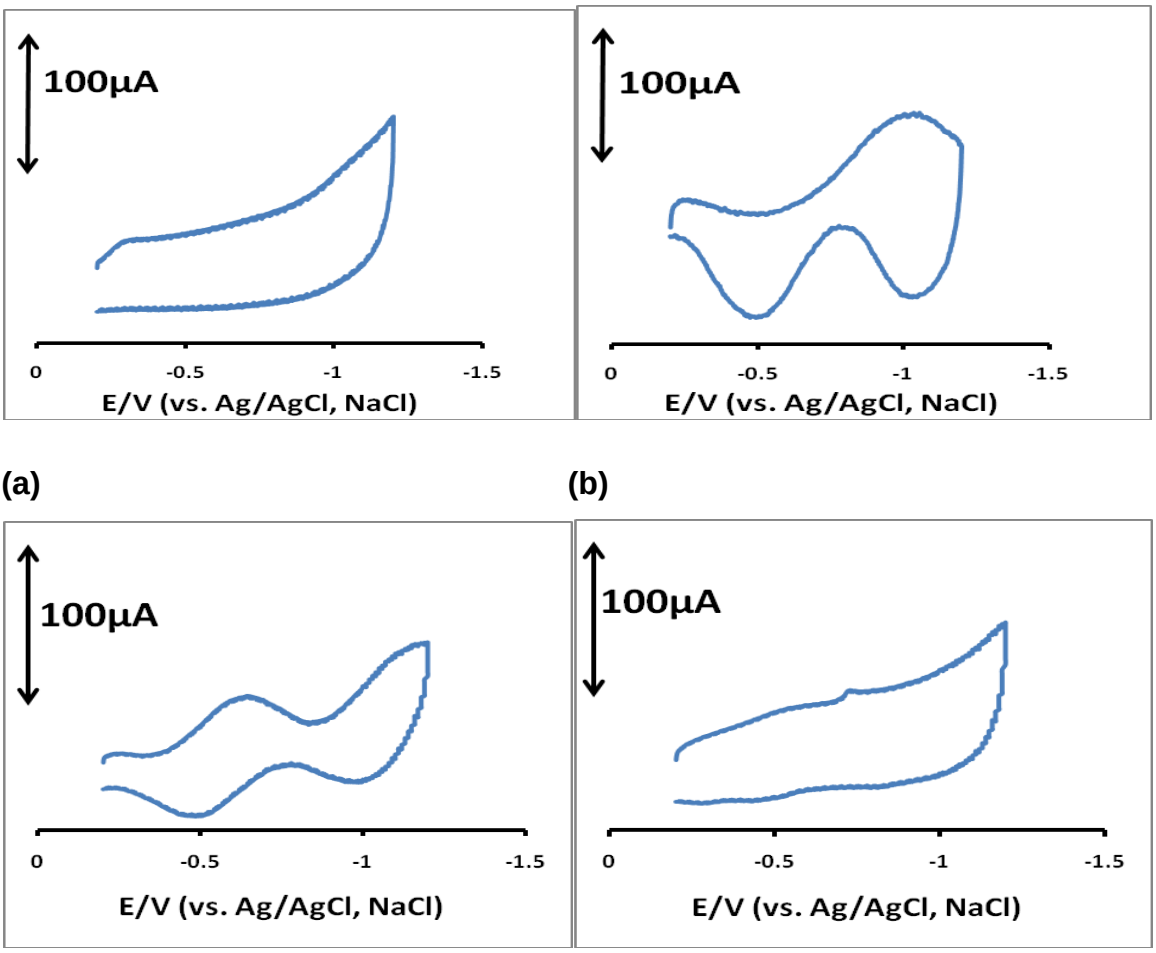

Figure 4.42: Cyclic voltammetric profiles of **(a)** Bare GCE, **(b)** GCE-MWCNT, **(c)** GCE-Ni and **(d)** GCE-MWCNT-Ni electrodes at a scan rate of 50 mV/s.

4.3.5.9.2 Effect of scan number on the anodic and cathodic peaks using GCE-MWCNT-Ni electrode

The effect of scan number was investigated by using GCE-MWCNT-Ni at a scan rate of 10 mV/s, as shown in figure 4.43. As the scan number increases, the cathodic current tends to increase, while the anodic current tends to decrease as

seen in figure 4.43 **(b)**. The grid lines clearly show an increase and a decrease behavior of current.

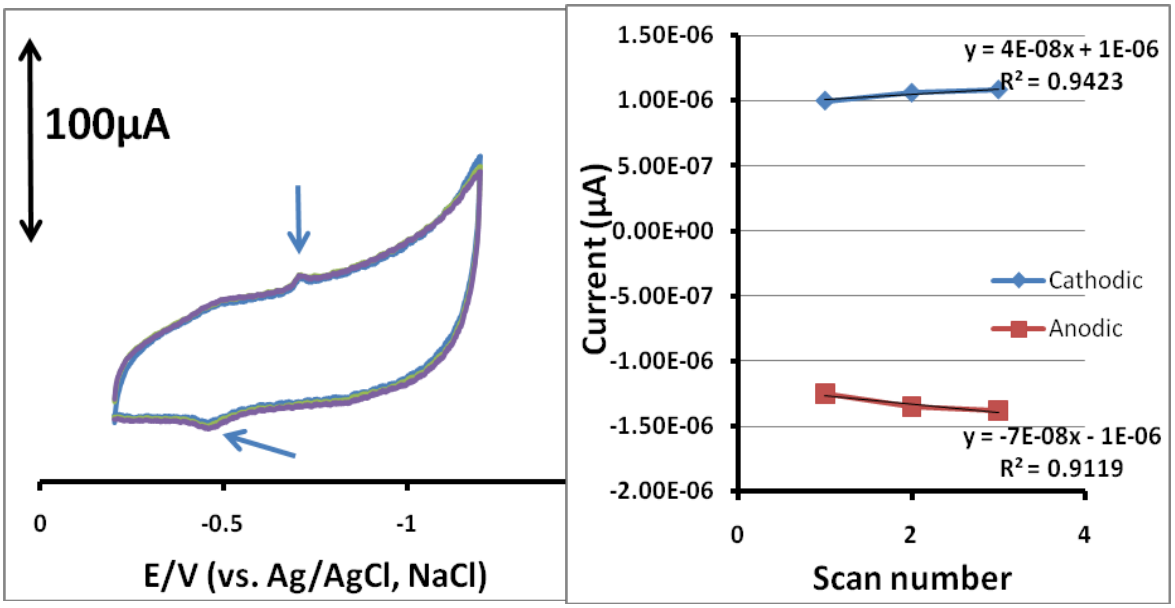

(a) **(b)**

Figure 4.43: (a) Cyclic voltammetric profiles depicting the effect of scan number at 10 mV/s and **(b)** the respective plot showing the effect of scan number on both the **(i)** cathodic and **(ii)** anodic current using GCE-MWCNT-Ni electrode. The arrows indicate the reproducible peaks.

4.3.5.9.3 Discharge capacity studies for Ni decorated MWCNTs

Comparison of the discharge capacity and behavior of GCE-MWCNT, GCE-Ni and GCE-MWCNT-Ni is shown in figure 4.44. The discharge voltages of GCE-Ni, and GCE-MWCNT-Ni as obtained in chronopotentiometry (*applied current of 1 μA*) are – 0.620 V and – 0.780 V respectively. As expected, a high discharge capacity is shown by GCE-MWCNT-Ni due to the present of both high surface area materials (MWCNT and Ni) combined. These results are consistent with the CV and discharge voltage studies where GCE-MWCNTs-Ni electrode gave the highest current respond and the highest discharge voltage compared to GCE-Ni. An increase in discharge capacity is as follows: bare GCE< GCE-MWCNT < GCE-Ni < GCE-MWCNT-Ni with the GCE-MWCNT behaving better that GCE-Ni since it does not gradually fall (retains its capacity) as the cycle number increases. The GCE-MWCNT-Ni also shows a short cycle life compared to GCE-MWCNT and GCE-Ni electrodes. From figure 4.44, it can be seen that Ni particles promote higher hydrogen-storage capability. Similar results were reported by Chien-Te *et al.* [84].

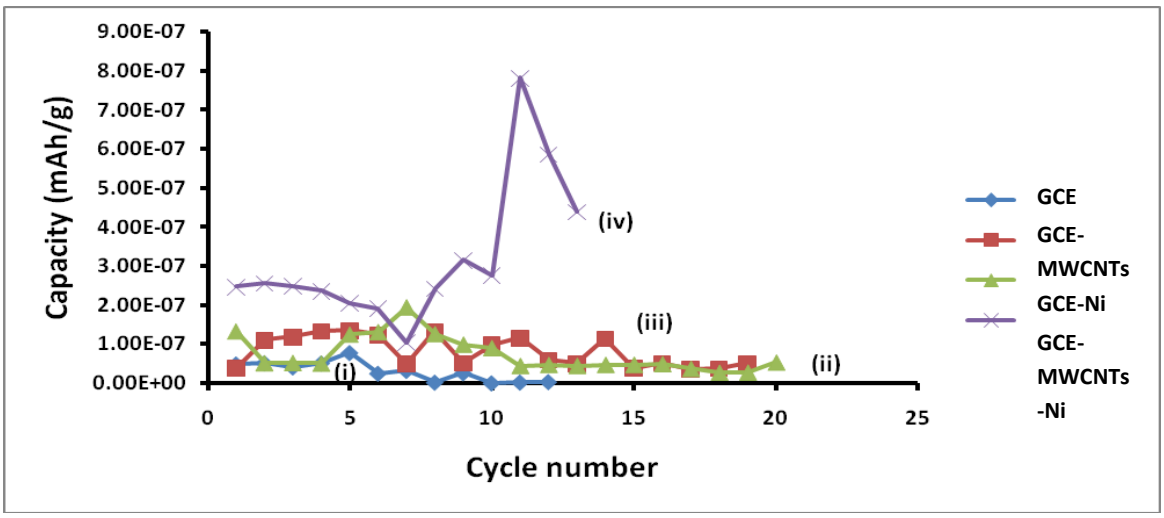

Figure 4.44: A plot depicting the effect of cycle number on the discharge capacity of **(i)** GCE, **(ii)** GCE-Ni, **(iii)** GCE-MWCNT and **(iv)** GCE-MWCNT-Ni electrodes.

The discharge capacities for the GCE, GCE-MWCNT, GCE-Ni and GCE-MWCNT-Ni electrodes are clearly presented in figure 4.45. It can be observed that the combination of MWCNTs and Ni nanoparticles results in a significant increase in hydrogen uptake by the GCE-MWCNT-Ni electrode. This confirms a synergy between MWCNTs and Ni nanoparticles. It was suggested that in addition to electrochemical storage of hydrogen, the other path for adsorbing and oxidizing hydrogen is that hydrogen molecules prefer to adsorb physically on MWCNTs, instead of electrochemical redox of hydrogen, followed by forming the metal hydride [84]. Researchers has inferred that this physisorption on MWCNTs may occur in pore or outer surface from atomic hydrogen produced by electrolysis [25] It is also said that metallic Ni supported on MWCNTs has the lower electrode overpotential [20], e.g., the connection between electrode material and current collector. The above speculations impact that the presence of Ni would facilitate the formation of hydrogen adsorption in aqueous solution [84].

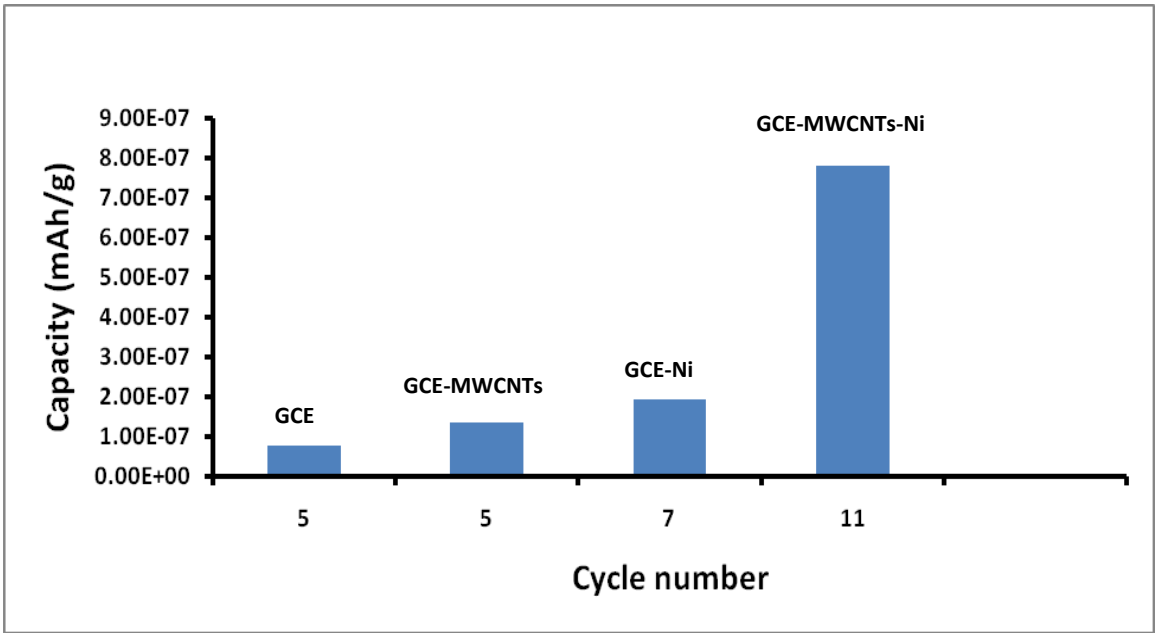

Figure 4.45: The bar graph clearly showing the discharge capacities of different glassy carbon modifiers.

The presence of nickel nanoparticles dispersed on the surface of the MWCNTs improves the hydrogen uptake by MWCNTs. This is due to the catalytic activity of the nickel nanoparticles which assists in the dissociation of hydrogen molecules to hydrogen atoms thereby allowing atomic hydrogen to adsorb chemically at the defective sites of the MWCNTs. The chemical adsorption process is improved by the presence of nickel nanoparticles whereby hydrogen atom occupies sites which would be prevented from adsorption in the other cases owing to the increase in hydrogen uptake [84].

4.3.5.10 Overall comparison of discharge capacities of different glassy carbon modified electrodes

Figure 4.46 compares the maximum capacities of different glassy carbon modified electrodes. The GCE-MWCNT-Ni electrode showed the highest hydrogen storage capacity of 8 nAh/g, which is equivalent to an H/C value of $28.32*10^{-9}$wt%. The lowest discharge capacity of 0.5 nAh/g was observed the GCE-Fe electrode. In general, it can be said that Iron nanoparticles are not suitable materials for hydrogen storage as it was seen also by the GCE-MWCNT-Fe_2O_3 and GCE-MWCNT-Fe electrodes giving low discharge capacities. GCE-Fe_2O_3 was able to outperform both GCE-CuO and GCE-Ni electrodes by giving high discharge capacity. The low discharge capacities by iron-base electrode (Fe_2O_3 and Fe) as compared to the copper and nickel-based electrodes may be one of the reasons why iron-based electrodes are not preferred in hydrogen storage studies.

From the copper-based electrodes and nickel-based electrodes, it is evident that nanoparticles enhance the electrochemical activity of MWCNTs by increasing their catalytic activity and surface area for hydrogen storage. Therefore, this results could lead to the conclusion that GCE-MWCNT-M (M = Ni or NiO) hybrid is suitable for hydrogen storage due to their high discharge capacities.

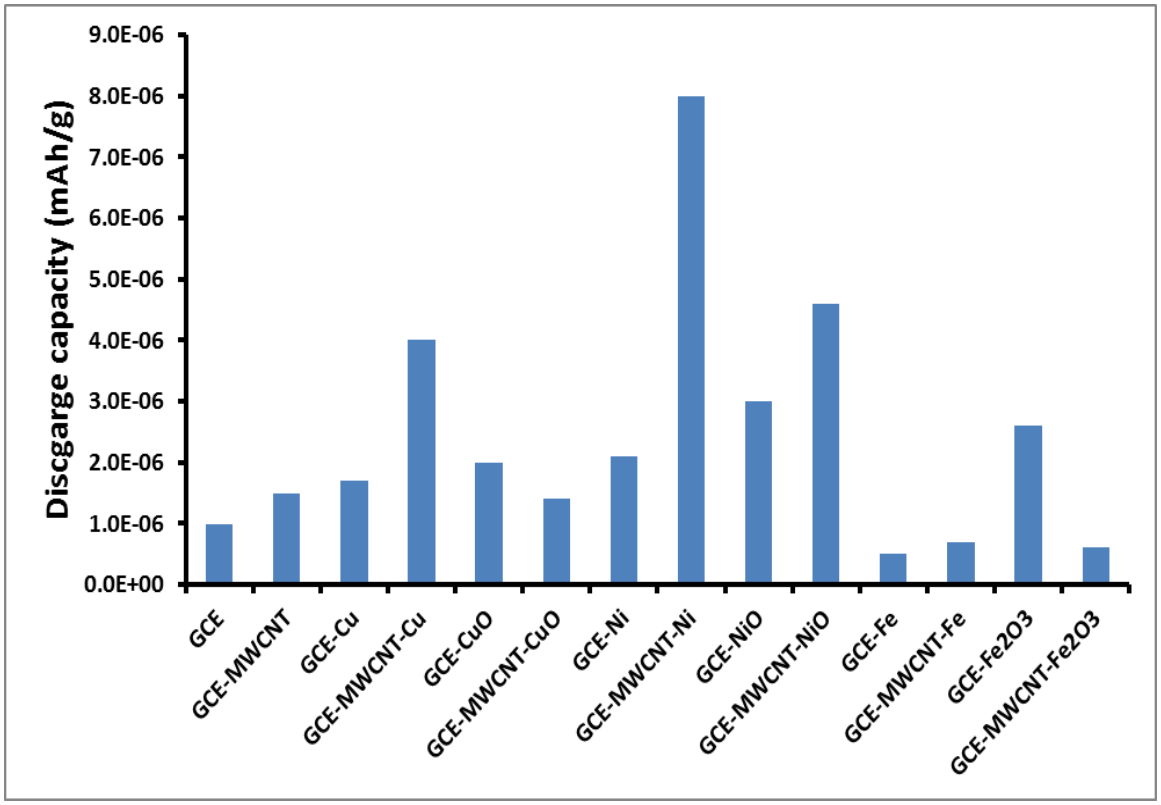

Figure 4.46: Comparison of the maximum capacity attained by specified electrode.

4.3.5.11 Effect of the MWCNTs loading

Carbon nanotubes (CNTs) combine unique chemical and physical properties which have attracted the interest of numerous researchers for applications such as supercapacitors, chemical sensors and energy storage devices [85-87]. The storage of hydrogen in a light element like carbon could lead to the formation of power suppliers for mobile applications with higher energy densities [88-91]. The variation of hydrogen storage capacity may arise due to the differences of CNTs used (SWCNTs or MWCNTs), purity, chirality of tubes, tube diameter, bundle

appearance, presence of metal catalyst and the amount of CNTs present [92, 93]. The percentage/amount of CNTs working electrode for hydrogen storage is one of the most important factor that need to be studied. CNTs have many properties that make them suitable materials for hydrogen storage such as: high surface area, controlled pore size, reversible behavior, high conductivity, etc [94-97]. The electrolysis temperature for this investigation was 21 ^{o}C.

4.3.5.11.1 Effect of MWCNTs loading on the current response

Cyclic voltammetric profiles for the effect of MWCNTs loadings on the current density for hydrogen storage are depicted in figure 4.47 **(a)**. It can be seen that as the amount of MWCNTs loading increases, there is a decrease in activity of the GCE-MWCNTs-Ni electrode as shown by the current density. This behavior is clearly shown in figure 4.47 **(b)** whereby a sharp decrease in current density is observed from 6wt% to 8wt% MWCNTs loading. This may be due to the decrease in surface area or reactive sites when more MWCNTs are added. Based on the results, it can be concluded that less carbon nanotubes (2wt% MWCNTs) provide a sufficient surface area for electrochemical activity in hydrogen storage. A broad cathodic peak for the GCE-MWCNT-Ni electrode is observed at a potential of -0.48 V vs. Ag/AgCl, NaCl reference electrode. Cyclic voltammetric profiles are nearly rectangular in shape, typical of a high energy and power density MWCNTs materials. These results are consistent with the results reported by Tarbena *et al*. [98], where a gradual decrease in peak current was observed as the amount of CNTs were loaded [98]. Carbon nanotubes addition caused a linear decrease in current response, but this is not always the case as the current response reduction is moderated by another effect: enhancement of both ionic and electronic percolation networks resulting from CNT presence in the active material. Carbon nanotubes form an open mesoporous network which

makes it easier the ion adsorption and limits the current response loss when CNTs content increases in the active material [48, 49].

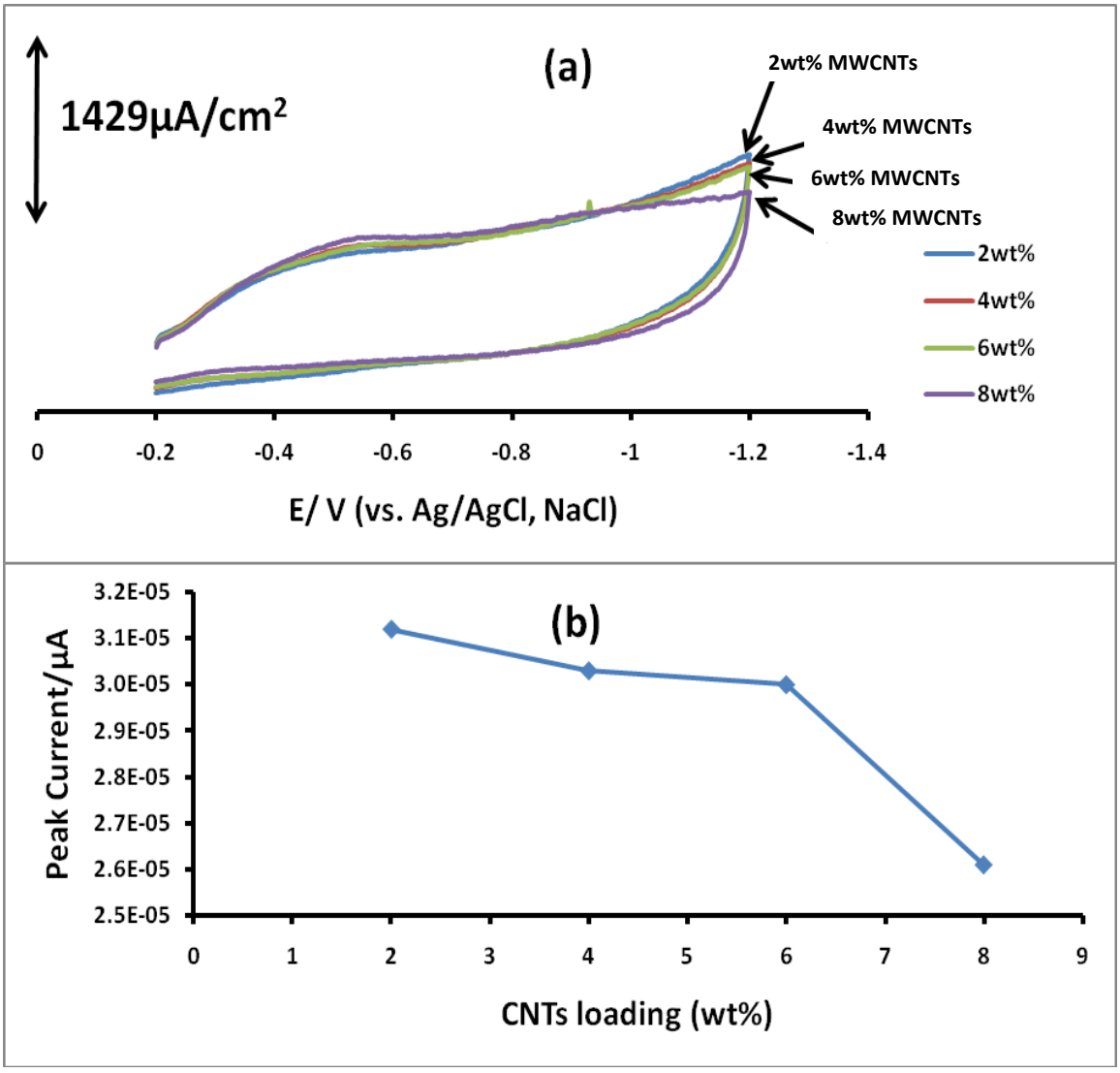

Figure 4.47: (a) Cyclic voltammetric profiles showing the relationship between current density and the amount of MWCNTs in a 6 M KOH electrolyte using the GCE-MWCNT-Ni at a sweep rate of 100 mV/s. **(b)** A plot showing the relationship between the peak current and MWCNT 's loading.

4.3.5.11.2 Influence of MWCNTs loading on the discharge current

The following study investigates the effect of MWCNTs loading (2wt%, 4wt%, 6wt% and 8wt%) on the discharge current using the MWCNT-Ni_{uncal} electrode. The GCE-MWCNT-Ni (2wt% MWCNTs) electrode shows the highest discharge current of 3.64E-06 µA compared to the 4wt% MWCNTs (2.36E-06µA), 6wt% MWCNTs (3.16E-06 µA) and 8wt% MWCNTs (1.7E-06 µA) as shown in figure 4.48. Similar results were reported by Tarbena *et al*. [98], where they found that CNTs loading was inversely proportional to the discharge capacity. The best results by the GCE-MWCNT-Ni (2wt% MWCNTs) electrode are consistent with CV, discharge profile in CP and CPE. For each CPE run, the applied potential was determined from the respective CP run. In the previous reports where MWCNTs weight percentages were higher, 4wt% MWCNTs gave a highest current response, discharge voltage and discharge current. From these results, 4wt% of MWCNTs appears to be a good compromise for maximum hydrogen storage in the GCE-MWCNT-Ni electrode.

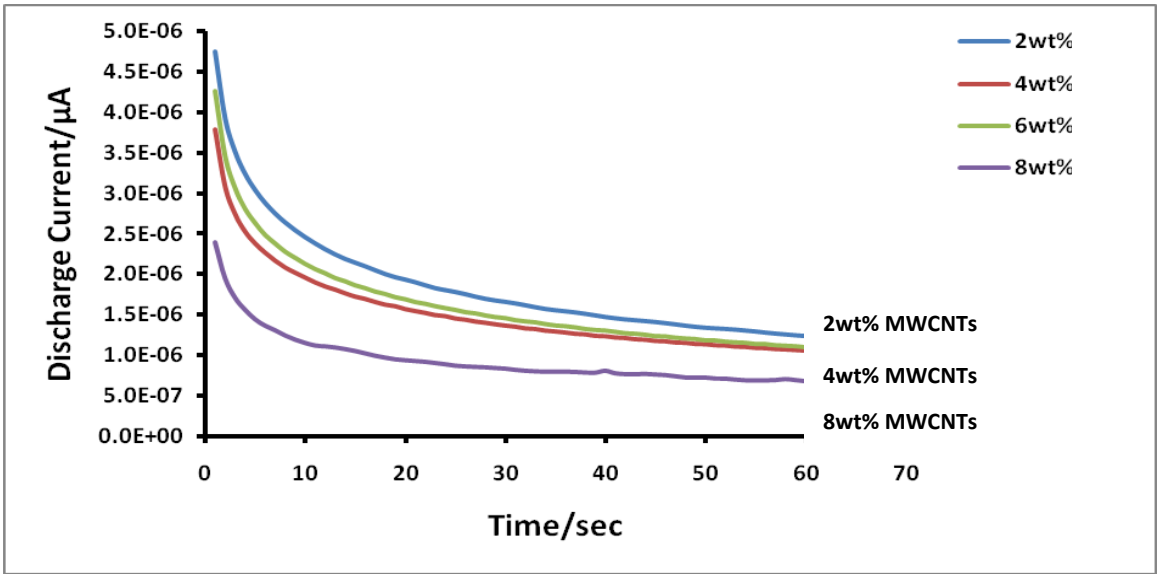

Figure 4.48: Controlled potential electrolysis profiles for the GCE-MWCNT-Ni electrodes showing the effect of MWCNTs loadings on the discharge current.

4.3.5.12 Effect of the Ni loading

Among various applications of carbon nanotubes, there has been increasing interest in CNTs as heterogeneous catalyst support. Pioneer studies have pointed out that metal nanoparticles supported on CNTs provide an excellent catalyst activity [99, 100]. For instance, Xiang *et al.* [52] has used sonochemical technique to deposit Pt nanoparticles onto the surface of CNTs, exhibiting a great activity in electrochemical adsorption and desorption of hydrogen. Kibria *et al*. [101] have indicated that Li-doped CNTs produce a higher hydrogen storage capacity, which is six times higher than undoped CNTs. However, there are few reports focused on the reactivity of metal nanocatalyst in electrochemical system. However, the role that the attachment of nickel on CNTs plays in hydrogen storage in electrochemical systems has not yet been clearly elucidated [102, 103]. The KOH electrolyte temperature for this study was 21 ^{o}C.

4.3.5.12.1 Comparative impact of Ni loading on the current response at various scan number

The following study investigates the influence of the quantity of nickel nanoparticles on the current response at the first and third scan number. The electrolysis temperature for this study was 21 ^{o}C. Hydrogen is adsorbed in the cathodic direction and desorbed in the anodic direction. Therefore, the mechanism for the electrochemical reaction of MWCNT-Ni electrode can be expressed as follows:

$$Ni + xH_2O + xe^- \longleftrightarrow Ni.xH_{ads} + xOH^-, \quad \textbf{(Scheme 4.4)}$$

$$Ni.xH_{ads} + CNT \longleftrightarrow CNT.xH_{ads} + Ni. \quad \textbf{(Scheme 4.5)}$$

Since the peak current known to be proportional to Ni loading, reaction scheme 4.4 is thus the rate-determining step in the overall electrochemical reaction. At first, each Ni nanoparticle adsorbs x hydrogen atoms. This means that high coverage of Ni nanoparticles can promote the greater hydrogen storage capability [84]. Then the adsorbed H atoms were transferred from the Ni of CNT-Ni electrode surface into CNTs after adsorption at Ni site. This mechanism tells us that Ni catalyst promote an electrochemical activity for hydrogen storage and the presence of CNTs also act as an acceptor, which provide enough sites for hydrogen storage. In addition to electrochemical storage of hydrogen, the other path for adsorbing and oxidizing hydrogen is that the hydrogen molecule prefers to adsorb physically on the CNTs, instead of electrochemical redox of hydrogen, followed by forming the metal hydride [84].

4.3.5.12.1.1 Impact of Ni loading on the current response at the first scan number

The GCE-MWCNT-Ni (4wt% Ni) electrode shows the highest current density as depicted by the first CV scan in figure 4.49 **(a)**. From which an increase in Ni content results in a decrease in current density as observed when using the GCE-MWCNT-Ni (8wt% Ni) electrode. The plot in figure 4.49 **(b)** clearly shows the effect of Ni loading on the current respond. It can be seen that there is an increase in current respond from 2wt% Ni to 4wt% Ni consistent with the results reported by Chien-Te *et al*. [84]. However, a decrease in current respond was observed when additional amounts of nickel are introduced. This decrease in current responds when higher amount are added is in contrast with the results reported by Chien-Te *et al*. [84] where the current response increased linearly as the Ni were loaded. The GCE-MWCNT-Ni (4wt% Ni) electrode shows a broad anodic peak at a potential of about -0.8 V vs. Ag/AgCl reference electrode. It was proved in previous reports that higher weight percentage of Ni nanoparticles

results in a direct proportionality with current density, discharge voltage and discharge capacity.

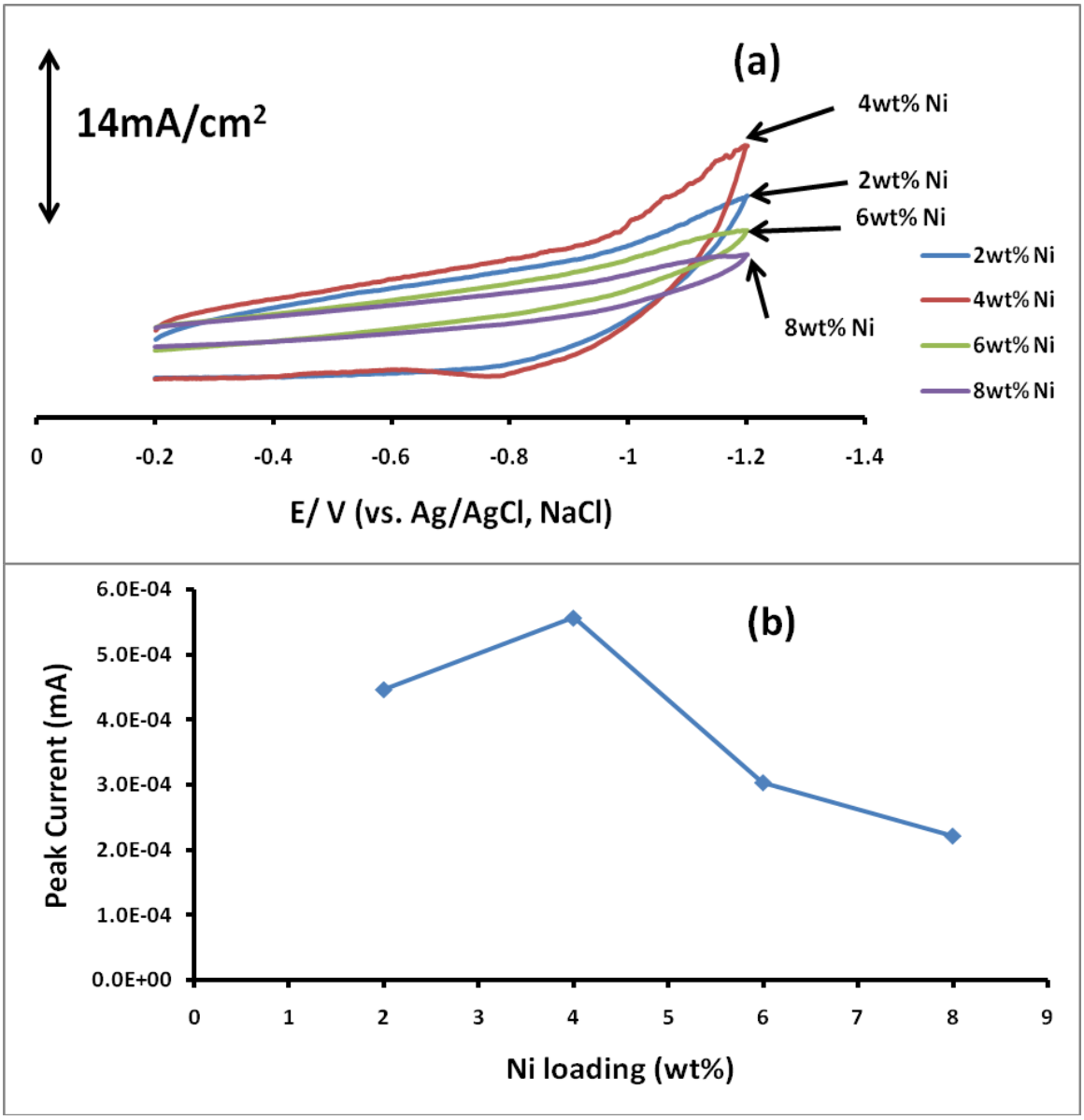

Figure 4.49: (a) Comparative CV profiles for the first scan recorded at the GCE-MWCNT-Ni electrode for different Ni loadings in a 6 M KOH electrolyte. Scan rate = 100 mV/s. **(b)** The plot showing the relationship between Ni loading and peak current.

4.3.5.12.1.2 Impact of Ni loading on the current response at the third scan number

Figure 4.50 **(a)** shows the third CV scans for Ni loadings justifying the fact that the GCE-MWCNT-Ni (4wt% Ni) electrode gave the highest current density as compared to lowest current density by the GCE-MWCNT-Ni (8wt% Ni) electrode. The results shows that the electrochemical adsorption and desorption of hydrogen is not a linearly increasing function of the Ni loading as was indicated in section 4.3.5.12.1.1 The enhancement in electrochemical activity from 2wt% Ni to 4wt% Ni was ascribed to the fact that Ni nanoparticles act as the redox site for hydrogen storage, thus leading to greater specific peak current as shown in figure 4.50 **(a)**. A decrease in porosity of the MWCNTs is seen from 4wt% Ni to 8wt% Ni due to increase in ohmic resistance, caused by a decrease in surface area or active reactive sites for the Ni nanoparticles. A sharp decrease in current response is observed from 4wt% Ni to 6wt% Ni and finally to 8wt% Ni as clearly shown in figure 4.50 **(b)**. It is also important for the Ni nanoparticles to be well-dispersed on the surface of the MWCNTs to provide maximum reactive sites.

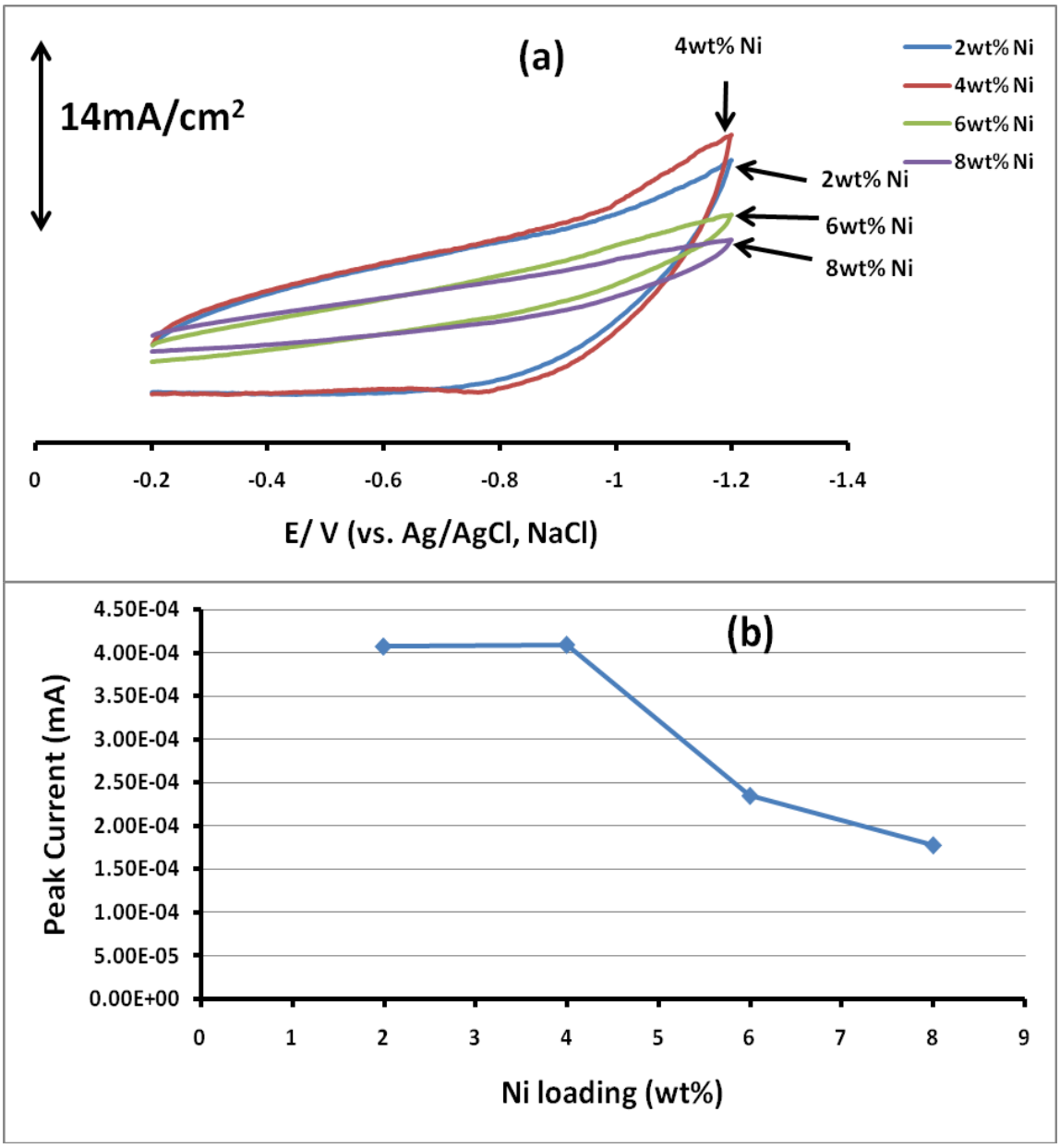

Figure 4.50: (a) Comparative CV profiles for the third scan recorded at the GCE-MWCNT-Ni electrode for different Ni loadings in a 6 M KOH electrolyte. Scan rate = 100 mV/s. **(b)** The plot showing the relationship between Ni loading and peak current.

4.3.5.12.2 Influence of Ni loadings on the discharge current

Figure 4.51 below depict the CPE profiles for the effect of different Ni loadings on the discharge current. The applied potentials for each CPE analysis were obtained from the respective chronopotentiometric run. The GCE-MWCNT-Ni (4wt% Ni) shows the highest discharge current which are the best results in consistent with the CV and discharge voltage profile, in chronopotentiometric experiments. The GCE-MWCNT-Ni (2wt% Ni) electrode behaves in the same manner as the GCE-MWCNT-Ni (4wt% Ni) electrode, but it is discharged from a less amount of current compared to the 4wt% Ni, i.e. the GCE-MWCNT-Ni (4wt% Ni) electrode is discharged to a current of 2.62E-05 µA compared to 1.08E-05 µA by the GCE-MWCNT-Ni (2wt% Ni) electrode. The 6wt% Ni and 8wt% Ni electrodes show a small discharge current. The highest discharge current by the 4wt% of Ni implies that the Ni catalyst have different activities at different Ni loadings [104]. It is believed that Ni nanoparticles act as a redox site in the electrochemical system as reported by Chien-Te *et al*. [84]. In this case, 4wt% Ni acting as a redox site lead to a greater hydrogen-storage capability compared to other Ni weight percentages. Low discharge capacity by higher Ni loadings may be due to the fact that Ni nanoparticles become large at higher loadings, and as a result, better dispersions can be achieved only at low nickel percentages [104].

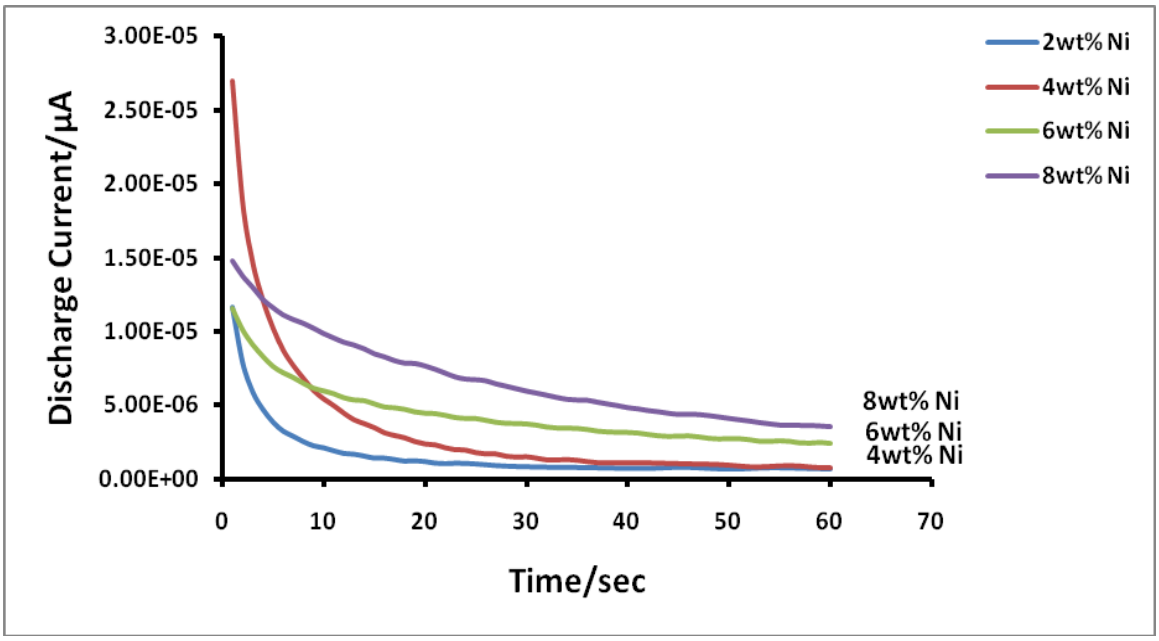

Figure 4.51: Controlled potential electrolytic profiles for the GCE-MWCNT-Ni electrode at different Ni nanoparticles loadings.

4.3.5.13 Effect of calcined and uncalcined Ni nanoparticles on electrochemical activity of glassy carbon electrode

Since calcination is an endothermic reaction, temperature in the calcination zone of the particle decreases and heat transfer process occurs from the particle surroundings to that zone [105, 106]. The relative importance of the heat transfer process is greatly influenced by the particle size [107]. However, mass transfer and chemical reaction have been considered as the rate-limiting processes by the majority of the authors. In recent years, nanomaterials have extensively attracted interest for their small and quantum size effects [108]. Nanomaterials can exhibit novel and significant mechanical, electronic, magnetic and optical properties in comparison with their bulk counterparts. Ni and NiO are important transition metal nanocatalysts [109, 110]. Furthermore, nickel materials are very prosperous materials extensively used as catalysis, battery cathodes, gas

sensors, electrochronic films and magnetic materials [111]. Because of the volume effect, the quantum size effect, the surface effect and the macroscopic quantum tunnel effect, nanocrystalline NiO and Ni are expected to possess many improved properties than those of micrometer-sized NiO and Ni particles which are influenced by calcination [112-114]. This section investigates the effect of calcining Ni nanoparticles on the current density, charge-discharge voltages and on the hydrogen evolution studies using the GCE-MWCNTs-Ni electrode. The hybrid of carbon nanotubes and nickel nanoparticles was used to monitor the effect of calcined Ni nanoparticles. The calcination was undertaken at 400 ^{o}C. Electrolysis temperature for this investigation was 24 ^{o}C.

4.3.5.13.1 Comparative cyclic voltammetric responses of MWCNT-Ni_{cal} and MWCNTs-Ni_{uncal} at the surface of the glassy carbon electrode

The GCE-MWCNT-Ni_{uncal} electrode shows a higher current density than the GCE-MWCNT-Ni_{cal} electrode as depicted in figure 4.52. Calcination affects the nanoparticles surface area responsible for storage of hydrogen. The low current density of the GCE-MWCNT-Ni_{cal} electrode is due to the sintering effect and crystal growth of the particles. It is suggested that calcined nickel nanoparticles tend to block the tubes of the MWCNTs resulting in low hydrogen amount being stored. It is also known that calcining the nickel nanoparticles destroys the active ions responsible for the formation of the strong bond between MWCNTs and Ni. Therefore, MWCNTs tend to interact weakly with the Ni resulting in low current density [95, 96].

The results suggest that, the size of the nickel nanoparticles and the diameter of the CNTs need to be controlled for maximum adsorption of hydrogen. It is important to calcine these nanoparticles at a temperature that will not affect the stability of nanoparticles. Inhibitors such as K_3PO_4 are used to prevent sintering and agglomeration of nanoparticles at high temperatures. Nanosized materials

with sizes below 100 nm are of scientific interest because of improved physico-chemical properties [115]. The uncalcined nickel nanoparticles seem to be more electrochemically active than the calcined nickel nanoparticles. It seems like the calcinations temperature used decreased the specific surface area of the nickel nanoparticles, but it known that with an increase in calcinations temperature, the average pore radius tend to increase as a results of the shrinkage of the agglomerates, destruction of the minute intercrystallite pores and the inter-agglomerate densification [115].

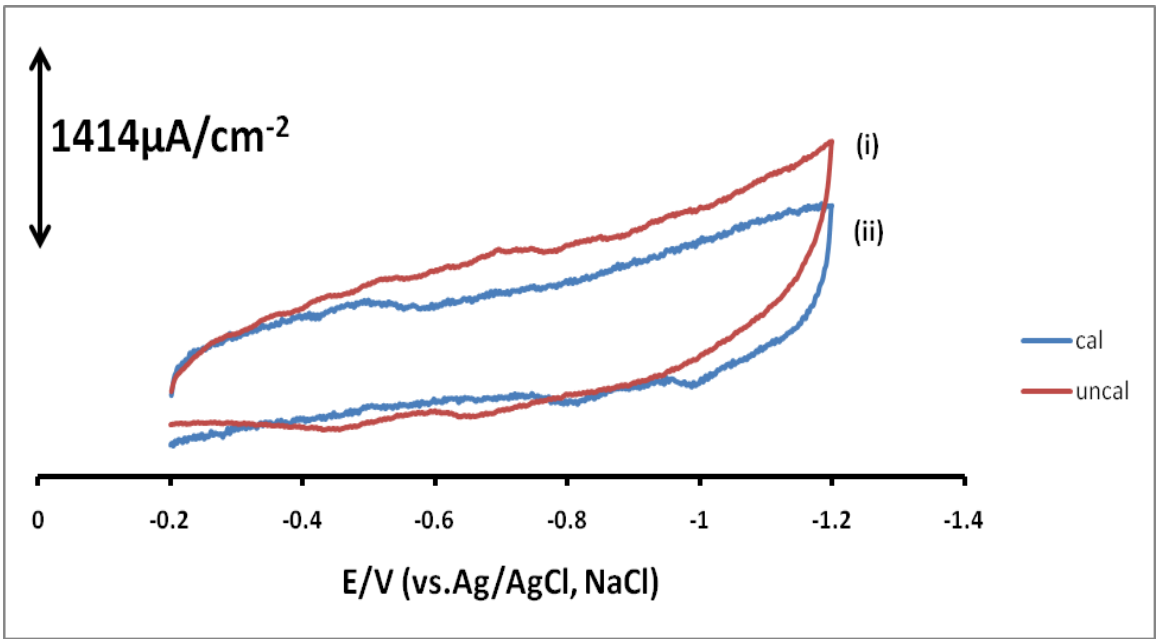

Figure 4.52: Comparative cyclic voltammetric profiles of **(i)** GCE-MWCNT-Niuncal and **(ii)** GCE-MWCNT-Nical at a scan rate of 10 mV/s.

The broad cathodic and anodic peak can be observed for both GCE-MWCNT-Ni_{uncal} and GCE-MWCNT-Ni_{cal}. It is advantageous to scan at a low rate because information about adsorption and desorption of hydrogen from the GCE-MWCNT-Ni electrode can be obtained. Anodic peaks for GCE-MWCNT-Ni_{cal} are obtained at about -1 V and -0.8 V, while for GCE-MWCNT-Ni_{uncal} electrode, the peaks are at about -0.6 V and -0.4 V vs. Ag/AgCl reference electrode.

4.3.5.13.2 Charge-discharge voltage analysis

The analysis was undertaken at a constant applied charge current of -2 µA for 60 seconds (1 min). The charge curves of GCE-MWCNT-Ni_{cal} and GCE-MWCNT-Ni_{uncal} electrodes are shown in figure 4.53. It can be observed that GCE-MWCNT-Ni_{uncal} electrode tend to be charged to a high voltage compared to GCE-MWCNT-Ni_{cal} electrode. The maximum electrochemical charge voltage of -0.165 V is obtained in the GCE-MWCNT-Ni_{uncal} electrode, while the maximal charge voltage of GCE-MWCNT-Ni_{cal} electrode is 0.065 V. This obtained high charge voltage for GCE-MWCNT-Ni_{uncal} is consistent with the high current density obtained by cyclic voltammetry.

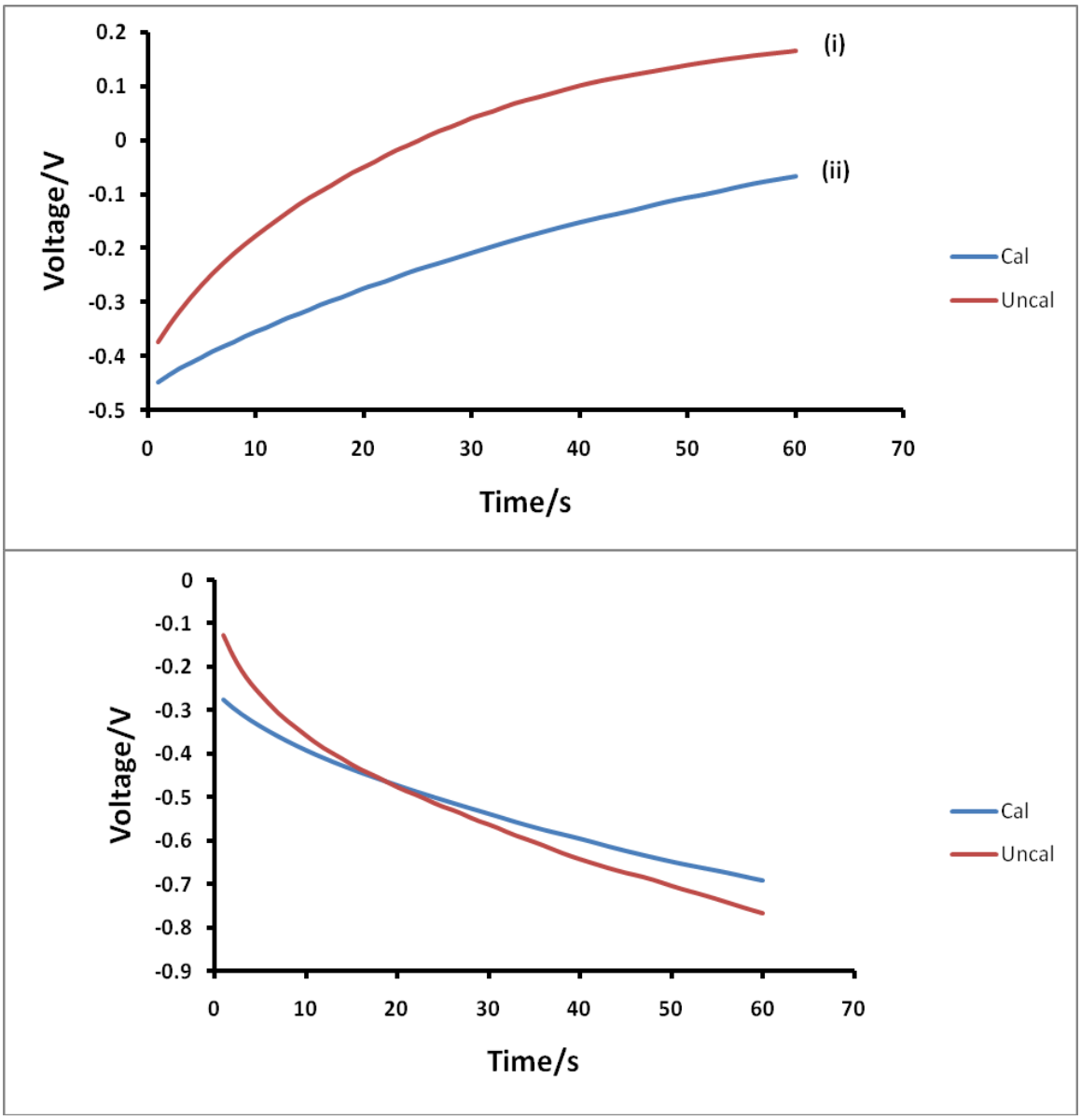

Figure 4.53: Charge and discharge profiles of **(i)** GCE-MWCNT-Ni_{uncal} and **(ii)** GCE-MWCNT-Ni_{cal} from an applied charge current of -2 µA.

4.3.5.13.3 Hydrogen evolution reaction studies

It is known that during the charging process, the water in the electrolyte dissociate at the working electrode and the adsorbed atomic hydrogen may be

adsorbed or intercalate in the electrode or recombine at the surface to molecular hydrogen and diffuse into the electrode. The formation of the molecular hydrogen on the surface of the electrode is observed by the gas bubbles. This prompted an investigation of the hydrogen evolution reaction. The general equation for hydrogen gas evolution reaction is expressed as follows:

$$2H^+ + 2e^- \longrightarrow H_2\ (g) \qquad \textbf{(Scheme 4.6)}$$

Two hydrogen adatom combine to form the hydrogen molecule. In the case of the MWCNT-Ni electrode, the mechanism for hydrogen evolution can be expressed as follows:

$$\text{MWCNT-Ni} + nH_3O^+ + ne^- \longrightarrow \text{MWCNT-NinH} + nH_2O, \qquad \textbf{(Scheme 4.7)}$$

Where H denote the hydrogen adatom intermediate and n represent the number of moles. Molecular hydrogen can be formed both by adatom recombination (the Tafel-Volmer route, scheme (4.7) and (4.8) or following the Heyrovsky-Volmer (scheme (4.7) and (4.9)) route [116].

$$\text{MWCNT-NinH} \longrightarrow \text{MWCNT-Nin}\ 0.5H_2 \qquad \textbf{(Scheme 4.8)}$$

$$\text{MWCNT-NinH} + nH_3O^+ + ne^- \longrightarrow \text{MWCNT-Nin}H_2 + nH_2O \qquad \textbf{(Scheme 4.9)}$$

The hydrogen evolution reaction is an electrocatalytic reaction and it is irreversible. The rate at which hydrogen ions are transformed into hydrogen gas is a function of several factors, including the rate of electron transfer from the GCE-MWCNT-Ni electrode to the hydrogen ions. It is expected that the rate of hydrogen evolution from GCE-MWCNT-Ni_{cal} and GCE-MWCNT-Ni_{uncal} electrodes should vary greatly.

4.3.5.13.3.1 GCE-MWCNT-Nical (4wt% Ni) electrode

The TEM images for the MWCNTs-Ni_{cal} are depicted clearly in figure 4.6, with Ni_{cal} nanoparticles well dispersed on the surface of the activated MWCNTs. The hydrogen evolution and oxidation on the GCE-MWCNT-Ni_{cal} electrode was investigated by applying discharge current ranging from 2 µA to 8 µA in chronopotentiometry. The GCE-MWCNTs-Ni hybrid was chosen because it gave the maximum discharge capacity compared to other metal nanoparticles and metal oxides decorated MWCNTs.

Figure 4.54 shows the voltage profile for the GCE-MWCNT-Ni_{cal} electrode. The potential of the electrode decreased gradually during discharging and its polarization was relatively low even for the discharge current of 8 µA. This observation is consistent with the results reported by Sabina *et al*. [61], who used the CNTs electrode and discharged it with a current ranging from 0.2 to 3.2 mA to determine the hydrogen evolution studies.

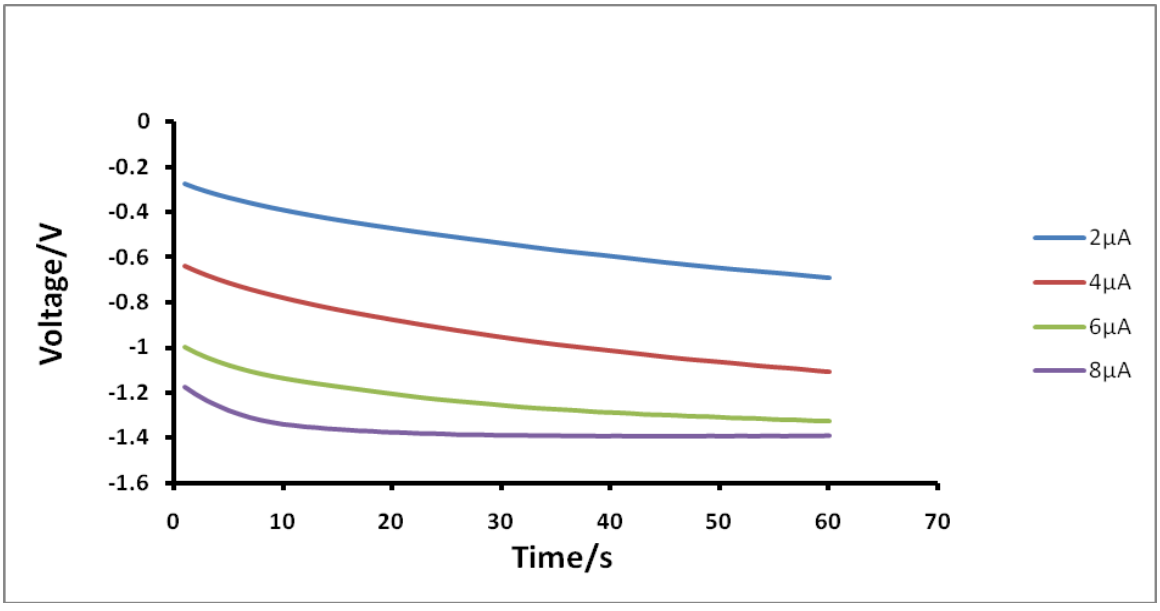

Figure 4.54: Discharge profiles of GCE-MWCNT-Nical electrode from an applied discharge current of 2 µA to 8 µA.

Kinetic parameters were obtained by plotting data registered at low overpotential, which is the method suggested by Allen and Hickling. The classical Tafel equation can be expressed as follows:

$$\text{Log } [i/(1-\exp(-nF\acute{\eta}/RT)] = \log(i_o)-\alpha nF\acute{\eta}/2.3RT \qquad \textbf{(Eq. 4.3)}$$

Where i_0 is the anodic or cathodic current, n is the number of participating electrons, R is the gas constant, i.e. 8.314 J mol^{-1} K^{-1}, T is the absolute temperature (K), F is the faraday constant corresponding to 96485 C/(mole of electrons), and ή is the overvoltage in volts (V).

The exchange current density (i_0) is surely the single most important variable that explains the large difference in the rate of hydrogen evolution on the surface of the electrode. It is a fundamental characteristic that can be defined as the rate of oxidation or reduction of the electrode at equilibrium expressed in terms of current [61].

Figure 4.55 is a plot of overpotential (ή) measured at the end of the discharge versus log[i/(1-exp(-nFή/RT)] with the current density determined from the geometric area of the electrode. The value of the exchange current density extrapolated at ή = 0 was found to be 1.07 µA cm^{-2}. The high value of the estimated exchange current density makes this MWCNT-Ni_{cal} a good electrocatalyst for the hydrogen evolution reaction. The higher the exchange current density value obtained, suggests that the hydrogen evolution reaction occurs rapidly [61]. These results suggest that in future, the GCE-MWCNT-Ni_{cal} nanocomposite electrodes will replace the expensive noble metals used as catalysts in acid electrolysers. But high overvoltage for hydrogen oxidation makes GCE-MWCNT-Ni electrode inadequate for use as catalyst in fuel cell applications. From letter A and B on the Tafel plot, the value of the slope was calculated as follows:

Slope = - αnF/2.3RT = 0.029 V^{-1},

The Tafel slope provides mechanism about the hydrogen evolution reaction and act as a key connection to reaction rate theory. Assuming low coverage of adsorbed hydrogen, the only mechanism which will give rise to a transfer coefficient of less than 1.5, at low overpotential is the discharge followed by a rate determining electrode desorption. From these results, it follows that the hydrogen evolution follows the Heyrovsky-Volmer route [116]. At a temperature of 25 ^{o}C with n = 1,

- αnF/2.3RT = Slope = 0.029 V^{-1}, from which the transfer coefficient (α) of the GCE-MWCNT-Ni_{cal} electrode was calculated to give α = 0.002

The general Tafel‘s law is expressed as follows:

ή = a + b*log (i_0), from which was determined from the straight line Tafel curve to give;

y = 0.029x – 5.97, where a constant b (slope) was 0,029 and -5.97 is a constant a.

The discharge voltage plateau was observed for the applied discharge current of 8 µA at a potential of -1.39 V vs. Ag/AgCl reference electrode. The quantity of hydrogen oxidised in the discharge step is increased by increasing the discharge current use for hydrogen evolution. These results can be related with an increased hydrogen adatom concentration, over the equilibrium concentration, with increased discharge current.

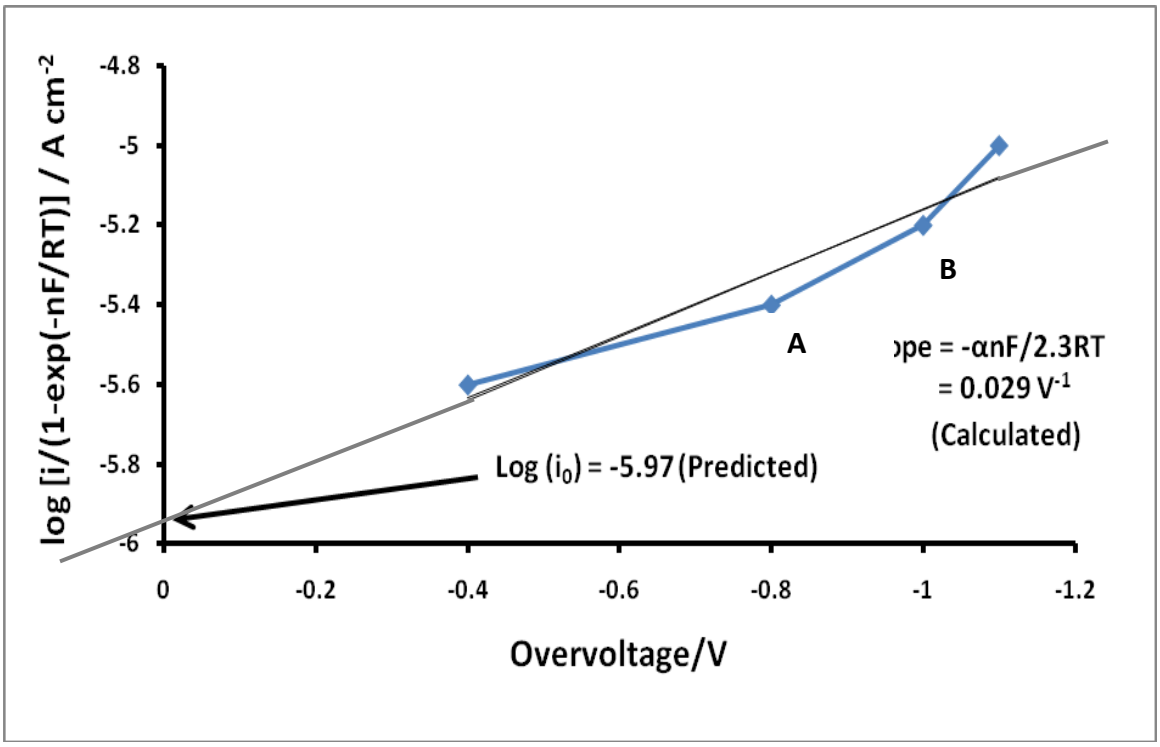

Figure 4.55: The respective modified Tafel plot for hydrogen evolution studies.

4.3.5.13.3.2 GCE-MWCNT-Ni_{uncal} (4wt% Ni) electrode

The TEM images for the MWCNTs-Ni_{uncal} are clearly shown in figure 4.5, with Ni_{uncal} nanoparticles dispersed on the surface of the oxidized MWCNTs. The effect of applied discharge current on the discharge voltage of GCE-MWCNT-Ni_{uncal} electrode is shown in figure 4.56 **(a)**. It can be seen that as the applied discharge current is increased, there is also an increase in discharge voltage. A significant increase is observed from an applied current of 4 µA. No significant increase in discharge voltage is seen for 8 µA. Note that the GCE-MWCNT-Ni_{uncal} electrode is discharged to a more voltage than the GCE-MWCNT-Ni_{cal} electrode.

The modified Tafel plot in figure 4.56 **(b)** was obtained from the data for the discharge voltage profile in figure 4.56 **(a)**. The value of the logarithm of the

exchange current density was extrapolated to give -6.2 A cm^{-2}. The value of the exchange current density at ή = 0 was found to be i_0 = 0.63 μA cm^{-2}, which tend to be less than that of the GCE-MWCNT-Ni_{cal} electrode, implying that the GCE-MWCNT-Ni_{cal} electrode is a good electrocatalyst for hydrogen evolution reaction [46]. This is true, since calcination of nickel nanoparticles increases their size responsible for the adsorption of large hydrogen molecules as compared to the small hydrogen atoms. This means that the GCE-MWCNT-Ni_{uncal} can be added in power cells such as popular alkaline primary cells to stifle (prevent) the thermodynamically favored production of the gaseous hydrogen and prevent unpleasant incidents [63]. These results are consistent with the TEM images where Ni_{cal} were shown to be well dispersed on the surface of the MWCNTs than the Ni_{uncal} (see TEM images figure 4.5 and 4.6). Points A and B on the Tafel plot (figure 4.56) were used to obtain the slope. The slope of the Tafel plot was calculated as follows;

Slope = - αnF/2.3RT = 1.25 V^{-1}, which is greater than of the GCE-MWCNT-Ni_{cal} electrode, implying that the transfer coefficient (α) of the GCE-MWCNT-Ni_{uncal} is more than of the GCE-MWCNT-Ni_{cal} electrode. At 25 ^{o}C with n = 1, α = 0.07, showing a fast electron transfer kinetics on the surface of the GCE-MWCNT-Ni_{uncal} electrode as compared to the GCE-MWCNT-Ni_{cal} electrode.

The Tafel ‘s law can be expressed as follows:

y = 1.25x – 6.2, where a, is a constant of - 6.2 and b is a Tafel slope of 1.25.

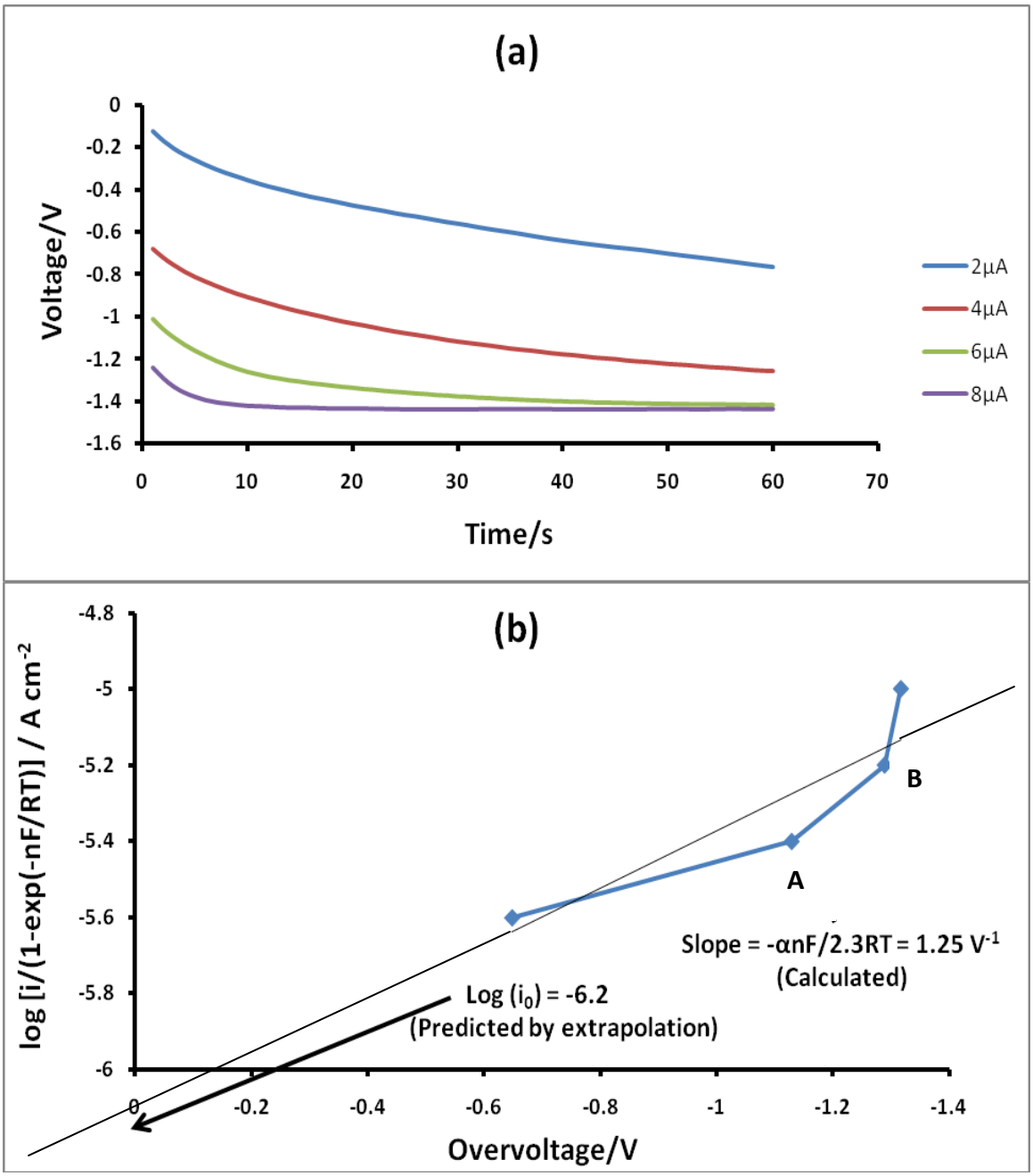

Figure 4.56: (a) Discharge profiles of GCE-MWCNT-Ni_{uncal} from different applied discharge current and **(b)** the respective Tafel plot showing the obtained exchange current density from the intercept.

4.3.5.13.4 Effect of the applied discharge current on the discharge capacity

The following study investigates the effect of applied discharge current (from 2 µA-8 µA) on the discharge capacity using GCE-MWCNT-Ni_{cal} and GCE-MWCNT-Ni_{uncal} nanocomposite electrodes.

4.3.5.13.4.1 GCE-MWCNT-Nical (4wt% Ni) electrode

Figure 4.57 **(a)** compares the behavior of discharge capacity of GCE-MWCNT-Ni_{cal} electrode obtained as a result of applying different discharge current. An applied current of 2 µA surprisingly results in a maximum discharge capacity. Followed by an increase in capacity in the order; 4 µA < 6 µA < 8 µA. It can be seen that with an increase in discharge capacity, the GCE-MWCNT-Ni_{cal} tend to have a short cycle life. The GCE-MWCNT-Ni_{cal} applied current profile of 2 µA lives up to cycle number 10, while for 4 µA the cycle life is up to 28. This behavior was also observed by Dong *et al.* [59] who investigated the effect of discharge current density on the specific discharge capacity using the as-grown SWCNTs. They discovered that as the discharge current density increases, the discharge capacity tend to gradually increases. But when SWCNTs-Ppy nanocomposite was used, the discharge capacity gradually decreases with an increase in discharge current density.

The relationship between the discharge capacity of GCE-MWCNT-Ni_{cal} for hydrogen and applied discharge current is shown in figure 4.57 **(b)**. At an applied current of 2 µA a capacity of 8.49E-06 mAh/g is reached. As 4 µA discharge current is applied, the capacity tends to drop to 7.62E-07 mAh/g, after which a gradual increase in capacity with discharge current is seen. The behavior for an applied current of 2 µA may be due to the fact that at the start of the analysis, the

amount of the GCE-MWCNT-Ni_{cal} is higher and as the analysis continues, some of the MWCNT-Ni_{cal} tends to fall from the GCE bare electrode until the stability is attained. Or the behavior may arise due to the poisoning effect of the GCE-MWCNT-Ni_{cal} electrode which tent to lose activity (the concentration of the H^+ on the surface of the electrode is high, resulting in a low diffusion coefficient) until a certain stage where it tend to be activated or cleaned as seen by an increase in capacity from 4 µA to 8 µA. A high discharge capacity at lower discharge current of 2 µA is the results consistent with the findings by Nutzenadel *et al.* [1]. The discharge capacity of the GCE-MWCNT-Ni_{cal} electrode increases slightly and saturate to a maximum value with increasing discharge current density. The slight increase of the discharge capacity of the GCE-MWCNT-Ni_{cal} electrode at higher discharge current may be attributed by the existence of various forms of pores and pore diameters in the electrode. It seems that some pores with small diameters can be invaded by ions from the electrolyte with high discharge current.

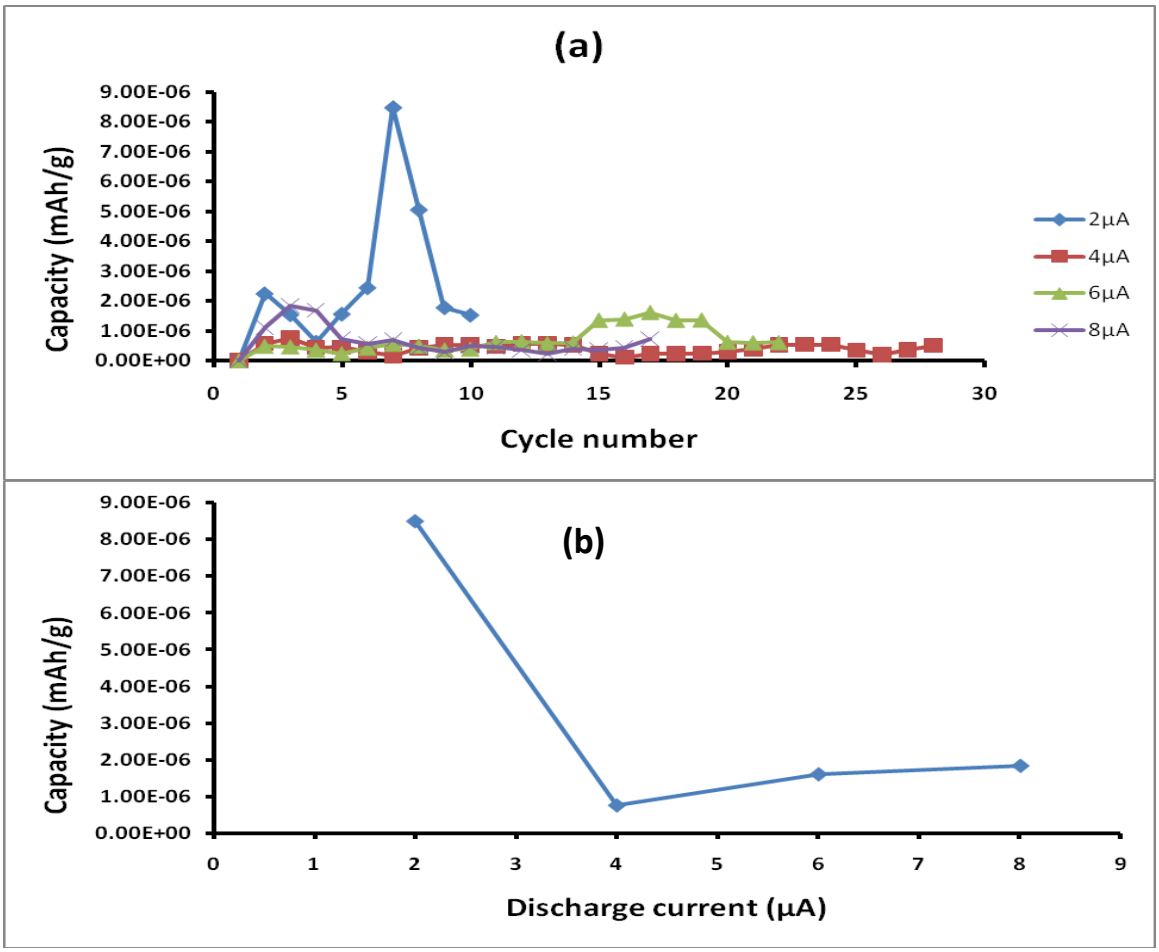

Figure 4.57: (a) plots comparing the discharge capacity of GCE-MWCNT-Ni_{cal} as a function of cycle number from different applied discharge current and **(b)** the plot showing the variation of the discharge capacity of GCE-MWCNT-Ni_{cal} electrode with respect to the applied discharge current.

4.3.5.13.4.2 GCE-MWCNT-Ni_{uncal} (4wt% Ni) electrode

The behavior of the discharge capacities as a function of cycle number for the GCE-MWCNT-Ni_{uncal} electrode from different applied discharge current is depicted in figure 4.58 **(a)**. The GCE-MWCNT-Ni_{uncal} nanocomposite electrode was chosen because it gave the highest current respond as compared to GCE-MWCNT-Ni_{cal}. It can be seen that as the applied discharge current is increased,

the discharge capacity also increases. It is also confirmed here that the higher the discharge capacity, the short the life cycle of the GCE-MWCNT-Ni_{uncal} electrode. When 2 µA is applied the electrode lives up to 21 cycles and when 8 µA of discharge current is applied, the electrode live up to cycle number 9.

Figure 4.58 **(b)** clearly shows the relationship between the applied discharge current and the maximum discharge capacity of the GCE-MWCNT-Ni_{uncal} electrode. It can be seen that as more discharge current is applied, the discharge capacity also increases. No significant increase in capacity is seen for an applied discharge current of 8 µA. These findings are consistent with the results obtained in charge-discharge experiment and with the results reported by Dong *et al*. [59].

But they are in contrast with that of the metal hydride electrodes where the capacity decreases steeply at higher discharging currents. These present study reveals that CNTs may indeed be useful in battery technology for the replacement of metal hydride electrodes. It is expected that at high discharge current, the discharge capacity should drop as the will be hindrance of ions at the surface of the electrode i.e. more ions are unable to diffuse to the inside of the electrode resulting in low discharge capacity at high applied discharge current. This seems not to be the case for the GCE-MWCNT-Ni electrode, probably due to their increased surface area and pore structure by introduced nickel nanoparticles [59].

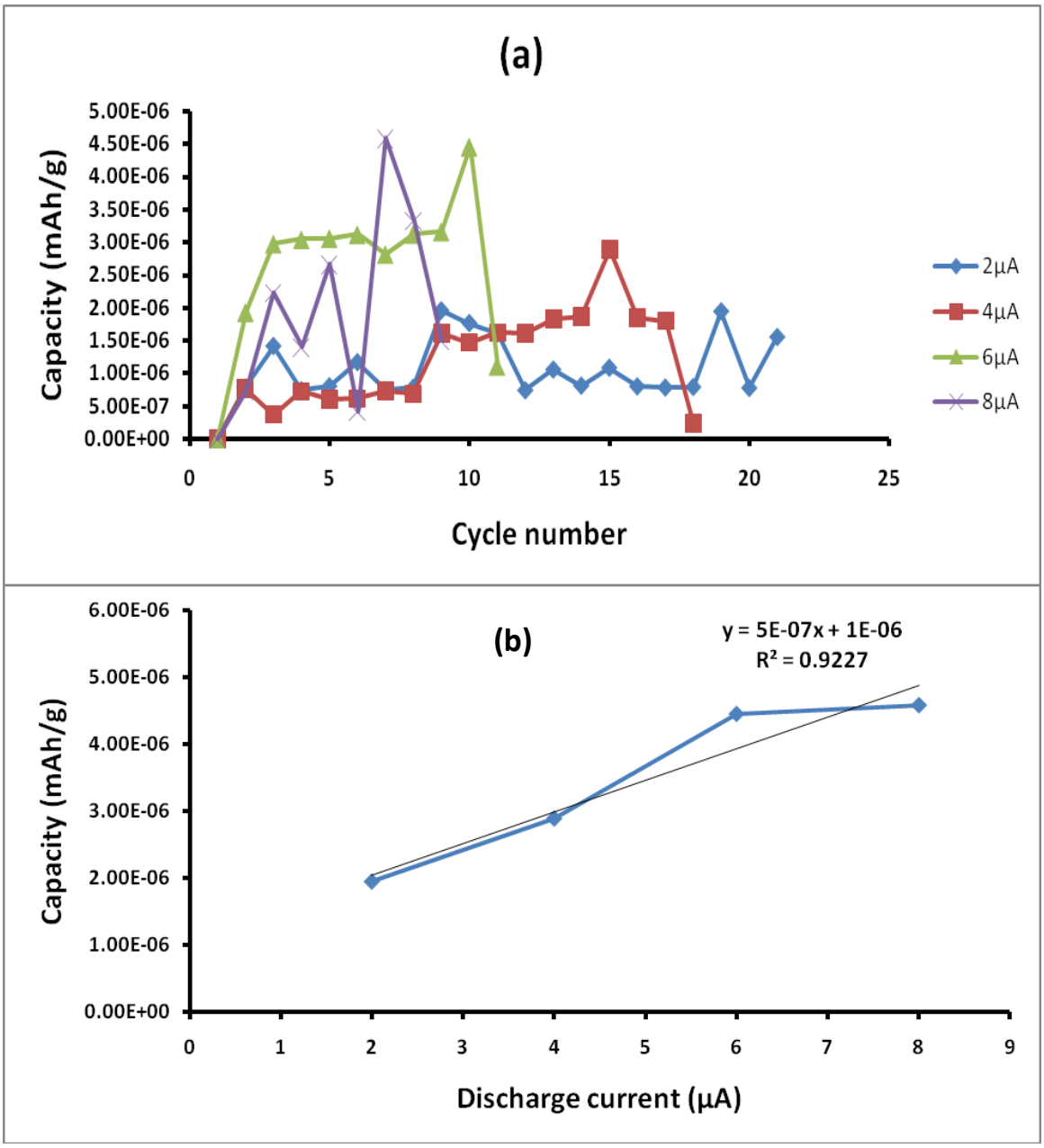

Figure 4.58: (a) The plots of discharge capacity against cycle number from different applied discharge current and **(b)** Variation of the electrochemical discharge capacity of GCE-MWCNT-Ni_{uncal} electrode with respect to the discharge current.

4.3.5.13.5 Comparison of the applied discharge current on the discharge capacity using GCE-MWCNT-Ni_{cal} (4wt% Ni) and GCE-MWCNT-Ni_{uncal} (4wt% Ni) electrodes

Figure 4.59 compares the discharge capacity of the GCE-MWCNT-Ni_{cal} and GCE-MWCNT-Ni_{uncal} electrodes as a function of applied discharge current. The GCE-CNT-Ni_{cal} tends to lose capacity from an applied current of 2 µA to 4 µA. After which its stability is maintained as seen by an increase in discharge capacity with applied current. The discharge capacity of the GCE-MWCNT-Ni_{uncal} electrode increase at a higher rate than of GCE-MWCNT-Ni_{cal} electrode. The deterioration of discharge capacity of GCE-MWCNT-Ni_{cal} electrode is caused by the large internal resistance of the electrode compared to the GCE-MWCNT-Ni_{uncal} electrode. The large internal resistance causes a large ohmic (IR) drop at high discharge current, resulting in the decrease of the discharge capacity. The magnitude of the equivalent series resistance (ESR) can clearly be shown by the use of electrochemical impedance spectroscopy (EIS) [84].

The Q test was used to validate the outlier at an applied discharge current of 2 µA by the GCE-MWCNTs-Ni_{cal} electrode. The Q experimental for an outlier in figure 4.94 was calculated as follows:

a = 7.62E-7 mAh/g - 8.49E-6 mAh/g = - 7.728E-6 mAh/g,
w = 1.84E-6 mAh/g - 8.49E-6 mAh/g = - 6.650E-6 mAh/g.

Therefore, Q_{exp} = a/w = - 7.728E-6 mAh/g / - 6.65E-6 mAh/g = 1.161

Therefore, for 4 measurements at 95% confidence level, Q_{crit} = 0.829, implying that Q_{exp} (1.161) > Q_{crit} (0.829). Therefore, we reject the outlier so that it does not influence the conclusions of the findings.

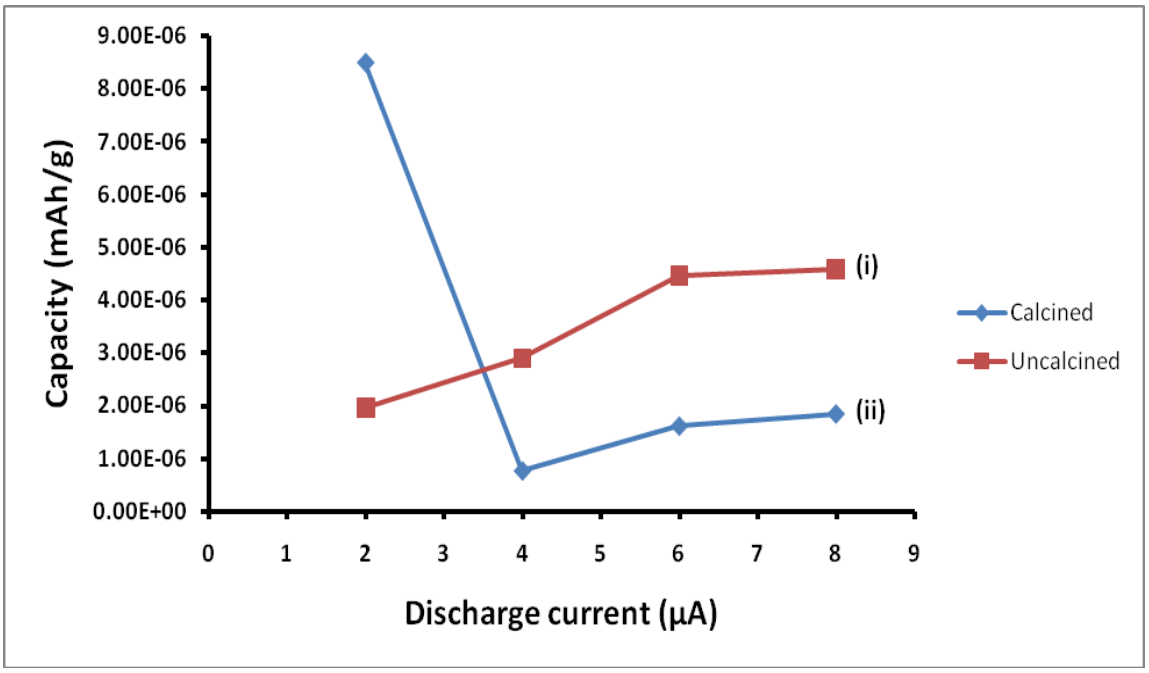

Figure 4.59: The plots comparing the discharge capacities of (i) GCE-MWCNT-Ni_{uncal} and (ii) GCE-MWCNT-Ni_{cal} as a function of applied discharge current.

Therefore, it can be concluded that the uncalcined nickel nanoparticles increase both the electro-catalytic activity and capacity of GCE-MWCNTs for hydrogen storage than the calcined nickel nanoparticles.

4.3.5.13.6 Effect of CPE run number on the discharge capacity of the GCE-MWCNT-Ni_{cal} (4wt% Ni) electrode

The following CPE profiles investigate the effect of run number on the discharge capacity of GCE-MWCNT-Ni_{cal} for hydrogen storage. The profiles were taken from three runs from the applied potential of -692 mV. This potential was obtained by applying 2 µA of current in CP. This investigation will also try to prove the stability of the capacity of discharge current of 2 µA seen above.

The maximum capacities of different runs for the CPE of GCE-MWCNT-Ni_{cal} as a function of cycle number are shown in figure 4.60 **(a)**. The applied potential for the runs was kept constant at -0.692 V which was obtained from an applied discharge current of 2 µA in chronopotentiometry. The third run showed a maximum capacity followed by the second and then the first run. In this case, the third run which showed a maximum capacity had a longer cycle life than the second run. The longest cycle life was seen for the first cycle. Figure 4.60 **(b)** shows the relationship between the discharge capacity and the run number for the GCE-MWCNT-Ni_{cal} electrode. It can be seen that as the run number increases, there is also an increase in discharge capacity of GCE-MWCNT-Ni_{cal} for hydrogen storage. This shows that by multi-running, the surface of the electrode tend to be activated.

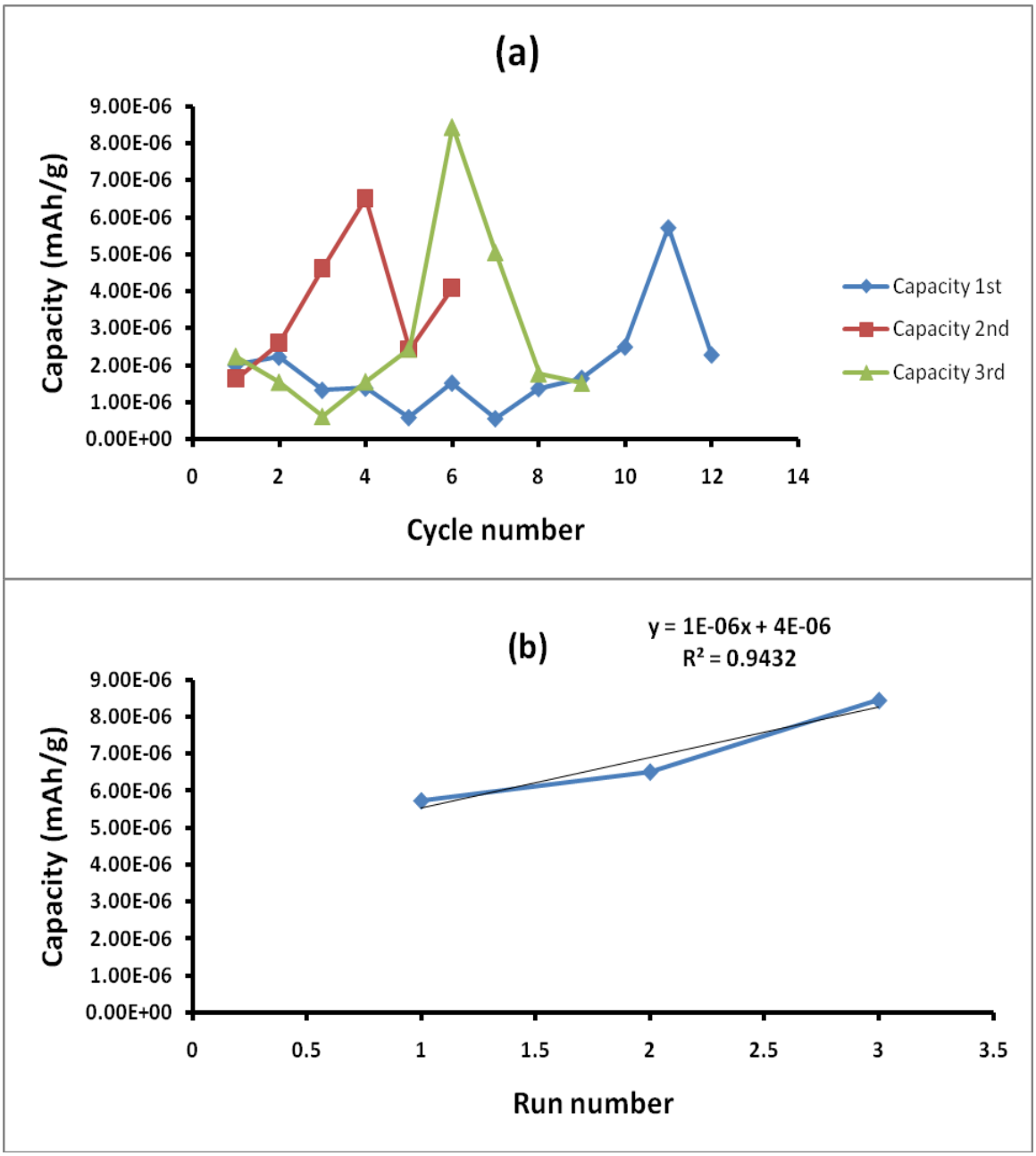

Figure 4.60: (a) The plot of discharge capacity against cycle number for different run numbers and **(b)** the relationship between discharge capacity and run number.

4.3.5.14 Effect of the amount of MWCNT-Ni_{uncal} (4wt% Ni) modified GCE

The hydrogen storage capacity depends not only on the surface area, porosity and electrical conductivity of the material, but also on the surface chemistry, which is a critical factor [105-108]. Therefore, it is of interest to investigate the effect of the quantity of MWCNT-Ni_{uncal} nanocomposite on the electrochemical activity of the GCE-MWCNT-Ni_{uncal} working electrode for hydrogen storage. The following study investigates the dependence of the current response, charge-discharge voltages and discharge capacity on the amount of MWCNT-Ni_{uncal} modifier concentrations. The amount MWCNT-Ni_{uncal} in DMF was ranged from 20 to 60 µl. The temperature of the 6 M KOH aqueous solution electrolyte was 25 ^{o}C.

4.3.5.14.1 Cyclic voltammetric response for various amount of MWCNT-Ni_{uncal} electrode

Cyclic voltammetric profiles for the different quantities of MWCNT-Ni_{uncal} nanocomposite are compared in figure 4.61. The sweep rate used was 0.01 V/s. There is an increase in current density from a MWCNT-Ni_{uncal} content of 20 µl to 40 µl. When more MWCNT-Ni_{uncal} is added to the surface of the GCE bare electrode, there is a decrease in current density due to the distance between the MWCNT-Ni_{uncal} materials and active surface area of the glassy carbon increasing. i.e., electrons take time to reach the active area to be transferred. This behavior is consistent with the results reported by Swamy *et al*. [83] who investigated the dependence of the electrochemical response on the amount of BMPTB modifier at a range of 1.25 to 10 µl. They found that a peak current increased linearly to 5 µl after which it dropped. The enhanced current values can be attributed to the high local density of the electronic states in the MWCNT-Ni_{uncal} nanocomposite. On the other hand, the decrease in the current density is

in accordance with a large surface area of the MWCNT-Ni_{uncal} that increases the background current [83]. Moreover, changes in the composite structure and hence charge transfer properties could lower the current values. Therefore, it can be said that the current signal increase gradually with the amount of MWCNT-Ni_{uncal} up to a certain defined level (from 20 µl to 40 µl) and then a decrease is observed at higher levels (60 µl). Evidence of the decrease in current response above 40 µl is an indication that the conductivity of the electrode is influenced by the degree at which the electrode was modified. The increase in the number of donor groups or active moieties decreased considerably the amount of carbon, which was responsible for the conductivity of the electrode. At 40 µl modifier concentration, the amount of modifier is probably sufficient to attain maximum conductivity [117].

Figure 4.61 compares the current densities for various MWCNT-Ni_{uncal} nanocomposite contents at a high scan rate of 100 mV/s. The same behavior was observed with an increase in current density from 20 µl to 40 µl MWCNT-Ni_{uncal}. As more MWCNT-Ni_{uncal} are added to the surface of the electrode, there is a sharp drop in current density as seen in figure 4.61 **(iii)** for 60 µl MWCNT-Ni_{uncal} nanocomposite electrode. During the experimental analysis, it was observed that as more MWCNT-Ni_{uncal} are added on the surface of the GC bare electrode, some of the MWCNT-Ni_{uncal} nanocomposite tend to fall into the electrolyte solution due to less interaction between the active surface area of the glassy carbon electrode and the MWCNT-Ni_{uncal} materials.

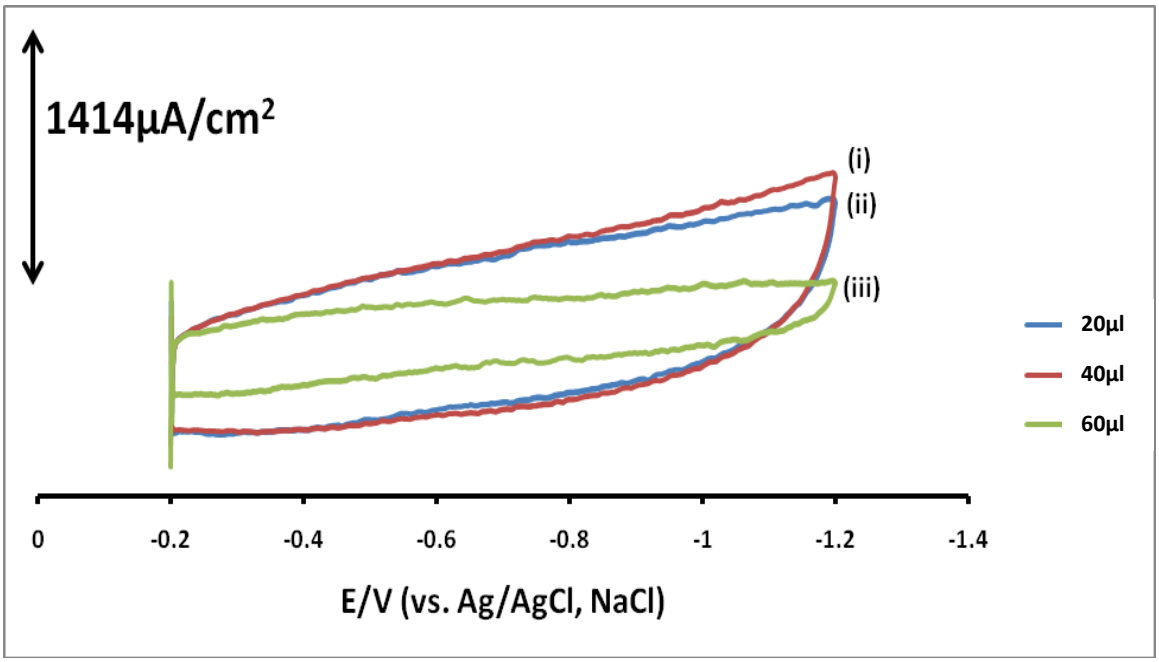

Figure 4.61: Cyclic voltammetric profiles of GCE-MWCNT-Ni_{uncal} electrode at a MWCNT-Niuncal quantity of **(i)** 40 µl, **(ii)** 20 µl and **(iii)** 60 µl. Scan rate = 100 mV/s.

4.3.5.14.2 Charge-discharge voltage studies

An interesting behavior is depicted in figure 4.62 for the voltage profiles of the GCE-MWCNT-Ni_{uncal} electrode at various MWCNT-Ni_{uncal} quantities. The applied charge current was -2 µA. It can be observed that as the MWCNTs-Ni_{uncal} content is increased, the charge voltage also tend to increase. MWCNT-Ni_{uncal} content of 60 µl tend to be charged to a high voltage compared to lower content of 20 µl which shows a low charge voltage. The charge curve for 60 µl MWCNT-Ni_{uncal} nanocomposite has an approximate voltage plateau of 0.250 V.

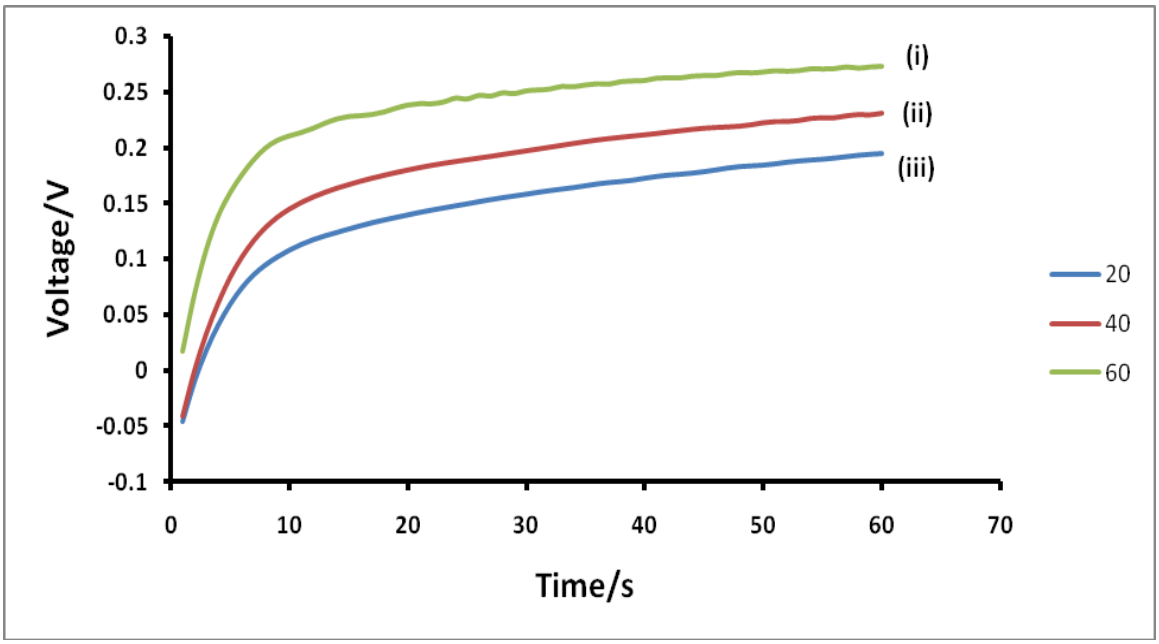

Figure 4.62: Voltage profile showing the charge voltage for GCE-MWCNT-Ni_{uncal} electrode at a MWCNT-Ni_{uncal} content of **(i)** 60 µl, **(ii)** 40 µl and **(iii)** 20 µl from an applied charge current of -2 µA.

And also as the MWCNT-Ni_{uncal} content increases, the discharge voltage of the GCE-MWCNT-Ni_{uncal} electrode increases as shown in figure 4.63. The discharge current applied for this chronopotentiometric analysis was 2 µA. The increase in discharge voltage is in the order; 20 µl < 40 µl < 60 µl amount of MWCNT-Ni_{uncal} coated on the active area of the glassy carbon bare electrode.

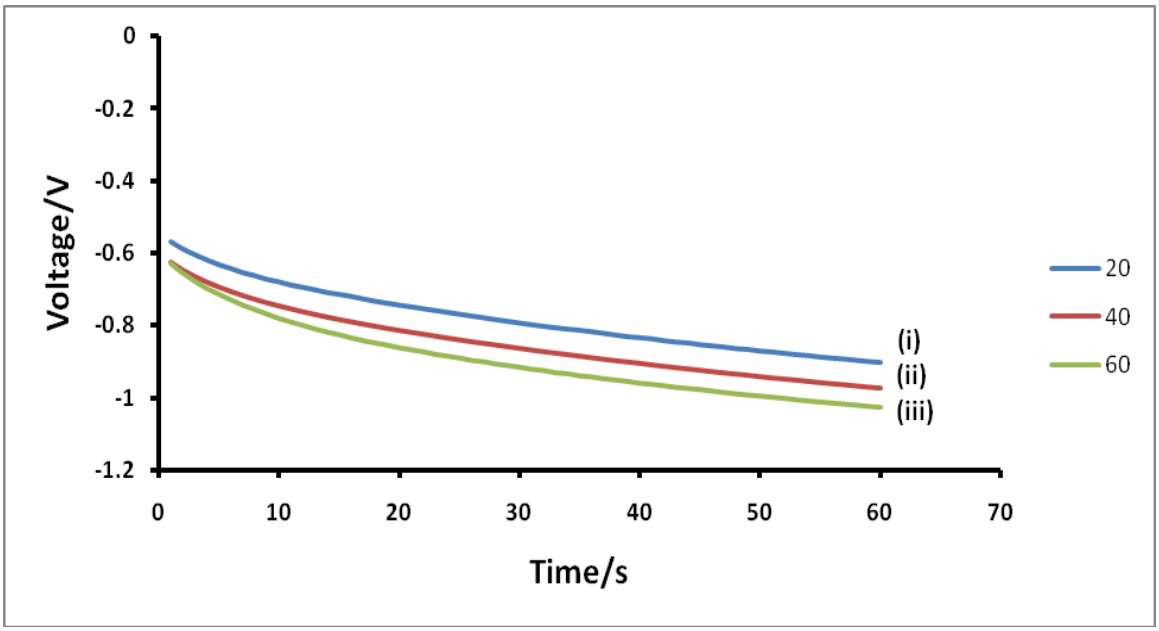

Figure 4.63: Voltage profile depicting the discharge voltage of GCE-MWCNT-Ni_{uncal} electrode at a MWCNT-Ni_{uncal} nanocomposite content of **(i)** 20 µl, **(ii)** 40 µl and **(iii)** 60 µl from an applied discharge current of 2 µA for 60 seconds.

4.3.5.14.3 Controlled potential electrolysis investigations for the various quantities of the MWCNT-Ni_{uncal} nanocomposites

Comparative discharge capacities of the GCE-MWCNT-Ni_{uncal} electrode at various quantities of the MWCNT-Ni_{uncal} are depicted in figure 4.64. It can be observed that the maximum capacity of the 40 µl MWCNT-Ni_{uncal} is obtained at a short cycle number of 1 compared to cycle number 3 of the 20 µl MWCNT-Ni_{uncal} and 5 for 60 µl MWCNT-Ni_{uncal} nanocomposite. It can also be seen that both 20 µl and 40 µl MWCNT-Ni_{uncal} nanocomposite electrode have equal life cycle of living up to eighth cycle. MWCNT-Ni_{uncal} with a content of 60 µl shows a long cycle life of 15.

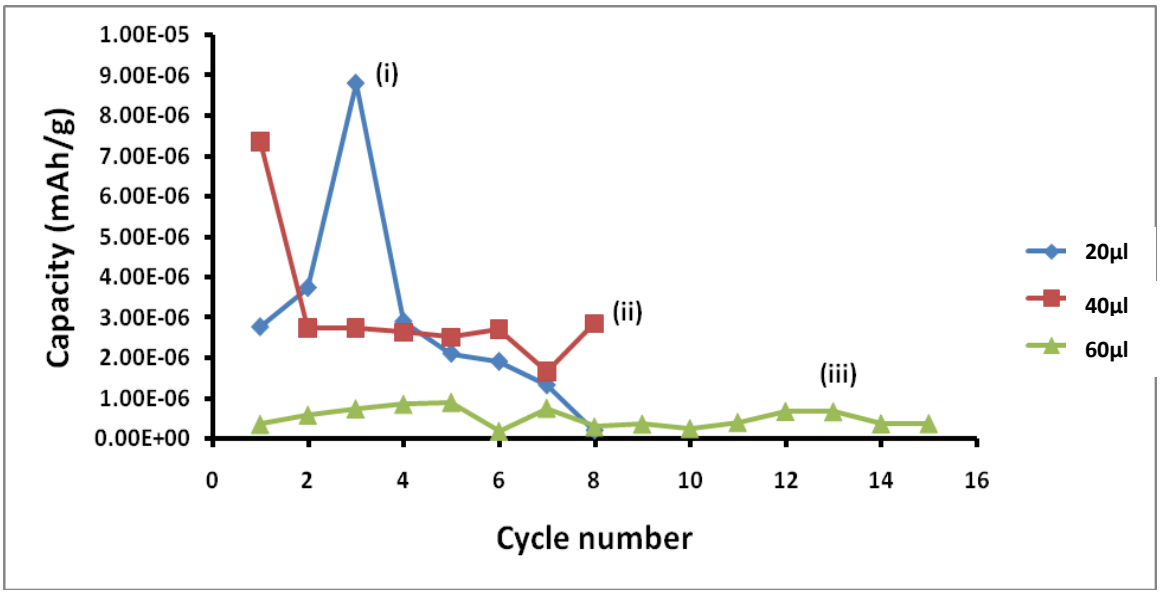

Figure 4.64: The combined plots of discharge capacity as a function of cycle number for the GCE-MWCNT-Niuncal electrode at MWCNT-Ni_{uncal} contents of **(i)** 20 µl, **(ii)** 40 µl and **(iii)** 60 µl.

Figure 4.65 shows the relationship between the discharge capacity and the quantity of the MWCNT-Ni_{uncal} nanocomposite. The results show that as the quantity of the MWCNT-Ni_{uncal} nanocomposite increases on the surface of the GCE, the hydrogen uptake tend to decrease. This shows that the active surface area (ASA) of the GCE-MWCNT-Ni_{uncal} tend to be clogged as more materials are added. It is also known that as the amount of surface oxygen increase, the hydrogen uptake by nanocomposite tends to be lowered. A gradual decrease is seen from 20 µl to 40 µl MWCNT-Ni_{uncal}, and thereafter a sharp decrease from 40 µl to 60 µl MWCNT-Ni_{uncal} tends to occurs.

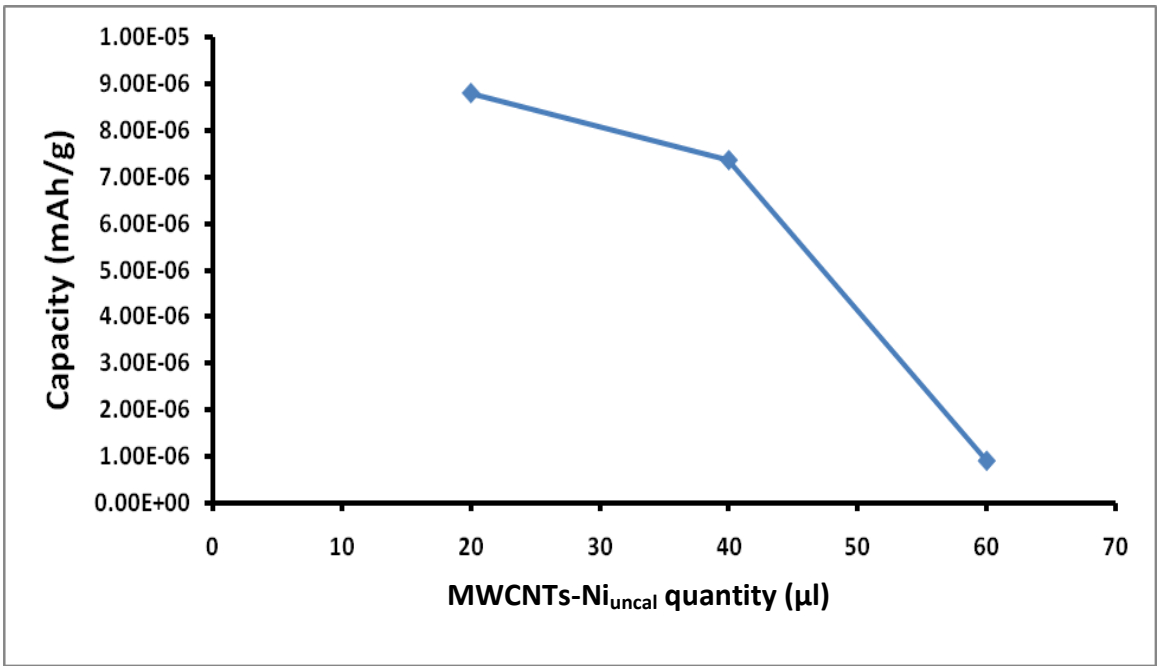

Figure 4.65: The plot clearly showing the relationship between the discharge capacity and the MWCNT-Niuncal quantity using the GCE-MWCNT-Niuncal working electrode.

Therefore, it can be said that the GCE-MWCNT-Ni_{uncal} electrode with a MWCNT-Ni_{uncal} quantity of 40 µl shows both high current response (as seen in CV studies above) and electrode stability compared to 20 µl which only shows high discharge capacity. Electrode with 60 µl MWCNT-Ni_{uncal} shows a high charge-discharge voltage and long cycle life compared to 20 µl and 40 µl MWCNT-Ni_{uncal} nanocomposite.

4.4 References

[1] C. Nutzenadel and A. Zuttel et al., Electrochemical and Solid-State Letters, 2 (1999) 30-32.

[2] D. Zhang and H. Yuan et al., Journal of Functional Materials and Devices, 9 (1998) 167-174.

[3] C.N.R. Rao and G. Gautam, Journal of Material Chemistry, 13 (2003) 209-213.

[4] J.C. Vickerman, Surface Analysis: The Principal Techniques, 1st edn, John Wiley and Sons, chichester, 67 (1997) 768-769.

[5] X. Wang, W. Hu, Y Liu and S. Zhou, Carbon, 39 (2001) 1533-1539.

[6] B.C. Liu, T.J. Lee, S.I. Jung and C.Y. Park, Carbon, 43 (2005) 1341-1346.

[7] C.T. Hsieh, Y.W. Chou and J.Y. Lin, International Journal of Hydrogen Energy, 32 (2007) 3457-3464.

[8] K.M.A. Hague, M.S. Hussain, S.S. Alam and M.S. Islam, African Journal of Pure and Applied Chemistry, 4 (2010) 58-63.

[9] P. Mahanandia and K.K. Nanda, Nanotechnology, 19 (2008) 155-156.

[10] J. Khathi, K.L. Rhee and J.H. Lee, Composites, part A, 40 (2009) 800-809.

[11] T. Ramanathan, F.T. Fisher, R.S. Ruoff and L.C. Brinson, Chemistry Master, 17 (2005) 1290-1295.

[12] N.N. Vesali, A.A. Khadadadi and S.S. Mosadegh, Engineering and Technology, 49 (2009) 177-179.

[13] J. Liu, Z. Mao, D. Hao, X. Xie and D. Wu, The Electrochemical Society, 130 (2003) 1441-1443.

[14] C. Xu, G. Wu, Z. Liu, D. Wu, T.T. Meek and Q. Han, Material Research Bulletin, 39 (2004) 1499-1505.

[15] J.F. Chen, C.L. Xu, Z.Q. Man, G.R. Chen, B.Q. Wie, J. Liang and D.H. Wu, Chinese Series A, 45 (2002) 82-86.

[16] D. Li and Y. Xia, Nanotechnology Letters, 4 (5) (2004) 933-938.

[17] Y.F. Yin, T. Mays and B. McEnaney, Adsorption of Nitrogen in Carbon Nanotubes Array, Langmuir, 15 (1999) 8714-8718.

[18] Y.H. Li, J. Ding, Z. Luan and C. Xu, Carbon, 41 (2003) 2787-2792.

[19] C.T. Hsieh, J.M. Chen, R.R. Kuo and Y.H. Huang, Applied Physics Letters, 84 (2004) 1186-1188.

[20] Y.C. Xing, Journal of Physical Chemistry B, 108 (2004) 19255-19259.

[21] A.K.M Fazle Kibria, Y.H. Mo, K.S. Park, K.S. Nahm and M.H. Yun, International Journal of Hydrogen Energy, 26 (2001) 823-829.

[22] H.S. Kim, H. Lee, K.S. Han, J.H. Kim, M.S. Song and M.S. Park, Journal of Physical Chemistry B, 109 (2005) 8983-8986.

[23] S. Chen, W. She, G. Wu, D. Chen and M. Jiang, Chemical Physics Letters, 402 (2005) 312-317.

[24] P. Serp, M. Corrias and P. Kalck, Applied catalysis A: General, 253 (2003) 337-358.

[25] M. Fleischer and H. Meixner, Sensors and Actuators B, 52 (1998) 179-187.

[26] J. Liu, A.G. Rinzler and J.H. Hafner, Fullerene pipes. Science, 280 (1998) 1253-1255.

[27] C. Bower and O. Zhou, Chemical Physics Letters, 288 (1998) 481-486.

[28] A.C. Dillon, T. Gennett and K.M. Jones, Advanced Matter, 11 (1999) 1354-1358.

[29] L. Vaccarini, L. Goze, V. Journet and C. Bernier, Synthesis Methods, 103 (1999) 2492-2493.

[30] K. Hyeok, K. Ku, S. Chu and D. Jae, Journal of the Electrochemical Society, 149 (2002) 1058-1062.

[31] W. Xianbao, H. Wenping and L. Yungi, Carbon, 39 (2001) 1533-1536.

[32] S.R. Chung, W.K. Wang and P.T Peng, Material Science, 39 (2001) 1681-1682.

[33] O.P. Gorelik, P. Nikolaev, S. Arepalli and B.W. Smith, Purification Procedure for Carbon Nanotubes. NASA/CR, 26 (2001) 2000-2089.

[34] P.C. Ho and D.A. Palmer, Solution Chemistry, 25 (1996) 711-712.

[35] P.C. Ho and D.A. Palmer, Chemical Engineering Data, 42 (1998) 1162-1164.

[36] G.H. Zimmerman, M.S. Gruszkiewiez and R.H. Wood, Journal of Physical Chemistry, 99 (2000) 217-218.

[37] M.L. Machesky, D.J. Wesolowski, D.A. Palmer and H.J. Ichiro-Hayashi, Journal of Colloids Interface Science, 200 (1998) 298-299.

[38] J.C. Justice and B.E. Bockris, Comprehensive Treatise Electrochemistry: Conway. Plenum Press: New York, 47 (1973) 525-526.

[39] A.J. Ellis, Journal of Chemistry Society A, 90 (1966) 1579-1581.

[40] R. Fernandez-Prini, Physical Chemical of Organic Solvent Systems: Plenium Press: New York, 210 (1973) 525-526.

[41] D.G. Archer and P. Wang, Journal of Physical Chemistry Data, 19 (1990) 371-372.

[42] M.S. Dresselhaus and G. Dresselhaus, Advances in Physics, 30 (1981) 139-326.

[43] G. Jinghong, P. Chengjiu and M. Yongzhi, Chinese Journal of Power Sources, 24 (2000) 189-190.

[44] X. Zhang, Y. Chen and T.A Mingda, Journal of Rare Earth, 26 (2008) 402-403.

[45] Y. Xianxia and X. Naixin, Acta Chimica Sinica, 60 (2002) 13-14.

[46] G. Zhang, B.N Popov and R.E White, Journal of Electrochemistry Society, 142 (1995) 2695-2696.

[47] W.X. Chen, J.Q. Qi, Y. Chen, C.P. Chen, Q.D. Wang and J.M Zhou, Journal of Alloys Compounds, 728 (1999) 293-294.

[48] J. Barnaby, Regulators Stamp Copper. New York Times, 301 (2008) 2345-2346.

[49] W. Rayner, Copper metal. Greenwood Publishing group, 32 (2007) 56-57.

[50] N.N. Greenwood and A. Earshaw, Chemistry of the Elements.2nd Edition, Butterworth-Heinemann, Oxford, UK, 56 (1997) 456-457.

[51] The Merck Index, 7th Edition, Merck and Co, Rahway, Ney Jersey, USA, 78 (1990) 890-892

[52] D. Nicholis, Complexes and First-Row Transition Elements. Macmillan Press, London, 56 (1973) 432-433.

[53] H. Feng, C. Shao and Z. Dong, International Journal of Hydrogen Energy, 32 (2007) 1294-1298.

[54] J. Pillay, K. Ozoemena and T. Nyokong, Electrochemistry Communications, 8 (2006) 1391-1392.

[55] P.P. Pier, P. Alfonso, B. Sabina and C. Roberto, Journal of Power Sources, 118 (2003) 265-269.

[56] W.J. Zhang, Nanoparticles Res, 5 (2003) 323-326.

[57] S.G. Reinaldo and M.S. Alzira, Journal of Brazilian Chemical Society, 11 (2000) 486-490.

[58] X. Zhang, J. Wang, Z. Wang and S. Wang, Sensors, 5 (2005) 580-593.

[59] M.L. Seung, S.P. Ki, C.C. Young and J.B. Dong, Synthetic Metals, 113 (2000) 209-216.

[60] E.A. Karakhanov, S.V. Kardashev, L.L. Meshkov and S.N. Nesterenko, Vestn. Mosk. University Series 2: Khim, 39 (1998) 214-215.

[61] J. Bandara, J. Kiwi, C. Pulgarin and G. Pajonk, Journal of Catalysis Chemistry A, 111 (1996) 333-334.

[62] Y. Ichihashi and Y. Matsumura, Journal of Catalysis, 202 (2001) 427-428.

[63] H. Kohl, Handbook of Materials and Techniques for Vacuum Devices. Springer, 67 (1995) 164-167.

[64] V. Ragharan, Materials Science and Engineering. PHI Learning Pvt Ltd, 54 (2004) 218-219.

[65] J.W. Martin, Concise Encyclopedia of the Structure of Materials. Elsevier, 43 (2007) 183-184.

[66] R.M. Cornell, The Iron Oxides: Structure, Properties and Reactions. Wiley, 3 (2005) 527-528.

[67] T.L. Johnson, W. Fish, Y.A. Gorby and P.G, Tratnyek. Contam. Hydrology, 29 (1998) 377-396.

[68] M. Carnes et al., Angewandte Chemie International Edition, 48 (2009) 3384-3385.

[69] S. Pfirrmann et al., Angewandte Chemie International Edition, 48 (2009) 3357-3358.

[70] R. Eric, Oxford university press, 56 (2007) 239-240.

[71] A. Earnshaw and N. Norman, Chemistry of the Elements. Oxford: Pergamon, 23 (2005) 1336-1337.

[72] K. Lascelles, L.G. Morgan and D. Nicholls, Encyclopedia of Industrial Chemistry. Wiley, Weinheim, 67 (2005) 2123-2124.

[73] G. Schmid, Chemical Review, 92 (1992) 1709-1711.

[74] P.V. Kamat, Chemical Review, 93 (1993) 267-268.

[75] K.J. Kjabunde, J. Stark, O. Koper, C. Mohs, G.P. Dong, S. Decker, Y. Jiang, I. Lagadic and D. Zhang, Journal of Physical Chemistry, 100 (1996) 12142-12143.

[76] K.M. Dooley, S.Y. Chem and J.R.H. Ross, Journal of Catalysis, 145 (1994) 402-403.

[77] A. Alejandre, F. Medina, P. Salagre, A. Fabregat and J.E. Sueiras, Applied Catalysis B, 18 (1998) 307-308.

[78] L. Soriano, M. Abbate, J. Vogel and J.C. Fuggle, Chemical Physics Letters, 208 (1993) 460-461.

[79] V. Biji and M.A. Khadar, Material Science Engineering A, 814 (2001) 304-306.

[80] R.H. Kodama, S.A. Makhlouf and A.E. Berkowitz, Physical Review Letters, 79 (1997) 1393-1394.

[81] R.H. Kodama, Journal of Magnetic Materials, 200 (1999) 359-360.

[82] F. Li, H. Chem, C. Wang and K. Hu, Journal of Electroanalytical Chemistry, 531 (2002) 53-54.

[83] B.E. Swamy Kumara, G. Ongera and H.G. Sathish, International Journal of Electrochemical Science, 5 (2010) 1187-1202.

[84] H. Chien-Te, C. Yu-We and L. Jia-Yi, International Journal of Hydrogen Energy, 32 (2007) 3457-3464.

[85] Y. Nuli, S. Zhao and Q. Qin, Journal of Power Sources, 114 (2003) 113-114.

[86] R. Palombari, Journal of Electroanalytical Chemistry, 546 (2003) 23-24.

[87] M. Matsumiya, F. Qui, W. Shin, N. Izu, N. Murayama and S. Kanzaki, Thin Solid Films, 419 (2002) 213-214.

[88] C. Niu, E.K. Sichel, R. Hoch, D. Moy and H. Tennet, Applied Physics Letters, 1480 (1997) 70-72.

[89] C. Liu, A.J. Bard, F. Wudl, I. Weitz and J.R. Heath, Electrochemical Solid-State Letters, 2 (1999) 577-578.

[90] P.J. Britto, K.S.V. Santhanam and P.M. Ajayan, Bioelectrochemical Bioenergies, 41 (1996) 61-63.

[91] E. Frackowiak, S. Gatier, H. Gaucher, H. Bonnay and F. Beguin, Carbon, 37 (1996) 61-62.

[92] A.C. Dillon, K.M. Jones, T.A. Bekkedahl, C.H. Kiang, D.S. Bethun and M.J. Heben, Nature, 386 (1997) 377-378.

[93] A. Chambers, C. Pak, R.T.K. Baker and N.M. Rodriguez, Journal of Physical Chemistry B, 102 (1998) 4253-4254.

[94] Y. Ye, C.C. Ahn, C. Witham, B. Fultz, J. Liu, A.G. Rinzler, D. Colbert, K.A. Smith and R.E. Smalley, Applied Physics. Letters, 74 (1997) 2307-2308.

[95] C. Liu, Y.Y. Fang, M. Liu, H.T. Cong, H.M. Cheng and M.S. Dresselhaus, Science, 1127 (1999) 286-287.

[96] N. Rajalakshmi, K.S. Dhathathreyan, A. Govindaraj and B.C. Satishkumar, Electrochimica Acta, 45 (2000) 4511-4512.

[97] X. Qin, X.P. Gao, H. Liu, H.T. Yuan, D.Y. Yan, W.L. Gong and D.Y. Song, Electrochemical Solid-State Letters, 3 (2000) 352-353.

[98] P.L. Taberna, C. Portet and P. Simon, Applied Physics, 82 (2006) 639-646.

[99] A.K.M. Fazle Kibria, Y.H. Mo, K.S. Park, K.S. Nahm and M.H. Yun, International Journal of Hydrogen Energy, 26 (2001) 823-824.

[100] Y.C. Xing, Journal of Physical Chemistry B, 108 (2004) 19255-19256.

[101] A.K.M. Fazle Kibria, Y.H. Mo, K.S. Park, K.S. Nahm and M.H. Yun, International Journal of Hydrogen Energy, 26 (2001) 823-829.

[102] X.P. Gao, Y. Lan, G.L. Pan, F. Wu, J.Q. Qu and D.Y. Song et al., Electrochemical Solid-State Letters, 4 (2001) 173-175.

[103] X. Qin, X.P. Gao, H. Liu, H.T. Yuan, D.Y. Yan and W.L. Gong et al., Electrochemical Solid-State Letters., 3 (2000) 532-535.

[104] H.S. Kim, H. Lee, K.S. Han, J.H. Kim, M.S. Song and M.S. Park et al., Journal of Physical Chemistry B, 109 (2005) 8983-8986.

[105] R.N. Bargava and J. Lumin, Journal of Physical Chemistry, 70 (1996) 85-86.

[106] E.T. Goldvurt, B. Kulkarni and R.N. Bhargava et al., J. Lumin. Journal of Physical Chemistry, 72 (1997) 190-191.

[107] E.F. Hilinske, P.A. Lucas and Y. Wang, Journal of Chemical Physics, 89 (1998) 3435-3436.

[108] M. Yoshio, Y. Todorov and K. Yamato et al., Journal of Power Sources, 74 (1998) 46-47.

[109] H.X. Yang, Q.F. Dong and X.H. Hu, Journal of Power Sources, 79 (1999) 256-257.

[110] I. Hotovy, J. Huran and L. Spiess et al., Vacuum, 58 (2000) 300-301.

[111] E.L. Miller and R.E. Rocheleau, Journal of Electrochemistry Society, 144 (1997) 3072-3073.

[112] Y. Ichiyanagi, N. Wakabayashi and J. Yamazaki et al., Physica B, 862 (2003) 329-333.

[113] S.A. Makhlouf, F.T. Parker, F.E. Spada and A.E. Berkowitz, Journal of Applied Physics, 81 (1997) 5561-5562.

[114] X.Y. Deng and Z. Chen, Material Letters, 58 (2004) 276-277.

[115] K. Jung, K. Sunwook and H. Sung-Hong, Journal of Material Science, 37 (2002) 1455-1460.

[116] M.R. Gennero de Chialvo and A.C. Chialvo, Journal of Brazilian Chemical Society, 5 (1994) 137-143.

[117] E. Elmer-Rico and E. Florinia, Journal of Applied Sciences, 5 (2005) 1461-1465.

CHAPTER 5

General Conclusions

Multi-walled carbon nanotubes (MWCNTs) were successfully synthesized, and their micro-structural information was determined by the TEM which showed the presence of iron nanoparticles impurities. The as-prepared and acid treated MWCNTs were characterized by FTIR for the presence of organic functional groups. The OH^- group of the carboxylic acid was present on the FTIR spectrum of the purified MWCNTs. This confirmed a successful purification of the as-prepared MWCNTs. The XRD pattern of the as-prepared MWCNTs showed the presence of the Fe nanoparticles and amorphous carbon impurities.

MWCNTs were successfully decorated with metal nanoparticles and metal oxides as shown by TEM and SEM images. This suggested that the method employed to decorate MWCNTs with metal nanoparticles and metal oxides was effective. TEM images also showed MWCNTs to have open tips at the end allowing for maximum hydrogen storage. The drop-drying method used for modifying the GCE have shown to be effective, as the current response and discharge capacity tend to increased significantly for the glassy carbon modified electrode. This also suggested a successful modification of the MWCNT-M (where M = Cu, Fe, Ni, CuO, Fe_2O_3 and NiO) nanocomposite on the surface of the GCE.

Multi-walled carbon nanotubes (MWCNTs) were successfully oxidized as confirmed by their high current respond compared to the as-prepared MWCNTs. High discharge capacity by the as-prepared MWCNTs shows that metal nanoparticles impurities plays an important role in hydrogen storage.

The use of KOH electrolyte gave a high discharge capacity as compared to NaOH electrolyte indicating its suitability for hydrogen storage studies.

Concentration studies confirmed that 6 M KOH electrolyte is the suitable concentration for hydrogen storage studies due to its high discharge capacity.

Glassy carbon bare electrode showed a high charge voltage than the modified GCE. Metal nanoparticles and oxide decorated MWCNTs enhance the discharge voltage of the GCE. The discharge voltage was found not to be related to the discharge capacity. An increase in applied discharge and charge current resulted in an increase in discharge and charge voltage respectively.

The increase in discharge capacity of the electrode for hydrogen is in the order: GCE-Fe < GCE-MWCNT-Fe_2O_3 < GCE < GCE-MWCNT-Fe < GCE-MWCNT-CuO < GCE-MWCNT < GCE-Cu < GCE-CuO < GCE-Ni < GCE-Fe_2O_3 < GCE-NiO < GCE-MWCNT-Cu < GCE-MWCNT-NiO < GCE-MWCNT-Ni. High discharge capacity by a Ni and NiO decorated MWCNTs is typical of Nickel cadmium and Nickel metal hydride used in secondary batteries.

The GCE-MWCNT-Ni (2wt% MWCNTs) electrode showed the highest discharge capacity as compared to the loadings of 4wt%, 6wt% and 8wt% MWCNTs. The results suggest the need of smaller amount of MWCNTs on the surface of the electrode. The maximum current density was obtained when using GCE-MWCNT-Ni (4wt% Ni) electrode and this current decreased as more Ni nanoparticles were added. The GCE-MWCNT-Ni (4wt% Ni) electrode gave consistent results since higher discharge capacity was obtained.

Calcination of nickel nanoparticles enhanced the hydrogen evolution reaction, but provided slow electron transfer kinetics at the surface of the electrode. The TEM showed Ni_{cal} well dispersed on the surface of the MWCNTs better than Ni_{uncal} nanoparticles. The high current response by MWCNT-Ni_{uncal} as compared to MWCNT-Ni_{cal} proves that uncalcined Ni nanoparticles are electrochemically active than the calcined Ni nanoparticles. A low current response of the calcined Ni nanoparticles modified on the GCE-MWCNT might be due to the agglomeration of Ni nanoparticles. These resulted in a reduced surface area for electron transfer process to occur effectively. An increase in applied discharge

current was found to results in an increase in discharge capacity for both GCE-MWCNT-Ni_{uncal} and GCE-MWCNT-Ni_{cal} electrodes.

The higher the exchange current density value obtained, suggests that the hydrogen evolution reaction occurs rapidly. These results suggest that in future, the GCE-MWCNT-Ni_{cal} nanocomposite electrode will replace the expensive noble metals used as catalyst in acid electrolysers. But high overvoltage for hydrogen oxidation makes GCE-MWCNT-Ni electrode inadequate for use as catalyst in fuel cell applications.

The amount of nanoparticles modified on the glassy carbon electrode was found to be directly proportional to the charge and discharge voltages, but inversely proportional to the discharge capacity for hydrogen storage. This is an indication that the amount of modifiers needs to be monitored and controlled for better consistent results.